Simulating nonlinear acoustic field propagation with application to fisheries research

by

Kristin Pedersen

Thesis for the degree of Master of Science

Faculty of Mathematics and Natural Sciences
University of Oslo

January 2009

Preface

This thesis marks the end of my years as a student at the University of Oslo. It was commenced in March 2008 and finished in January 2009.

The road to submitting a master's thesis is inevitably a long and winding one, and mine was no exception. This year has has been a test of both patience and stamina, and the obstacles have been plentiful. There are a handful of people I would like to acknowledge for making this period of time a little easier.

First and foremost, my thanks go to my supervisor, associate professor Andreas Austeng and co-supervisor professor Sverre Holm. They managed to provide a subject that combined all of my fields of study in an elegant fashion. Sverre gave some helpful hints in the initial and final state of this thesis, and made himself available via e-mail during his sabbatical. Andreas has been a valuable support during this period, and is thanked for supplying me with articles and new ideas, for reading all of my ridiculously long e-mails and for his ability to stay positive, which was appreciated most of all.

I would like to use this opportunity to thank Thoril for keeping me company on all of those long days on the tenth floor; for our discussions – fruitful or otherwise, and for listening to my ranting whenever I needed it.

I owe thanks to all of my friends for being patient with me these last years, and for involving me in extra-scholar activities from time to time.

My parents have always been supportive of my pursuing an education, and I am profoundly grateful for their support, without which this would have been a lot harder.

Last, but not least; My heartfelt thanks go to Per Henrik for his invaluable love and encouragement during these last months. Coming second to my thesis never seemed to bother him, and he kept impelling me even though he sometimes received more blame than appreciation. I persevered thanks to you, and will do my best to reciprocate.

Oslo, January 2009
Kristin Pedersen

Contents

Chapter 1

Introduction

1.1 Motivation

Acoustic methods are used for many purposes in fisheries and marine research today. They can detect small or large objects in water, such as schools of fish, mines, submarines and plankton. Echosounders may remotely discriminate between different species of fish, and may be used to study their behaviour without invading their habitat. Using echosounders for abundance estimation is very common, and most fishing vessels carry such equipment and uses it actively in their everyday occupation.

Sound travelling through water was traditionally thought to be a linear or close to linear process. As echosounders and their accompanying equipment have improved over the recent years, one has become aware of the fact that nonlinear effects may induce excess sound attenuation. These effects are induced by the water medium because of a varying sound speed, which distorts the waveform. As a result, the energy carried by the wave is lessened compared to that resulted by linear propagation. Echosounders used today do not correct for nonlinear effects, but disregarding them altogether may very well lead to erroneous results when deciphering the signals returned to the echosounder.

The size of the excess absorption due to nonlinear effects is dependent on several factors, the transmitted frequency being a major one. Nonlinear effects may be a problem for frequencies of and above 120 kHz (Pedersen 2006), which are operating frequencies commonly used in fisheries research. Operating frequencies are chosen for the best trade-off between range and accuracy for the problem at hand.

The initial peak intensity and the propagation distance are also important factors. Tichy *et al.* (2003) simulated and performed measurements on the

beam axis of the field from a 200 kHz echosounder. They found the excess attenuation to be dependent of both range and transmitted power, and in some cases the nonlinear loss reached several decibels. This indicates that nonlinear effects should be compensated for, to attain correct estimates.

1.2 Objective of this thesis

The objective of this thesis is in essence twofold.

The first focus lies on the development of a simulator for linear and nonlinear propagation of acoustic fields. Techniques reported in literature for such simulations form a basis for the development of the simulator. Calculating diffraction is based on the angular spectrum approach (ASA), and nonlinear effects are added according to a frequency domain solution of Burger's equation (FDSBE).

The simulator should calculate the field accurately, and be applicable to transducers of arbitrary shapes. This is an extension to the case of circular symmetric sources, implemented by Synnevåg in his thesis (1998). Fjellestad (2000) implemented such an extension using as a starting point a program he received from Kai Thomenius. The use of many loops due to memory issues made his code slow. Matrix operations are used to a larger extent in this thesis to improve computation time. The algorithm is also extended to the use of a second order operator-splitting technique. The possibility of enlarging the stepsize as a result of this will be investigated.

The results obtained by Fjellestad and Synnevåg showed some differences compared to measurements reported in literature. A priority in this thesis has been to unveil and correct this problem. Effort has been made to implement the algorithm accurately and verify its credibility. The problems considered in this thesis involves the propagation of fields from sonars and echosounders. The simulator is however applicable to general ultrasonic fields, and may be applied to problems involving medical ultrasound as well.

The second objective is to investigate the nonlinear loss and the field of the second harmonic for a source commonly used in fisheries research. The axial field of a 200 kHz transducer is simulated, both linearly and nonlinearly, to investigate the size of the nonlinear effects. It is possible that neglecting these effects leads to an erroneous estimate of target strength, and that they should be accounted for.

It might also be possible to utilize the second harmonic in imaging situations in fisheries acoustics, or in target strength measurements. This is common in medical ultrasound today through a technique called Tissue Harmonic Imaging. The range and quality of the beam of the second

harmonic will determine if an analogous technique is applicable in sonars.

The thesis aims to briefly introduce the subjects of fisheries acoustics and target strength to the reader unfamiliar with these topics.

1.3 Synopsis

The present chapter gives a short introduction to the topics discussed in this thesis and a layout of the work herein.

The basic theory of waves and their propagation is summarized in Chapter 2. The general idea of diffraction is presented.

Chapter 3 describes the basics of echosounding and other relevant concepts in the field of fisheries acoustics.

The linear propagation of sound is the subject of Chapter 4. The angular spectrum approach is presented as a means for calculating diffraction. Also introduced in the same chapter is the algorithm for linear field propagation, along with some pertinent issues concerning its implementation.

The algorithm is further extended to nonlinear field propagation in Chapter 5, which deals with the nonlinear propagation of sound waves. The cause of nonlinear effects and their implications are given. After presenting a substep for calculating nonlinear effects, some issues regarding the implementation is discussed.

Chapter 6 is devoted to verifying the performance of the simulator. It will be tested on linear and nonlinear field propagation, for circular symmetric and non-symmetric sources, and the results are compared with those reported in literature. Also the choice of stepsize is discussed.

In Chapter 7, simulations for a 200 kHz transducer is performed, and the results are presented and discussed in view of the objective of this thesis.

Chapter 8 summarizes the results obtained throughout this thesis, and suggests some points for future investigation.

The bibliography follows Chapter 8, alphabetized by the surname of the first author.

Appendix A lists the nomenclature, Appendix B contains some useful definitions and derivations and Appendix C lists parts of the source code for the simulator. Finally, Appendix D includes some additional figures.

1.4 Approach

At the commencement of the work on this thesis, the very field of signal processing was unfamiliar to the author. To be able to write this thesis, a vast amount of theory and literature needed to become acquaint posthaste.

To quickly get an overview of the problem, a series of colloquia was held at the center for Digital Signal Processing and Image Analysis (DSB) from January to mid March 2008.

Involved in the colloquia were myself, my supervisors, PHD student Ann Blomberg, and master student Thoril Kristiansen. Thoril's thesis dealt with a subject similar to mine, and articles of fundamental importance to both theses were presented and discussed. After the completion of the colloquia, the work on the theses has been carried out individually.

A course on signal processing was taken by the author parallell to the work on this thesis.

Chapter 2

Theory of acoustic propagation

This chapter is devoted to the underlying physical laws of wave propagation, and will form a necessary basis for understanding the different topics in this thesis. Elements in this chapter can be found in elementary books on physics and wave propagation, such as that by Young and Freedman (2004).

The basics of sound waves and their propagation are given in Section 2.1. Section 2.2 deals with the wave equation and its solutions. Section 2.3 describes diffraction; a phenomena that leads to the definition of the Rayleigh-Sommerfeld diffraction formula, which will be used in later chapters.

2.1 Sound waves

Whenever a system is disturbed from equilibrium and the disturbance can propagate, we have a wave. Waves are excellent carriers of energy, which we take advantage of in signal processing, trying to extract as much information about our surroundings as possible. One type of waves are the mechanical waves, waves that propagate through a medium. The mechanical waves most experienced by humans in everyday life are sound waves.

Sound waves are longitudinal disturbances of a medium, often a disturbance of density. Something sets the particles of a compressible fluid or solid in motion. Trying to return to the state of equilibrium, the particles thus undergo oscillatory motion. This in turn affects the neighboring particles and transfers the energy to them. This is what makes the waves propagate through the medium. It is also the reason why sound waves cannot exist outside a medium, as opposed to electromagnetic waves which propagate easily through vacuum.

As it propagates, the sound wave alternately compresses and decompresses the medium. This makes the density, and thereby the pressure,

fluctuate about their equilibrium values. Regions of increased density are called compressions, while regions of reduced density are rarefactions. The oscillatory motion is parallel to the direction of propagation, thereby the term longitudinal. Waves can also be transversal, wich means that the particle motion is normal to the direction of propagation. Electromagnetic waves are examples of transversal waves.

Compressions make up wavefronts of an acoustic wave, as illustrated in Fig. 2.1. Wavefronts are loci of points having the same phase, traveling in space with the propagation speed c. The value of c is generally dependant on the characteristics of the medium. The distance between two successive compressions is called a wavelength, denoted λ. During the time it takes to travel this distance, the wave completes a cycle. This time is known as the period T of the wave, given by $\mathrm{T} = \lambda/c$ and measured in seconds.

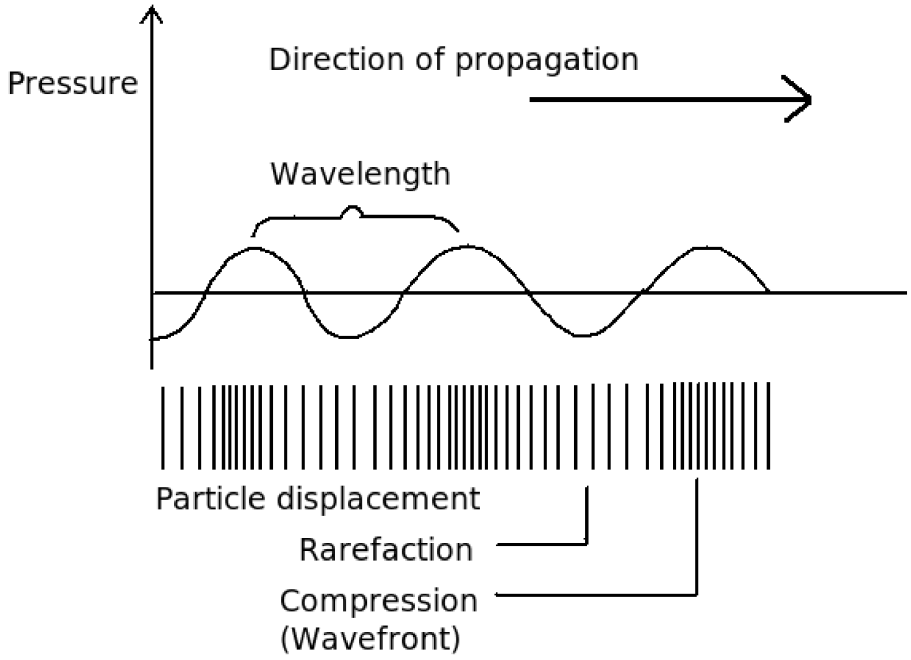

Fig. 2.1: Compressions of a traveling sound wave make up the wavefronts of the wave, separated by one wavelength λ.

The reciprocal of T is the frequency of the wave. It tells us how many cycles that are completed per unit time, measured in hertz (1 Hz = 1 s^{-1}). Frequency thus is given by

$$f = \frac{1}{\mathrm{T}} = \frac{c}{\lambda}.$$

The shorter the wavelength, the more compressions per second, and we have a higher frequency.

Audible sound is the range of frequencies to which the human ear is sensitive, from about 20 Hz to 20 MHz. Sound waves with frequencies below this region are termed infrasonic, and the ones above are termed ultrasonic. The ultrasonic frequencies are the ones used in medical ultrasound and most sonars.

Scattering of sound waves

The medium that carries the wave is called a transmission medium. All waves are influenced by the physical properties of their transmission medium. When the wave encounters a density difference, parameters of the wave changes as well, and part of the energy might be reflected as an echo. This could happen at the boundary between two different media. The amount of energy reflected is determined by the material properties of the new medium. The rest of the energy is either transmitted through the new medium or absorbed, for example by being converted to heat.

With sonars we send acoustic waves through water, as will be elaborated in Chapter 3. When the sound wave hits a new medium or an object, for example the bottom, an echo will propagate outward from that point. Echoes that return to the source are termed backscattered sound, and echoes that proceed further to some other receiver are termed forward-scattered sound. We can then analyze the information carried by back-scattered sound waved to gain insight into the cause of their reflections. The same principle is used in medical ultrasound; ultrasonic sound waves are sent through the body, and the transducer converts the reflected energy to electric voltages, which are used to obtain an image.

2.2 The wave equation and the equation of state

The governing equation for any wave propagation is the wave equation. This will be defined in the following, along with some of its solutions.

When the transmission medium is in its equilibrium state (i.e. no sound present), it is described by the variables $\mathbf{v}_0$, ρ_0 and p_0. These are initial velocity, ambient density and ambient pressure, respectively. When sound is present, these attributes fluctuate about their ambient states, and we have

$$\mathbf{v} = \mathbf{v}_0 + \mathbf{v}', \quad p = p_0 + p' \quad \text{and} \quad \rho = \rho_0 + \rho'. \tag{2.1}$$

The prime values here denote the perturbations from the ambient state. Here, p is a function of density, as formulated by the equation of state; $p = p(\rho)$. A Taylor series expansion of the equation of state about 0 gives

$$p' = (\frac{\partial p}{\partial \rho})_0 \, \rho' + \frac{1}{2!}(\frac{\partial^2 p}{\partial \rho^2})_0 \, (\rho')^2 + \cdots , \tag{2.2}$$

or more concisely (Hamilton and Blackstock 1998)

$$p' = A(\frac{\rho'}{\rho_0}) + \frac{B}{2!}(\frac{\rho'}{\rho_0})^2 + \frac{C}{3!}(\frac{\rho'}{\rho_0})^3 + \cdots , \tag{2.3}$$

where

$$\begin{aligned} A &= \rho_0 \, (\frac{\partial p}{\partial \rho})_0 \equiv \rho_0 c_0^2, \\ B &= \rho_0^2 \, (\frac{\partial^2 p}{\partial \rho^2})_0, \\ C &= \rho_0^3 \, (\frac{\partial^3 p}{\partial \rho^3})_0. \end{aligned} \tag{2.4}$$

Note that the expansion must be carried out under adiabatic conditions. If the perturbations are small, so that $p'/p_0 << 1$, we keep only the first term of Eq.(2.3), giving us a linear relationship between pressure and density. We may then consider the propagation as linear, as described by the homogeneous wave equation:

$$\boxed{\nabla^2 s = \frac{1}{c^2}\frac{\partial^2 s}{\partial t^2}} \tag{2.5}$$

where ∇^2 represents the Laplacian operator (often denoted $\triangle$)

$$\nabla^2 \equiv \frac{\partial^2}{\partial x^2} + \frac{\partial^2}{\partial y^2} + \frac{\partial^2}{\partial z^2},$$

and s represents some general field, for example pressure or velocity.

In Chapter 5, we will consider nonlinear propagation, where we keep more than one term from Eq.(2.3). We will define the parameter B/A, and see how it affects the waveform as the wave propagates.

Solutions of the wave equation

Being a partial differential equation, Eq.(2.5) can be solved by assuming a separable solution of the form

$$s(x, y, z, t) = f_1(x) f_2(y) f_3(z) f_4(t).$$

Let us now make an initial guess that $s(\mathbf{x}, t)$ has a complex exponential form

$$s(x, y, z, t) = a\, \mathrm{e}^{j(\omega t - k_x x - k_y y - k_z z)}, \tag{2.6}$$

where a is a complex constant and ω, k_x, k_y and k_z are real constants. The reason for this particular guess will be made clear later. Substituting this expression for $s(\mathbf{x}, t)$ into Eq.(2.5), we arrive at

$$k_x^2 s(x, y, z, t) + k_y^2 s(x, y, z, t) + k_z^2 s(x, y, z, t) = \frac{\omega^2 s(x, y, z, t)}{c^2} \Rightarrow$$

$$k_x^2 + k_y^2 + k_z^2 = \frac{\omega^2}{c^2}.$$

So we see that, if Eq.(2.6) is to be a solution of the wave equation, this constraint needs to be met. Letting $\mathbf{k} = k_x \hat{\mathbf{i}}_x + k_y \hat{\mathbf{i}}_y + k_z \hat{\mathbf{i}}_z$, this becomes $c^2 = \omega^2/\mathbf{k}^2$. We can now rewrite Eq.(2.6) to

$$\boxed{s(\mathbf{x}, t) = a\, \mathrm{e}^{j(\omega t - \mathbf{k}\cdot\mathbf{x})}} \tag{2.7}$$

the equation of a monochromatic plane wave with amplitude a and angular frequency ω. This might be easier to see by means of the familiar Eulers' formula

$$s(\mathbf{0}, t) = a\, \mathrm{e}^{j\omega t} = a\, \cos \omega t + ja \sin \omega t.$$

At some time t, the value of s will be the same at all points in planes where $k_x + k_y + k_z =$ constant. This is why we call the wave a plane wave. The term '*monochromatic*' means '*one color*', referring to the fact that ω is a constant. The wave travels in the direction of $\mathbf{k}$, which is called the *wavenumber vector*, and its magnitude has the unit of radians per meter. It can therefore be interpreted as a spatial frequency variable, analogous to the temporal frequency variable ω.

A spherically symmetric solution

The wave equation can be restated in the spherical coordinates (r, θ, ϕ), where $\phi = \arctan(y/x)$ and $\theta = \arccos(z/r)$. For spherically symmetric problems, the wave equation will only be dependant on r, and becomes

$$\frac{1}{r^2}\frac{\partial}{\partial r}\left(r^2 \frac{\partial s}{\partial r}\right) = \frac{1}{c^2}\frac{\partial^2 s}{\partial t^2}. \tag{2.8}$$

A solution to this equation is the monochromatic one:

$$s(r,t) = \frac{a}{r} \mathrm{e}^{j(\omega t - kr)}, \tag{2.9}$$

a spherical wave propagating outward from the origin. For spherical waves, the radii r of the wavefronts increase as the wave propagates, and the energy inherently spreads out over a larger area.

2.3 Diffraction

Generally, sound spreads spherically with intensity I from a source of finite extent, and the sound intensity decreases inversely with the square of r, $I \propto 1/r^2$. Sufficiently far from the source, however, in the far-field region, the waves can be regarded as plane. For a plane wave, the wavefronts are parallel planes of constant phase, as shown in the previous section.

Huygens' principle

Consider a plane wave impinging on a wall of such material properties so that it completely reflects the wave. Now assume there is a hole in the wall of finite extent that lets parts of the wave through. After passing the wall, the wavefronts are no longer plane, but have instead assumed a spherical form, much as if they were radiated from an aperture of finite size. This phenomenon is an example of diffraction; bending of wavefronts due to obstacles in their path.

Diffraction occurs whenever the wave encounters an obstacle, but the term is mostly used for situations where the size of the obstacle is of the order of a wavelength. This is because the amount of diffraction is dependant on the size of the hole or aperture measured in wavelengths. A large hole compared to the wavelength gives less spreading of the waves, and the wavefronts are more plane in the middle, see Fig. 2.2(a).

A theory on the diffraction phenomenon was postulated in 1678 by the Dutch physicist Christian Huygens (1629-1695). Consider each point on a traveling wavefront at a time t as a point source of secondary, spherical wavelets. The propagation of the wave can then be realized as the envelope of these wavelets at time $t + \delta t$. Hence, the addition of all the wavelets forms the new wavefront. This is known as the Huygens' principle, and is illustrated in Fig. 2.2.

Huygens' principle also explains why we can hear around corners. If a sound is generated anywhere inside a room with an open door, a person in

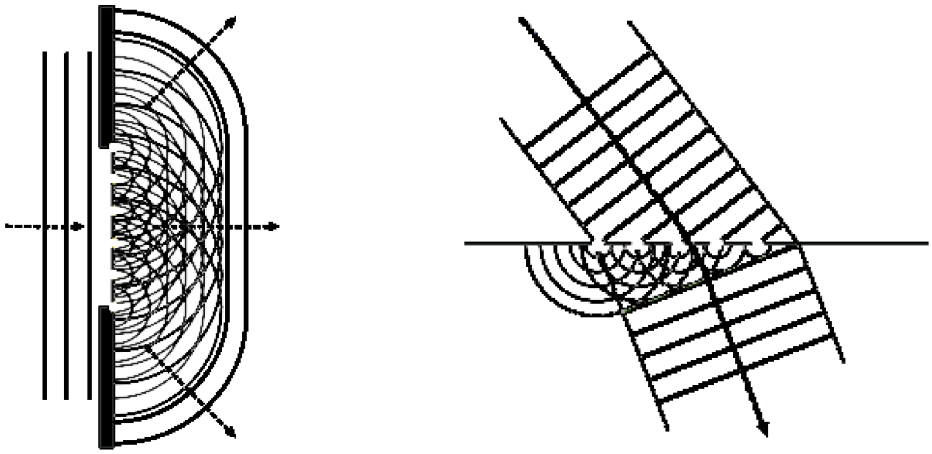

(a) Diffraction (b) Refraction

Fig. 2.2: Huygens' principle: Points on a traveling wavefront are sources of secondary wavelets. The sum of these wavelets forms the new wavefront at some later time.

the adjacent room will hear the sound as if it originated at the doorway. To that person it seems as though the source of the sound is the air within the doorway. Diffraction does however not help us to see around corners; the doorway is too large with respect to the short wavelengths of visible light. An extremely narrow slit would be needed to bend lightwaves to a large extent. However, the effect is visible through the unsharp edges of shadows.

The Rayleigh-Sommerfeld diffraction formula

Many physicists would later refine the idea of Huygens' principle, and effort was made to give it a mathematical foundation. One of the results is the Rayleigh-Sommerfeld diffraction (RSD) formula, given by

$$p(x,y,z) = -j\omega\rho \iint_S v(x',y',0)\,\frac{\mathrm{e}^{jkr}}{2\pi r}\,dx'dy', \tag{2.10}$$

where S is the size of the aperture, $dx'dy'$ is an infinitesimal patch of area located at $(x',y',0)$ and k is the wavenumber magnitude, $k = 2\pi/\lambda$. Here, r is the distance to the point (x,y,z)

$$r = \sqrt{(x-x')^2 + (y-y')^2 + (z)^2}.$$

The RSD formula determines the field distribution in a certain point, either given as pressure or velocity. Basically, the formula states that at some point $\mathbf{x}$, the wavefield $p(\mathbf{x})$ or $\mathbf{v}(\mathbf{x})$ can be represented as a superposition of fields originating in the hole S. Each field is weighted by a spherical spreading function, in which we recognize the factor $1/r$ from the spherically symmetric solution above. The sum will be determined by the relative phases and the amplitudes of the individual fields.

The RSD formula will be explained further in Chapter 4 when it is used to define a method for calulating field propagation: The angular spectrum approach.

Chapter 3

Underwater acoustics

This chapter deals with sound propagating under water, known as underwater acoustics or hydroacoustics. It will introduce concepts that will be important in later chapters of this thesis.

A general introduction to sonars and their use in water is given first in Sections 3.1 and 3.2. Section 3.3 introduces the field of fisheries acoustics, which is hydroacoustics applied to areas which concern fishing or research on fish. Parameters that are important in this field, as well as in this thesis, will be defined in the same section.

3.1 Introduction

The sea, and the life existing within it, has fascinated mankind throughout all of history. Its vast extent and great depth, seemingly unattainable, have given rise to many myths over the years.

Aquatic, living organisms have been an important source of food since the development of tools, and in modern times they have become of great economic importance as well. The acts of catching, breeding and selling fish support many livelihoods to this day.

But fishing and the very presence of man has had a huge impact on ocean environment. Overfishing has lead to the extinction of many species. Damage to the animals' habitats and the accidental killing of non-target populations continues to be of great concern.

The authorities introduced fish quotas as an attempt to avoid over-exploiting the fish stock. To be able to set such quotas accurately, one needs to estimate the abundance, the current size of a population of fish. As we shall see, underwater acoustics can be used for this purpose.

The fact that sound travels through water easily has been known since

the medieval times. In 1490, Leonardo da Vinci wrote in one of his notebooks (Urick 1983) that '*If you cause your ship to stop, and place the head of a long tube in the water and place the outer extremity to your ear, you will hear ships at great distances from you*'. The idea of the air-filled tube was still used in World War I, only they used in addition a second tube to the other ear, to determine directions to the enemy's submarines.

Sound travels through water better than any other known form of radiation. Light waves are attenuated to a large degree, and penetrates a few meters at the most. This fact led to the development of the echosounder and other acoustic instruments used to explore the sea.

3.2 Basic principles of sonars

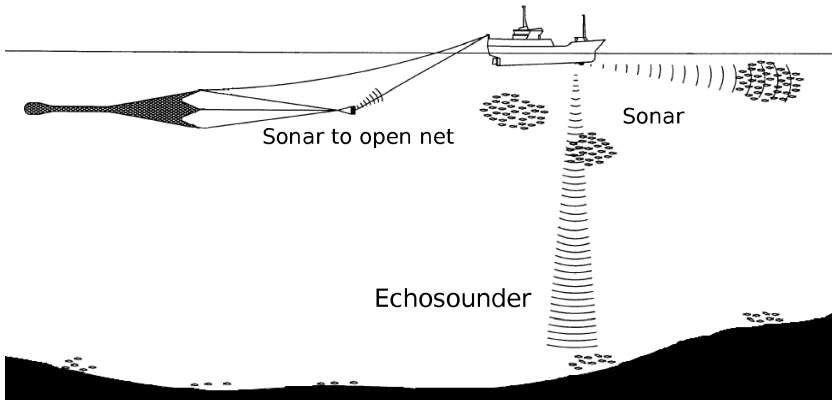

Fig. 3.1: Illustration of echosounding and sonar used for fishing. Most fishing vessels today have some form of this equipment installed. (Illustration based on Fig 1 given by Misund (1997).

Sonar (sound navigation and ranging) is a technique that uses the propagation of sound, mainly underwater, to locate objects and to communicate with other vessels. Today this technique is used extensively for ship navigation, as well as in fisheries and marine research. The term 'sonar' is used for the equipment that receives and/or transmits sound, as well as the associated software.

Sonars can be either active or passive. Passive sonars listen without transmitting, like da Vinci's air-filled tube could be an example of. A hydrophone is the aquatic equivalent to the microphone in air, and can be used to listen to underwater sound. The active sonar sends out single or

repetitive short (e.g. 0.2 - 1 ms) sound pulses and then listens for echoes of them. These echoes will then be the backscattered sound, as described in Chapter 2.

Scatterers

The object reflecting the wave is termed a scatterer. If the target is small compared to the wavelength, it will be subjected to the same amount of pressure throughout its volume. It will then contract and expand according to the oscillations, and act as a point source, spherically spreading scattered waves. This is illustrated in Fig. 3.2(a). If, on the other hand, the scatterer is very large compared to the wavelength and of a smooth surface, the scattered waves will emanate in one direction, as shown in Fig. 3.2(b)

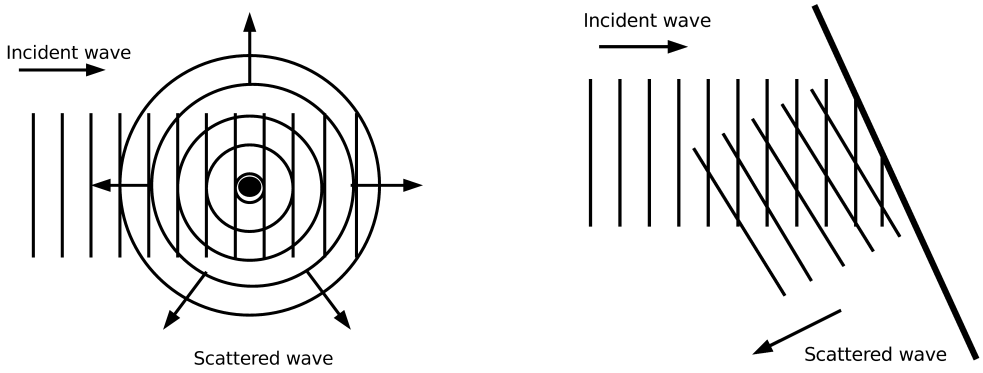

(a) Scattering by a small target. The scatterer acts as a point source and the scattered wave is spherical.

(b) A large scatterer reflects the waves in a single direction if the surface is smooth.

Fig. 3.2: Scattering of sound by objects of different sizes.

Transducers

The device that converts energy from one form to another is called a transducer. It is made from a piezoelectric ceramic material which generates electric potentials as a result of being deformed. The effects is reversible, so directly applying an electric field will cause mechanical stress in the material. This makes the transducer transmit and receive sound. In transmit mode, it converts electric energy into an acoustic pulse, which is transferred to water.

In receiving mode, the echo is converted to an electric signal that can be processed. Transducers come in different sizes and shapes, and may consist of several individual elements or be one continuous structure (a piston).

The performance of transducers has improved greatly over the last decades, as a result of developing materials of better converting capabilities and otherwise improving their design.

A vast amount of research has been spent on meliorating the beampattern of transducers, to reduce the beamwidth or lower the sidelobe levels. This may in part be accomplished through shading or weighting of the transducers elements.

Echosounders

Echosounders are active sonars used to transmit sound vertically into water (Simmonds and MacLennan 2005), as shown in Fig. 3.1. The echosounder is connected to a transmitter, which produces electrical energy bursts at the desired frequency. This is converted to acoustical energy by the transducer, and the result is a directional beam aimed downwards. For single-beam (one frequency) echosounders, the beamwidth is proportional to the size of the transducer divided by the frequency used. It is typically between 5 and 15 degrees, but not necessarily equal in the along-ship and athwart-ship directions.

The first to file a patent application for echo ranging was L. F. Richardson in 1912 (Urick 1983). The Titanic had sunk five days past, and he was motivated to discover a way to detect icebergs remotely. Richardson's idea was to use airborne sound to do this. He also applied for a patent for echo ranging under water, a month later. However, he made no attempt to build a device for this purpose, and so the first patent for an echosounder was obtained in 1913 by Alexander Behm.

Although not very suitable for finding icebergs[1], the echosounder turned out to be an excellent device for measuring the depth of the sea. The research on echosounding was sped up when the need to detect submarines emerged during World War I.

[1]Reginald Fessenden made a similar construction with his 'Fessenden oscillators', installed in United States submarines during World War I. He was able to detect an iceberg at a distance of two miles using this device (Urick 1983). Fessenden oscillators operated at frequencies of 500 and 1000 Hz.

3.3 Fisheries acoustics

With the aid of echosounders, acoustics can be utilized to study aquatic environments and the organisms therein. Marine animals may be located, mapped and counted by means of propagating sound. This is of particular interest to e.g. marine researchers and fishers. Using sound saves time and money, as one need not set traps and catch animals that are not of interest. It works in turbid waters, large volumes of water may be searched quickly, and it is also noninvasive.

This does not necessarily mean that animal life is not affected by the presence of sound. In addition to intentional use of underwater acoustics, man's general activities in and on water all contribute to noise pollution. These include amongst others the search for oil and gas, constructing oil rigs, drilling, shipping and laying pipelines.

Animals of the sea, particularly mammals, use sound naturally as a means of navigation, communication and hunting. Though not necessarily harmful, man made sound might disturb these animals to some extent. The impact of underwater sound on marine environments will not be considered further in this thesis, but has been studied by Heathershaw *et al.* (2001).

The first to use echosounders in the field of fisheries acoustics was R. Balls (Pedersen 2006), who conducted a series of experiments in the North Sea in 1933. Underwater acoustics has since been used for locating and counting aquatic organisms, so-called acoustic abundance estimates. Commercial fishers used this new technology combined with their prior knowledge of fishing sites and species' habits to locate schools of fish and to identify different species.

Locating fish with the aid of underwater acoustics has become increasingly important over the last years, and most fish caught by trawlers today have first been located by echosounders or sonars.

Underwater acoustics may also be used for behavioural studies, using subcutaneous acoustic tags. It is used to study more than fish. Large mammals such as whales often produce acoustic signals of their own, which may be recorded with the aid of a passive sonar. On the other end of the scale, we have the plankton, which often carry with them small bubbles of air.

Abundance estimation

As an echo returns to the source, two types of information are readily extracted; the time elapsed since the pulse was transmitted, and the sound pressure, or echo amplitude. The elapsed time tells us the distance to the

target, as the speed of sound in water is known for all temperatures, pressure states and salinities.

The sound pressure at the receiver is measured as intensity (unit W/m^2), energy flux per unit time. Instantaneous intensity is equal to the product of pressure and velocity

$$I_{\text{inst}} = pv = \frac{p^2}{\rho c}. \tag{3.1}$$

The intensity is then proportional to the density of organisms (Horne 2000), which can be estimated by using echo integration.

Echo integration means converting the sound pressures to volts and integrating over units of time. Multiplying the estimated density by the volume of water in the region of interest, gives an abundance estimate of that region.

If the packing density of fish is not too high, it is also possible to count echoes from individual animals, a procedure known as echo counting. Counting targets and dividing by the sample volume will then give an estimate of the density of targets.

Echo counting and echo integration is often combined with direct sampling, measurements made on tethered animals and prior knowledge to obtain better estimates.

Target strength and target identification

Knowing the existence and abundance of fish in an area is not enough. For this information to be useful, one needs to determine what species is responsible for the backscattered sound. Remote target identification has long been a goal of researchers and fishers. To experienced fishers, the location and depth of a school will give an indication of the species, but echosounding reveals more information than that.

The amount of sound that returns after hitting a target is dependant on a variety of factors. The size of the target is important, as previously discussed. The transducer used, how it is configured, the transmitted frequency and the location and behaviour of the target all affect the amount of back-scattered sound. The composition of the animal also matters, like the presence of a swimbladder, the stomach contents and the animals reproductive and maturation stage.

For fish with swimbladders, most of the backscattered sound ($> 90\%$) is due to the swimbladder (Simmonds and MacLennan 2005). The bladder contains gas, which reflects the waves almost totally. Some bladders also contain oil or fat. As the bladder is generally not spherical, the orientation

of the animal is not irrelevant. The axis of the bladder deviates slightly from the fish body axis, and so, maximum backscatter is achieved when the fish swims with its head down 5-10°.

Fig. 3.3: The backscattered sound intensity from a single small target. (Illustration: Pedersen (2006))

A measure of the amount of sound reflected by any one target at a certain frequency is the backscattering cross-section, measured in m^2. At any distance R from the source, it is given by:

$$\sigma_{\mathrm{bs}} = R^2(\frac{I_{\mathrm{bs}}}{I_{\mathrm{i}}}), \tag{3.2}$$

where I_{bs} is the intensity of the backscattered sound as shown in Fig. 3.3, and I_i is the incident intensity of the pulse, usually measured at unit distance. The backscattering cross-section will depend on the frequency response of the echosounder. In practice, the quantity measured is the effective backscattering cross-section, $\sigma_{\mathrm{bs,eff}}$, which is the weighted average of σ_{bs} over the bandwidth of the sonar

$$\sigma_{\mathrm{bs,eff}} = \int_0^\infty \sigma_{\mathrm{bs}}(\omega)P_{r0}(\omega)d\omega \Big/ \int_0^\infty P_{r0}(\omega)d\omega. \tag{3.3}$$

Here, $P_{r0}(\omega)$ is the power frequency response for the echo sounder.

If the density of organisms is too high for echo counting, one usually measures the volume backscattering coefficient s_v instead. This is the reflected intensity from a volume of scatterers. If we assume that all backscattered energy in a volume V comes from targets of interest, and that they are homogeneously distributed

$$s_v = \frac{1}{V}\sum_i \sigma_{\mathrm{bs},i} \approx \frac{\partial \sigma_{\mathrm{bs}}}{\partial V}, \tag{3.4}$$

where $\sigma_{\mathrm{bs},i}$ is the backscattering cross-section for the i-th scatterer. Fish of the same kind generally aggregate into schools that almost move as a whole, where all fish are oriented the same way. Hence, assuming that all $\sigma_{\mathrm{bs},i}$ are equal to σ_{bs} would not result in too much error in the density estimate.

The backscattering cross-section is used in defining target strength (TS)

$$\mathrm{TS} = 10 \log_{10}(\sigma_{\mathrm{bs}}). \tag{3.5}$$

Target strength is an important parameter in fisheries acoustics, measuring the echo returned by a single scatterer. Echo amplitudes are commonly expressed as target strengths, given in decibels. The larger the value of the TS is, the stronger the echo is compared to the transmitted pulse. For fish, TS is usually in the range -60 to -20, where -20 refers to stronger echoes.

The value of TS varies quite a lot between fish, even if they are of the same species and size. Even for the same fish the value of TS might not be constant for different measurements, because the fish's orientation may change. TS for a species must therefore be considered a stochastic variable, and its mean value is the average of many measurements. Note that this is the average of σ_{bs} values and not TS values themselves, because TS is a logarithmic measure of σ_{bs}.

TS of different types of fish has been measured *in situ* and on caged or even unconscious fish. Caged fish may be filmed while measurements are performed, to provide information about their tilt angles and behaviour. On the other hand, it is possible that the stress of being caught and caged affects the behaviour of the fish, so that they do not move in a way typical for their species.

The measurement of target strength is a main topic in this thesis. Nonlinear propagation of sound, as described throughout Chapter 5 might influence these measurements. This must then be accounted for before using them in abundance estimations. It might also be possible to obtain better measurements by exploiting nonlinear effects. This will be investigated further in later chapters. Fisheries acoustics and target strength will be revisited in Section 5.4, after introducing some important aspects of linear and nonlinear propagation of sound in the next two chapters.

Chapter 4

Linear propagation of acoustic fields and the ASA

In this chapter, a method for calculating linear diffraction will be presented. This method is called the angular spectrum approach (ASA). The ASA is often used to numerically simulate acoustic propagation, and has been exploited for this purpose in this thesis. The ASA has been widely implemented because it takes advantage of the powerful fast Fourier Transform (FFT), which reduces computation time.

The definition of the angular spectrum is given in Section 4.1, and in Section 4.2, the angular spectrum approach is presented. The resulting algorithm for linear field propagation is given in Section 4.3. This algorithm will be modified in Chapter 5 by including a nonlinear substep. Some known errors of the ASA and their remedies are presented in Section 4.4, before moving on to multistep propagation in Section 4.5.

For a more thorough derivation of some of the equations in this chapter, see Appendix B.

4.1 Definition of the angular spectrum

We will consider a sound wave traveling in space in the positive z-direction. The source of the wave is a plane transducer placed in the plane $z = 0$, which is thereby known as the source plane. The transducer vibrates with frequency f and the field in the source plane is denoted by $\mathbf{v}(x, y, 0)$.

The wave can be viewed as a collection of waves, each with its own wavenumber vector $\mathbf{k}$ and weight. The waves whose wavenumber vector points in or close to the direction of propagation carry the most weight. Had the source been a point source, however, the field would have been spherically

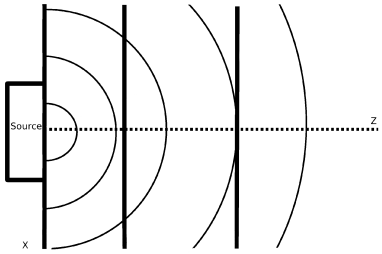

(a) Source plane and two successive planes.

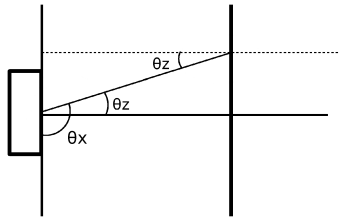

(b) Propagation angles of a plane wave.

Fig. 4.1: Geometry and coordinate system for the RSD formula.

symmetric, and all waves would have been weighted equally. Following Huygens' principle as described in Chapter 2, we may choose to view the transducer as a collection of such point sources. We then obtain a spatial frequency spectrum of the source field as the linear sum of their contributions. From theory (Johnson and Dudgeon 1993), we know that this is equal to the two-dimensional Fourier transform (given in Appendix B) of the aperture

$$V(k_x, k_y; 0) = \mathcal{F}\{v(x, y, 0)\} = \iint_{-\infty}^{\infty} v(x, y, 0) \mathrm{e}^{-j(k_x x + k_y y)} dx dy, \tag{4.1}$$

wherein we recognize the expression for plane waves from Eq. (2.7). Taking the two-dimensional Fourier transform of the field is equivalent to decomposing the field into a sum of plane waves (Christopher and Parker 1991b). Realizing this, Eq. (4.1) tells us that the plane wave with wavenumber vector $\mathbf{k} = (k_x, k_y, k_z)$ has weighting $V(k_x, k_y)$. Here, $k_x = k\cos(\theta_x) = k\, n_x$ and $k_y = k\cos(\theta_y) = k\, n_y$. Only the (k_x, k_y) components are needed because of the relation

$$k_z = \sqrt{k^2 - k_x^2 - k_y^2} = k\sqrt{1 - n_x^2 - n_y^2}.$$

We may rewrite the spatial frequency spectrum in Eq. (4.1) to obtain

$$V(n_x, n_y; 0) = \iint_{-\infty}^{\infty} v(x, y, 0) \mathrm{e}^{-jk(n_x x + n_y y)} dx dy. \tag{4.2}$$

The direction cosines n_x and n_y will form the orientation of $\mathbf{k}$ with respect to the coordinate axes, for each wave component. The concept is illustrated in Fig. 4.1(b). This makes the plane waves travel over a spectrum of angles, and Eq. (4.2) is thereby referred to as the angular spectrum. In literature, this term is also often used for Eq. (4.1), although this is not technically correct, as it is not expressed through its direction cosines.

4.2 The angular spectrum approach (ASA)

In Section 2.3, Rayleigh's integral (the RSD formula) was defined as a mathematical realization of Huygens' principle. As this is the starting point for our derivation of the angular spectrum approach (ASA), we will now consider this formula in more detail. Therefore, the RSD formula (Eq. (2.10)) is restated here

$$p(x,y,z) = -j\omega\rho \iint_S v(x',y',0)\,\frac{\mathrm{e}^{\,jkr}}{2\pi r}\,dx'dy', \tag{4.3}$$

where $r = [(x-x')^2 + (y-y')^2 + (z)^2]^{1/2}$.

The idea of the ASA is that a known field in a plane z_0 can be used to model the field in a parallel plane z_1 some distance Δz away. At each point on z_1, the field will be a sum of field contributions from all the points across the source plane, as is stated by the RSD formula. The field $\mathbf{v}(x,y,z_1)$ at z_1 could be calculated by taking the inverse transform of the angular spectrum $V(n_x,n_y;z_1)$. But diffractive propagation will cause the angular spectrum at z_1 to be different from that at z_0, so $V(n_x,n_y;z_1)$ is not known.

Luckily there is a linear relation between the two field profiles. This relation can be described by a two-dimensional transfer function $H(k_x,k_y;\Delta z)$ in the spatial frequency domain, or a point spread function $h(x,y;\Delta z)$ in the spatial domain. By defining (Zemp 2000)

$$h(x,y,\Delta z) = -j\omega\rho g(x,y,\Delta z) = -j\omega\rho\,\frac{\mathrm{e}^{\,jkR}}{2\pi R}\,, \tag{4.4}$$

where $R = (x^2+y^2+\Delta z^2)^{1/2}$ and $g(x,y,\Delta z)$ is the point source Greens function, we may rewrite Eq. (4.3) in condensed form. Through the definition of the Rayleigh integral, we may then view the field propagation as a convolution at $z = \Delta z$

$$p(x,y,\Delta z) = v(x,y) ** h(x,y;\Delta z), \tag{4.5}$$

where $**$ denotes two-dimensional convolution. It might be helpful to think of h as the impulse response of the system, relating diffractive propagation to the familiar case of linear, time-invariant filters.

It is a well known fact that convolution of two functions in the time or spatial domain is equivalent to inverse transforming the product of their Fourier transforms. Applying the convolution theorem to Eq. (4.3), and noting that (Williams 1983)

$$\mathcal{F}\left\{\frac{\mathrm{e}^{\,jkR}}{2\pi R}\right\} = j\frac{\mathrm{e}^{\,j\Delta z k_z}}{k_z},$$

we obtain a formula for the pressure field at Δz

$$p(x,y,\Delta z) = \frac{\omega\rho}{2\pi}\iint_{-\infty}^{\infty} V(k_x,k_y)\frac{\mathrm{e}^{\,j(k_x x+k_y y+\Delta z k_z)}}{k_z}\,dk_x dk_y. \tag{4.6}$$

Instead of pressure, one may choose to compute normal particle velocity. This is assumed to lead to less ripple in the results (Wu, Kazys, and Stepinski 1996b). Pressure and velocity is related to one another by the impedance relation (Williams 1983)

$$v = \frac{k_z}{k\rho c}\,\mathcal{F}^{-1}\left\{P\right\}, \tag{4.7}$$

which leads to the expression for the velocity field

$$\begin{aligned} v(x,y,z) &= \frac{1}{2\pi}\iint_{-\infty}^{\infty} V(k_x,k_y)\,\mathrm{e}^{\,j(xk_x+yk_y+\Delta z k_z)}\,dk_x dk_y \qquad (4.8)\\ &= \frac{k}{2\pi}\iint_{-\infty}^{\infty} V(n_x,n_y)\,\mathrm{e}^{\,jk(xn_x+yn_y+\Delta z n_z)}\,dn_x dn_y \ \text{ for } z\geq 0, \end{aligned}$$

where $V(n_x,n_y)$ is the angular spectrum as given in the previous section.

4.3 Implementing linear propagation

Eq.(4.8) is an exact expression for the diffraction of a linear velocity field. However, for most fields, an analytical solution to this formula cannot be found, and we need to find a numerical approximation. This is achieved by a numerical implementation of the ASA.

The angular spectrum approach is based on transforming and inverse transforming acoustical fields. This fact makes it possible to make use of the FFT in the calculations. Williams and Maynard (1982) computed a field using 4096 complex data points, and in this case the FFT increased the computation speed by a factor of 400 compared to a two-dimensional numerical integration. However, the use of a discrete Fourier transform can also seriously distort the results with bias errors. This is discussed in Section 4.4.

There are two different approaches to implementing linear diffraction. One samples h in the spatial domain, the other its transform H directly. In the articles by Christopher and Parker (1991a and 1991b), these methods are referred to as the spatially sampled convolution (SSC) algorithm and the frequency sampled convolution (FSC) algorithm, respectively. They applied the ASA to the case of circular symmetric sources, allowing them to replace the FFT with a quicker discrete Hankel transform. The following implementation is an extension to non-symmetric sources, a version akin to that of Wu *et al.* (1996a).

The linear algorithm

The algorithm is here presented for the 2-D case, but extension to the case of 3-D fields is straightforward.

1. Select a source plane of width D, being larger that the extent of the source, in the middle of which the source is located.

2. Determine a spatial sampling frequency F_s for properly sampling the source plane. The sampling interval will be given by $\Delta d = 1/F_s$, making the number of samples along the plane width $N = D/\Delta d$.
   Let the extent of the source be $2A$, so that the number of samples for the source is $L_x = 2A/\Delta d$. If L_x is odd, we need to correct for a half-sample length phase shift error, which will be shown in Section 4.4.

3. Using N and F_s as determined above, compute the samples of $v(x, 0)$ to obtain the discrete form $v_D(i_x \Delta d, 0)$, where $i_x = -(N/2)+1, \cdots, N/2$.
   Perform the DFT of $v_D(i_x \Delta d, 0)$ and obtain the angular spectrum $V_D(m_x \Delta f)$, where $m_x = -(N/2)+1, \cdots, N/2$ and $\Delta f = 1/D = 1/N\Delta d$ is the sampling interval in the frequency domain.

4. Compute the specified samples of $h(x, \Delta z)$, and find the DFT of them, $H(m_x \Delta f)$. Alternatively, sample $H(m_x \Delta f)$ directly.

5. At each point on z_1, obtain the acoustical field v_D by making a complex summation of the N plane waves. These waves travel in the directions $(n_x, n_z) = (\lambda m_x \Delta f,\ \sqrt{1-(\lambda m_x \Delta f)^2}\ )$ with amplitudes $V_D(m_x \Delta f)$. The summation is made by taking the inverse DFT of the complex product $V_D(m_x \Delta f) \cdot H(m_x \Delta f)$.

The i_x are discrete spatial indices of the source plane, as illustrated in Fig. 4.2. When implementing the algorithm, the spatial indices need to be positive integers, and we therefore introduce a shift by adding $(\frac{N}{2}-1)$ to the i_x -indices, creating a new set of spatial indices $i'_x = 0, 1, \cdots, N-1$. Now $i_x = (i'_x - \frac{N}{2}+1)$ and $x = (i'_x - \frac{N}{2}+1)\Delta d$.

The m_x are discrete spatial frequency indices. Having m_x range from $-(N/2)+1$ to $N/2$ means that all spatial frequencies larger than the Nyquist frequency are interpreted as negative spatial frequencies by subtracting N from them (Orofino and Pedersen 1993a). The DFT is however defined as a sum over spatial frequencies ranging from 0 to $N-1$ (see Appendix), so m_x needs to be shifted as well.

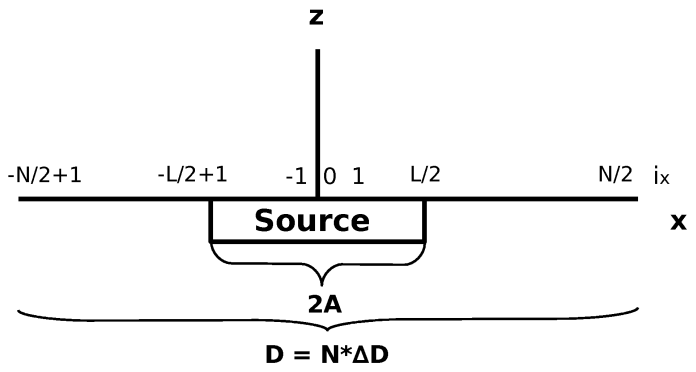

Fig. 4.2: Discretization of the source plane and source.

In the plane located at Δz, we can now calculate the field at each point by first obtaining the angular spectrum

$$V_D((m'_x - \tfrac{N}{2}+1)\Delta f) = \Delta d \sum_{i'_x=0}^{N-1} v((i'_x - \tfrac{N}{2}+1)\Delta d)\ \mathrm{e}^{-j\frac{2\pi}{N}(i'_x(-\frac{N}{2}+1))}, \qquad (4.9)$$

and then inserting it into

$$v_D((i'_x - \tfrac{N}{2}+1)\Delta d) = N\Delta f \, \mathrm{e}^{j\frac{2\pi}{N}(i'_x(-\frac{N}{2}+1))} \times \sum_{m'_x=0}^{N-1} V_D((m'_x - \tfrac{N}{2}+1)\Delta f) \, \mathrm{e}^{j\Delta z k_z} \mathrm{e}^{j\frac{2\pi}{N} i'_x m'_x}. \tag{4.10}$$

These equations are the numerical implementation of Eq. (4.8), and their derivations are given in Appendix B.

4.4 Errors in the angular spectrum

Wu *et al.* made a thorough investigation of the numerically implemented ASA in their papers (Wu, Kazys, and Stepinski 1996a, 1996b and 1997b). Following their argumentation, three problems arise when implementing the algorithm as is. Two aliasing errors are made, one in each domain, as a result of discretizing. Also, discretizing the source into an even number of samples makes the source center at $x = -\Delta d/2$, which creates a half-sample length phase shift. This shift error is easily removed by shifting the phase in the spectrum by the same negative amount – in other words, by multiplying V_D by $\mathrm{e}^{-j2\pi m_x \phi/N}$. Here, $\phi = 1/2$ when L is even, otherwise $\phi = 0$.

Spatial frequency aliasing and the DSFT

The first aliasing error is made in the spatial frequency domain, and is a result of performing the DFT on a source of finite size. This will not equal the exact angular spectrum, as is pointed out in the first article by Wu *et al.* (1996a). For a planar source with normal velocity distribution $u(x) = 1$, the analytical Fourier transform in discrete form is

$$V_D(m_x\Delta f) = L\Delta d \, \mathrm{sinc}\big(\frac{\pi L m_x}{N}\big) \, , \quad m_x = -(N/2)+1, \ldots, N/2 \, ,$$

but the phase corrected DFT for the same source is

$$V_D(m_x\Delta f) = L\Delta d \, \frac{\sin(\pi L m_x/N)}{L\sin(\pi m_x/N)}) \, , \quad m_x = -(N/2)+1, \ldots, N/2 \, .$$

The difference between the two is their denominators, and will grow with increasing m_x. Hence the difference is bigger for larger spatial frequencies $f_x = m_x\Delta F = n_x/\lambda$. This will ultimately overestimate the calculated near field.

A high sampling frequency will generally help reduce this aliasing error. From theory (Johnson and Dudgeon 1993) we know that the spatial sampling frequency must be larger than or equal to the Nyquist rate, which is 2 times the bandwidth of the signal. But, seeing as a finite source produces a band-infinite spectrum, the aliasing cannot be avoided.

In their article, Wu *et al.* propose a method called the discrete sinc-Fourier transform (DSFT) which eliminates the frequency aliasing error for planar sources. It is claimed that the analytical Fourier transform is obtained in a discrete form simply by multiplying the angular spectrum given by Eq. (4.9) with a sinc function. So, we obtain an exact angular spectrum given by

$$\begin{aligned} V_D((m'_x - \tfrac{N}{2}+1)\Delta f) = \ & \operatorname{sinc}(\frac{\pi m_x}{N})\ \mathrm{e}^{-j2\pi m_x \phi/N} \\ & \times\ \Delta d \sum_{i'_x=0}^{N-1} v((i'_x - \tfrac{N}{2}+1)\Delta d)\ \mathrm{e}^{-j\frac{2\pi}{N}(i'_x(-\frac{N}{2}+1))}\,. \end{aligned} \tag{4.11}$$

As the sum multiplied by Δd is simply the DFT of $\mathbf{v}(x,0)$, the FFT is still applicable.

Spatial aliasing – sampling and windowing

The other aliasing problem is the well known spatial aliasing error due to the intrinsic periodicity of the DFT's spectrum and undersampling of H.

One reason for this error is that the linear convolution in Eq. (4.3) becomes a circular convolution when using the discrete form of the Fourier transform (Oppenheim and Schafer 1999).

Whether or not these operations give the same result, is dependant on the length of the DFTs compared to the length of the sequences which are to be convolved. If the sequences are of lengths L and P, respectively, the operations are equal if the DFT is of length $L + P - 1$. This means that the sequences need to be zero-padded if this is not the case.

The circular convolution may be interpreted as having false replicated sources in the source plane, which may contribute in the far field and seriously distort the results there. Replicated sources vibrate in phase with the actual one, having the same velocity distribution. The sources are located along the source plane a distance D apart. Zeropadding the source plane will push them further apart, because this corresponds to a larger D. Hence the effect of the spatial aliasing will be moved further into the far field. Fig. 4.4 illustrates the idea of the zero-padding.

Spatial aliasing is also related to the undersampling of the transfer function H, which is the DFT of h. Inside the radiation circle

$$k_x^2 + k_y^2 = (\frac{2\pi f}{c})^2 \ ,$$

$H(k_x, k_y)$ has magnitude 1, and tapers off exponentially to zero beyond the circle. Waves with wavenumber vectors outside this region correspond to evanescent waves. The evanescent tail of H will be aliased back into the spectrum, but is typically of a negligible order if the steps Δz are of the order of a wavelength or smaller (Zemp, Tavakkoli, and Cobbold 2003). Zemp *et al.* found that, if large steps were to be used, aliasing became more of a problem.

On and about the radiation circle, H is subject to dense oscillations, and may become undersampled if waves of such propagation angles are allowed to contribute. Wu *et al.* discretized and plotted the magnitude and phase of H for a planar source using $\Delta f = 1/512\lambda$. The results show how the oscillations become denser for larger direction cosines n_x. For n_x beyond some critical value, H is undersampled. As $\Delta f = 1/D$, enlarging D implies a denser sampling in the spatial frequency domain. This will make the critical value of n_x larger. However, Zemp *et al.* claim that if the spatial frequency extent $k_{\max} = 2\pi/\Delta d$ contains a part of or all of the radiation circle, H cannot be sampled properly even if Δf is small. They then propose the sampling of h instead.

As Zemp *et al.* prioritized the use of large steps, they put much effort into finding an appropriate sampling scheme. They did not base their approach on choosing between the SSC or the FSC algorithm initially. Their algorithm samples h or H based on whether the angular range includes the radiation circle or not. How much of the circle that is included in the spatial frequency extent will determine whether to sample h or H, and the sampling interval needed in each step. This sampling interval may be different from the sampling scheme of the source plane. As might be clear from Chapter 5, this scheme may also be different for each harmonic in nonlinear propagation.

The use of a very large Δz has not been the top priority in this thesis, and the choice has been to apply the FSC algorithm. The affect this choice has on the stepsize is investigated further in Chapter 6.

To reduce the problems associated with the undersampling of H, a window is applied to the data, which forces the edges to be zero. The DFT will then repeat itself with a set of windowed data. The Tukey window is chosen, because it consists of a large plateau equal to one, which results in a large area of unaffected data. An example of a Tukey window is shown

in Fig. 4.3. The edges of the window are cosine-tapered, and outside the windowed region, the source plane is zeropadded, as shown in Fig. 4.4.

Applying a Tukey window in the spatial domain corresponds to a lowpass filter in the spatial frequency domain. This helps reducing the spatial aliasing problems, because waves of large direction cosines are not allowed to contribute. In effect, this reduces the angular range.

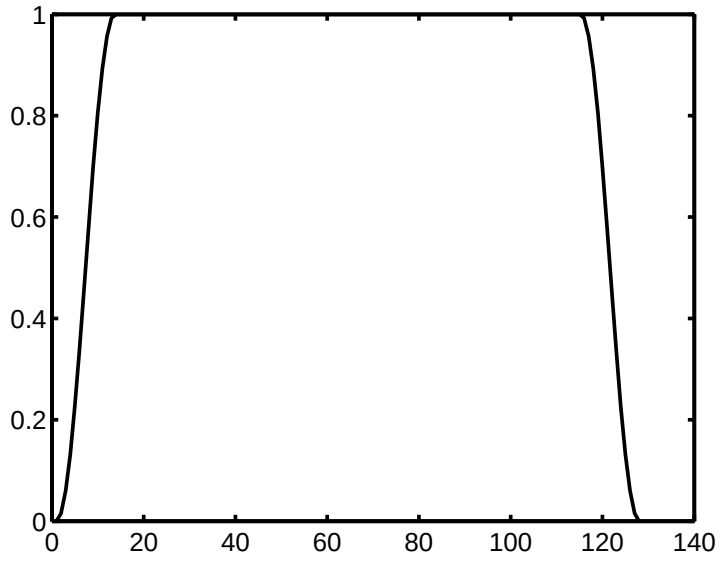

Fig. 4.3: Example of a Tukey window. This window is of length 128 and has a ratio of taper equal to 0.2.

If the angular range is truncated, it will lead to a great reduction of the spatial aliasing error (Orofino and Pedersen 1993a). Christopher and Parker used ray truncation to reduce the angular range in their papers (1991b and 1991a). Zemp *et al.* (2003) found that this was not appropriate for non-axisymmetric sources, because that would put a radially symmetric bound on a rectangular spatial frequency domain.

The angular range is also dependent on the choice of sampling frequency. The sampling frequency F_s should be chosen larger than the Nyquist rate in order to reduce spatial frequency aliasing. This will determine the maximal spatial frequency $f_{x\max}$, and thereby the angular range $n_{x\max}$ through the relations

$$|f_x| \leq \frac{F_s}{2}, \quad |n_x| \leq \frac{\lambda F_s}{2} \quad \text{and} \quad n_x = \lambda f_x \,. \tag{4.12}$$

As $D = N/F_s$, the spatial aliasing error is sensitive to the angular range for a fixed D. Choosing F_s wisely thus might help reduce spatial aliasing.

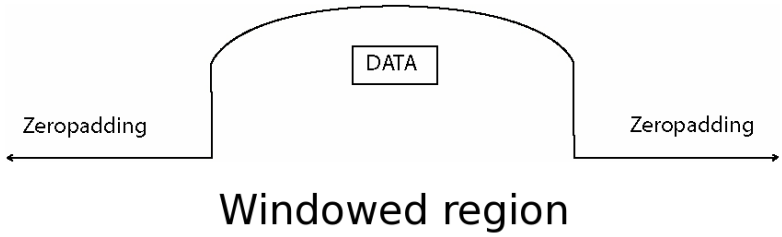

Fig. 4.4: Zero-padding and windowing of the source field. The source field is applied a Tukey window, and outside this windowed region, the source plane is zeropadded. This extends the length of the DFT so it becomes equal to N. The size of the zeropadded and windowed region is equal to D.

If $F_s = 2/\lambda$ the angular range is $n_x = \cos(\theta_x) = [-1, 1]$. In this case, all the plane waves are allowed to contribute to the field, and we cannot avoid the spatial aliasing. Increasing F_s above this will include evanescent waves, which only contribute to the extreme near field (Wu, Kazys, and Stepinski 1996a). A small angular range will however make the ASA less convergent, because some information is lost in the process. Most of the energy is contained in waves of small direction cosines, though.

Combination a large discretization size D and a high sampling frequency will result in a high computational burden, because the size of the DFT grows. Especially in the case of 3-D fields, this may cause problems with both memory and computation time. It suffices to say that there will always be a trade-off between the speed and the accuracy of the algorithm. The parameters used throughout this thesis will be presented in each case.

4.5 Multistep propagation

As mentioned previously, the intention in this thesis is to use the algorithm above to simulate nonlinear acoustic fields. To do so, a nonlinear substep will be added between adjacent planes. So far, we have implemented Eq. (4.10) by inserting z's directly into the transfer function. So, at each step the source plane has been the plane in which the source is actually located. The new field was calculated at ever growing distances z based on the DSFT spectrum of the actual source, given by Eq. (4.11). This method will from here on be referred to as single-step propagation.

To prepare for nonlinear propagation, we introduce a multistep version of the algorithm. In this version, the source field is updated to be the field in the plane just visited. Hence, the angular spectrum needs to be recalculated at each step. This is done by performing the DFT on the field recently output from the algorithm. The DSFT can no longer be used, as it is only valid for planar-like sources of finite extent. The multistep algorithm is investigated further in Chapter 6.

Chapter 5

Nonlinear wave propagation

The preceding chapters have dealt with the linear propagation of sound. In this chapter, the theory for nonlinear wave propagation is presented. A nonlinear version of the wave equation will arise in Section 5.2, and we will see how nonlinearity effects the waveform. An important application of nonlinear propagation, tissue harmonic imaging, is described in Section 5.3. Section 5.4 briefly discusses the effects of nonlinearity in fisheries acoustics. The chapter culminates in the algorithm for nonlinear propagation of acoustic fields, presented in Section 5.5. Here a nonlinear substep has been added to the linear algorithm. Some issues concerning the implementation of this algorithm is further discussed in Section 5.6.

Verification of the algorithm is done in the Chapter 6, for both linear and nonlinear examples.

5.1 Motivation

In 1686, Newton obtained the first formula for sound speed (Hamilton and Blackstock 1998)

$$b = \sqrt{\frac{P_0}{\rho_0}}, \tag{5.1}$$

based on an assumption that the relationship between pressure and density was linear

$$\frac{P}{P_0} = \frac{\rho}{\rho_0}.$$

This was known as Boyle's law at the time. Eq. (5.1) would later be known as the speed of sound in an isothermal gas, thereby the symbol b. However, Newton's calculations were around 16% lower than the

corresponding measurements. This fact remained a mystery for over a century until Laplace finally gave the explanation in 1816. The presence of sound will in fact change the local temperature of the gas, due to the compressions and rarefactions described in Chapter 2. So heat does not flow along with the wave propagation. For an adiabatic gas (Hamilton and Blackstock 1998)

$$\frac{P}{P_0} = (\frac{\rho}{\rho_0})^\gamma,$$

where γ is the ratio of specific heats. So, we see that the pressure-density relationship is actually not linear, and this affects the sound speed in the medium. The adiabatic sound speed given by Laplace is

$$c_0 = \sqrt{\frac{\gamma P}{\rho}}.$$

The field of nonlinear acoustics is in itself about as old as the linear one. The nonlinear wave equation, which will be presented below, was developed in the late 1750's (Hamilton and Blackstock 1998). In spite of this, it was still assumed that sound propagated in a linear fashion. There were a couple of reasons for this assumption. Most acoustical motions were considered small enough so that the nonlinear effects would be small compared to the linear ones. This would mean that sufficient results were obtained through linear modeling, and nonlinear effects could safely be neglected. Also, to solve the nonlinear equations would be mathematically difficult, if not impossible, without the aid of powerful computers.

The progress in the field has for these reasons been very slow, but for the last five decades or so, interest and activity in the field of nonlinear acoustics have increased. The improvements of computers have lead to relatively quick algorithms which allow us to solve problems that would have been impossible to solve a few years ago. The development of such an algorithm is one of the main goals in this thesis.

5.2 The nonlinear wave equation

In Chapter 2, we defined the linear wave equation. By making a small signal approximation, we kept only the first term from the Taylor expansion in Eq. (2.3). This gave us a linear relation between pressure and density, which led to the description of linear propagation.

However, neglecting higher power terms in the equations of motion will result in an approximation, only valid in the small signal limit. Many

applications use high amplitude ultrasonic fields, such as medical ultrasound and many sonars. In these cases, the initial pressure is larger than what is governed by the small signal limit, and the nonlinear effects are typically non-negligible. As we will see in Section 5.3, nonlinear effects may also work to our advantage in some situations. For these reasons, we need to be able to model finite acoustics as well. We begin by considering anew the equation of state.

A nonlinear and more accurate pressure-density relationship is obtained by retaining the first two terms of Eq. (2.2). (We assume constant entropy, and drop the third term.) In this case, Eq. (2.3) becomes

$$p' = A(\frac{\rho'}{\rho_0}) + \frac{B}{2!}(\frac{\rho'}{\rho_0})^2, \tag{5.2}$$

where $\rho' = \rho - \rho_0$ and $p' = p - p_0$. Remembering from Eq. (2.4) that

$$A = \rho_0 c_0^2 \quad \text{and} \quad B = \rho_0^2 (\frac{\partial^2 p}{\partial \rho^2})_0, \tag{5.3}$$

we can rewrite Eq. (5.2) to

$$p = c_0^2 \rho + \frac{c_0^2}{\rho_0} \left(\frac{B}{2A} \right) \rho^2.$$

A measure of the nonlinear effects are commonly expressed through the coefficient of nonlinearity

$$\beta = 1 + \frac{B}{2A}, \tag{5.4}$$

where the first term is due to convection, and the latter (B/A) is the nonlinear parameter. For a linear medium, $B/A = -2$ and $\beta = 0$. Typical values for β is 3.5 in freshwater and 4.6 for a dog's kidney.

The nonlinear wave equation arises from these new expressions as

$$\frac{\partial^2 \phi}{\partial t^2} - c_0^2 \triangle \phi = \frac{\partial}{\partial t} \left[(\nabla \phi)^2 + \frac{B}{2Ac_0^2} (\frac{\partial \phi}{\partial t})^2 + \frac{b}{\rho_0} \triangle \phi \right] , \tag{5.5}$$

where ϕ is the velocity potential, $\mathbf{v} = -\nabla \phi$. The absorption coefficient b is a constant determining the effects of viscosity and heat conduction. The derivation of Eq. (5.5) is beyond the scope of this thesis, but can be found in the book by Enflo and Hedberg (2002).

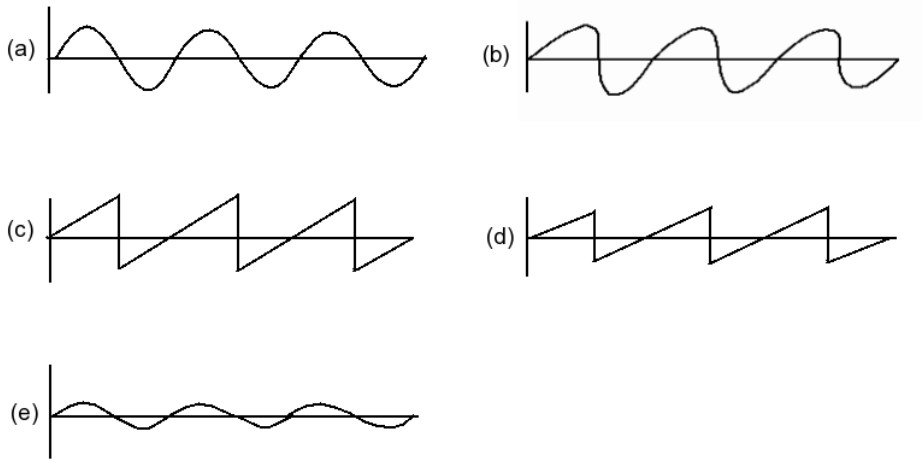

Fig. 5.1: Distortion of a transmitted sinusoid. Waveform shown at different stages. (a) Transmitted pure sinusoid of fundamental frequency. (b) Distortion becoming noticeable. Higher harmonics are generated and the fundamental loses energy to them. (c) Fully developed sawtooth wave. (d) Decaying sawtooth wave. The higher harmonics are attenuated. (e) Old age region. Only an attenuated version of the fundamental remains.

Nonlinear effects on the waveform

Nonlinear effects will contribute to the wave speed, which will be given by the Eularian speed of sound (Hamilton and Blackstock 1998)

$$c = c_0 + \beta v(\mathbf{x}),$$

where $v(\mathbf{x})$ is the particle velocity at point $\mathbf{x}$. This means that the wave speed is no longer determined entirely by the physical properties of the medium, but also depends on local particle velocities. The higher the value of β, the larger the nonlinear effect on the propagation speed will be.

The wave speed will generally be higher in compressed regions, causing the wave to travel faster through the medium during its compression phase. This is because the pressure and temperature is increased in this area. During a rarefaction, the opposite happens, and the wave will slow down as the water particles are drawn apart. This varying sound speed will in turn cause a distortion of the waveform. The distortion is accumulative, and will be more severe for higher amplitude waves, when $v(\mathbf{x})$ is larger.

Fig. 5.1 illustrates a transmitted pure sinusoid of frequency f_0. This initial frequency is known as the fundamental frequency of the wave. As it

propagates, the steepness of the wave will rise, and the sinusoid will gradually approach a shock wave if the attenuation in the medium is not too large. If the transmitted wave is a pulse, it might transform into a wave of triangular shape.

Distortion of the waveform in the time domain will generate higher components in the frequency domain. These are harmoniously related to the fundamental, i.e. their frequencies are multiples of the fundamental's frequency. Energy is transferred from the fundamental into the higher harmonics as the wave propagates, and more harmonics are generated as we go along. The higher harmonics will be dampened after propagating some distance, and only an attenuated version of the fundamental might exist in the far field. This is sometimes referred to as the old age region (Shooter, Muir, and Blackstock 1974). From here, small-signal attenuation is more important than the nonlinear effects.

There exists a number of formulas, valid for different regions and waves, to predict the distances to shock formation and old age region. Shooter *et al.* made an analysis of these distances for a source of radius 0.9144 meters and gave predictions for several peak source levels and fundamental frequencies. They focused their attention to the state of acoustic saturation. In this state, increasing the amplitude of the source additionally will not increase the amplitude at the receiver. This may happen if the nonlinear effects are large enough. All the excess energy from the source will then leak to higher harmonics and be attenuated.

Predictions of nonlinear effects and shock distances at different parameters are useful when performing measurements or simulations. If, for instance, the old age distance is shorter than the shock distance, no shocks will be formed. The wave will simply attenuate and the nonlinear effects are negligible.

Attenuation

Attenuation of the nth spectral component can be described by

$$v_n = (v_n)_0 \, \mathrm{e}^{-\alpha(n)z},$$

or

$$\frac{\partial v_n}{\partial z} = -\alpha(n) v_n,$$

where $\alpha(n)$ is an attenuation coefficient which depends on frequency. This is usually given by $\alpha(n) = \alpha_0 (n f_0)^2$, where α_0 is a constant, which gives a

quadratic dependency on frequency. By rewriting it to $\alpha(n) = \alpha_0(nf_0)^b$, we get a more general dependency, defined by b.

From these equations, it is obvious that waves with higher frequencies will be attenuated more. Hence, the penetration of higher harmonics is more shallow compared to the fundamental. This contributes to dampen the build-up of higher harmonics at large axial distances.

5.3 Harmonic imaging

The nonlinear propagation of ultrasound may be utilized to substantial advantage in imaging situations. A well-known example is the technique of harmonic imaging, described in the current section.

Ultrasound has been used in medical imaging for years, for example in diagnostics imaging, cardiology and fetal imaging. This is because it is relatively cheap and easy to use, and the apparatuses are portable compared to those used in magnetic resonance imaging (MRI) or computer tomography (CT). But the main advantage of using ultrasound is that it is non-invasive and safe for the patient. The disadvantages are that the images are not always of the best resolution, and the penetration is relatively shallow because tissue is a highly attenuating medium.

The lateral resolution is given by $\Delta l = \lambda F/A$, where F is the focal depth and A is the size of the probe. A larger probe would therefore help improve image quality. However, the size of the probe is often limited. For instance, for cardiac imaging, the probe can be no larger than the gap between the ribs. A larger probe would also be more expensive to manufacture.

A higher frequency would also generally improve the resolution. But higher frequencies are also attenuated more, as shown in the previous section, so there is a trade-off between resolution and range. Frequencies used in medical ultrasound range from 2 to 10 MHz, in rare cases up to 30 MHz. As this determines the range for the given transducer (up to about 20 cm for 2 Mhz) it also determines what may be imaged with this frequency. For instance, 30 MHz may be used for intravascular imaging, as it penetrates a couple of cm at the most. As shock waves could cause damage to tissue, this also limits the applicable frequencies.

Upon reception, the resolution will be determined by the width of the mainlobe, as is stated by the Rayleigh criterion[1]. A narrower mainlobe will

[1]The Rayleigh criterion is a classical definition of resolution, saying that two plane waves are resolved if the mainlobe peak of one aperture smoothing function replica falls on the first zero of the other. In other words, the resolution equals half of the mainlobe width.

give better resolution. The second harmonic generally has a narrower beam profile and lower sidelobe levels than the fundamental. The relative sidelobe levels are important because they give rise to clutter, or noise, in the images. Hence, if the receiver is set to receive at the frequency of the second harmonic, better resolution would be obtained. An additional benefit is that the second harmonic is easy to filter out from the transmitted fundamental.

Forming images based on the reception of the second harmonic is known as harmonic imaging. The narrower beam profile might of course be obtained simply by transmitting the frequency of the second harmonic. However, as attenuation increases with frequency, this leads to a shallower penetration, which is not desirable.

The benefits of harmonic imaging in medical ultrasound were discovered in the 1980's. Initially, tissue was assumed to be a linear medium, and gas-filled microbubbles called contrast agents were injected into the bloodstream to provoke nonlinear effects.

Tissue Harmonic Imaging (THI) became more common in the late 1990's (Averkiou, Roundhill, and Powers 1997). It was discovered that tissue is in fact a nonlinear medium, and no microbubbles are needed for harmonic generation. In THI, nonlinear effects are a result of nonlinear propagation and not nonlinear scattering, as in the case with contrast agents.

5.4 Nonlinearity in fisheries acoustics

As the accuracy and range of modern echosounders have increased, the excess attenuation due to nonlinear effects in water has become apparent. Some of the transmitted frequencies and power levels often used in fisheries research may generate nonlinear losses. If neglected, they will result in inexact estimates of the calculated field or target strength.

The frequencies used in fishery acoustics range from 200 Hz for small fish in shallow waters to 10 MHz for plankton (Horne 2000). For frequencies of 120 kHz and above, nonlinear losses are a potential problem (Pedersen 2006). This also depends on the acoustic level and the depth of the transducer.

Echo integration of echoes from transducers that operate at a single frequency is often used for abundance estimation of fish, as described in Chapter 3. Remember from Section 3.2 that the beamwidth is inversely proportional to the frequency. The chosen frequency then determines how well we can make measurements on small animals, because this determines the beamwidth for the chosen transducer. But there is a trade-off between this accuracy and the range of the beam, due to frequency-dependent attenuation. The choice of frequency therefore depends on the depth and

size of the targets of interest.

To increase the information we are able to obtain, several frequencies are often used simultaneously in modern echosounder systems. This might lead to more accurate results in discriminating different species.

Up to six different frequencies are used in multi-frequency systems. Most common are the dual-beam echosounders that use two frequencies. Nonlinear effects will then create waves with energy at the sum and at the difference of the two original frequencies. If the original waves are close in frequency, the sum frequency will be very high and the difference frequency will be low. The sum frequency signal will then be highly attenuated, but the difference frequency wave will have a much higher range than the fundamental frequency signals, though with a poorer resolution.

THI is today the default mode for medical imaging, and it is well known that this leads to improved resolution and clutter suppression in the images. The idea of using the principle of harmonic imaging in sonars arises quite naturally. By receiving at twice the fundamental frequency, it might be possible to exploit the nonlinear effects even with a single-beam transducer. This is generally not done today, because the bandwidths of typical sonars are too small to receive the second harmonic. Disregarding this particular problem, it is of interest to know if the second harmonic could be used for measuring target strength, or possibly in imaging situations. In view of this question, the development of the second harmonic of an appropriate source will be investigated in Chapter 7.

5.5 Implementing nonlinear propagation

Modeling finite amplitude sound beam propagation includes the effects of diffraction, attenuation and nonlinearity on each harmonic. This will be done in an incremental propagation where the fundamental v_1 and the harmonics v_n are propagated together in steps of length Δz. This is analogous to the multistep, linear algorithm, which was thoroughly described in Chapter 4.

An operator-splitting approach

We adopt the phenomenological method implemented by Christopher and Parker (1991a), and calculate the effects of diffraction, attenuation and nonlinearity separately. This operator-splitting technique is valid for small steps Δz, where these effects may be considered independent.

Diffraction is accounted for by means of the linear algorithm, and nonlinear effects are added to the result in a separate substep. The nonlinear

effects are calculated in the frequency domain via a Fourier series solution to Burgers equation, introduced below, which includes attenuation.

The operator-splitting technique may be written

$$\frac{\partial v}{\partial z} = L_{A,N,D} \cdot v \approx L_A \cdot v + L_N \cdot v + L_D \cdot v,$$

where L_A, L_N and L_D are operators which represent attenuation, nonlinearity and diffraction, respectively. We can obtain a diffraction sub-equation by considering only

$$\frac{\partial v}{\partial z} = L_D \cdot v,$$

to which a solution at $z + \Delta z$ is the propagation operator $\Gamma_{D,\Delta z}$. Similarly, we obtain the operators $\Gamma_{A,\Delta z}$ and $\Gamma_{N,\Delta z}$ as solutions to the attenuation and nonlinearity sub-equations.

The model used by Christopher and Parker is equivalent to a first-order operator splitting scheme

$$v(x, y, z + \Delta z; t) = \Gamma_{D+A,\Delta z}\Gamma_{N,\Delta z} v(x, y, z; t) + O(\Delta z^2).$$

So the effects of diffraction and attenuation are combined in their algorithm, whereas nonlinear effects are added in a separate nonlinear substep.

Zemp *et al.* (2003) use a similar approach in their model, but they gain considerable computational efficiency by using their second order operator-splitting scheme

$$v(x, y, z + \Delta z; t) = \Gamma_{D,\Delta z/2}\Gamma_{N+A,\Delta z}\Gamma_{D,\Delta z/2} v(x, y, z; t) + O(\Delta z^3).$$

The idea of the substeps in the operator-splitting method is illustrated in Fig. 5.2. The diffraction substep is divided into two smaller substeps $\Delta z/2$, and the nonlinear effects are added to the intermediate result. This approach allows for larger Δz, which implies that fewer steps are needed in order to reach the desired propagation distance. In the referred article, Zemp *et al.* claim to need only 23 fractional steps for a case where the algorithm of Christopher and Parker would require hundreds or thousands. For this reason, the second order operator-splitting approach has been chosen in this thesis.

However, Zemp *et al.*'s ability to use large stepsizes were not only a result of the second order operator-splitting approach. An important contributory effect was their adaptive sampling scheme, described in Section 4.4. As the

FSC algorithm is implemented in this thesis, we might expect to be forced to use a stepsize larger than Zemp *et al.*'s, but still larger than Christopher and Parker's. Different stepsizes are tested out in Chapter 6.

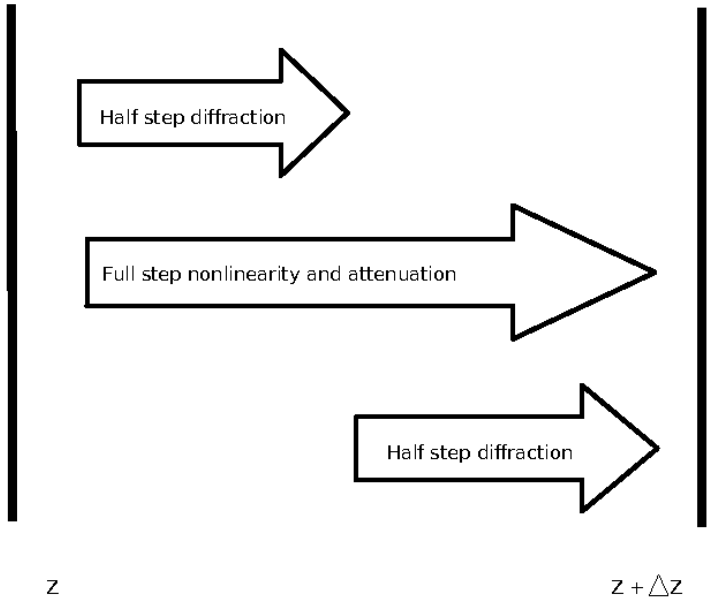

Fig. 5.2: Schematic of the second order splitting approach between two planes a distance Δz apart. The effects of diffraction, attenuation and nonlinearity are approximated to the second order.

Burgers' equation and the FDSBE

Solving the nonlinear wave equation, Eq. (5.5), might be impossible to do numerically, and so we use model equations to numerically calculate nonlinear propagation. If Δz is small, the incremental change of particle velocity v due to nonlinear effects and attenuation can be written

$$v(z + \Delta z, t) = v(z, t) + \frac{\partial v}{\partial z}\Delta z. \tag{5.6}$$

This is a truncated power series where higher order terms are neglected. To calculate $\partial v/\partial z$, a number of different models are available, each valid under different simplifying conditions. An excellent review of several approaches is given in the book by Hamilton and Blackstock (1998).

A widely used model equation is the nonlinear parabolic equation by Khoklov, Zabolotskaya and Kuznetsov, known as the KZK-equation. The

KZK-equation has a few drawbacks. It uses a parabolic approximation to calculate the field, which will not be valid in the near field region, or far off-axis in the direction of propagation. It is also only valid for thermoviscous fluids.

Another highly invoked equation is the Burgers' equation, given by (1983)

$$\frac{\partial v}{\partial z} = \frac{\beta\omega_0}{2c_0^2} v \frac{\partial v}{\partial \tau} + \Gamma \frac{\partial^2 v}{\partial \tau^2}, \tag{5.7}$$

which will also be used in this thesis. In this equation, $\partial v/\partial z$ is the differential change of particle velocity and $\tau = \omega_0 t - kz$. The constant Γ is related to thermoviscous dissipation, not to be confused with the propagation operator $\Gamma_{D,\Delta z}$ above.

In the nonlinear algorithm, we are interested in the differential change of the n-th harmonic separately. This can be written as

$$\frac{\partial v_n}{\partial z} = j\frac{\beta\omega_0}{2c_0^2} \sum_{k=-\infty}^{\infty} (n-k) v_{n-k} v_k - \alpha_0 (nf_0)^b v_n, \tag{5.8}$$

where the last term on the right hand side represents viscous losses (attenuation). The derivation of this equation can be found in the article by Haran and Cook, but there is an inconsistency in their notation which results in an error in the constant term. Their version should be divided by a factor 2 to give Eq. 5.8. The details of the reason for this error will not be described here, but are given in a comment by Trivett and Van Buren (1984).

To calculate Eq. (5.8) numerically, the series must be truncated to a finite number of harmonics. Calling this number M, and changing the summation term, the equation can be rewritten to

$$\frac{\partial v_n}{\partial z} = j\frac{\beta\omega_0}{2c_0^2} \left(\sum_{k=1}^{n-1} k v_k v_{n-k} + \sum_{k=n+1}^{M} n v_k v_{k-n}^* \right) - \alpha_0 (nf_0)^b v_n, \tag{5.9}$$

where $*$ denotes complex conjugation.

The first sum represents the sum frequency generation. In other words, this is the accretion of the n-th harmonic by combining other harmonics whose frequencies sum to nf_0. Likewise, the second summation represents depletion of the n-th harmonic to other harmonics with a difference frequency of nf_0. Eq. (5.9) can be referred to as the FDSBE, a frequency domain solution of Burgers' equation.

The nonlinear substep

The nonlinear substep consists of applying the FDSBE to the multi-harmonic field recently output by the linear substep. This field is the intermediate result at $z + \Delta z/2$, and will hereafter be denoted v', with the subscript n for the n-th harmonic.

Inserting Eq. (5.9) into Eq. (5.6), the $i_x i_y$-th iteration of the nonlinear substep may be written

$$v_n(i_x, i_y, z + \Delta z/2) = v'_n(i_x, i_y, z + \Delta z/2) + \frac{j\beta\pi f \Delta z}{c_0^2} \left(\sum_{k=1}^{n-1} k v'_k v'_{n-k} + \sum_{k=n+1}^{M} n v'_k v'^{*}_{k-n} \right) - \alpha_0 (n f_0)^b v'_n \Delta z, \quad n = 1, 2, \ldots, N. \tag{5.10}$$

Note that the $(i_x, i_y, z + \Delta z)$-terms have been dropped in the summations, to make the equation more readable.

Recall that i_x and i_y denotes lateral samples of the source plane. and the computation thus must be performed for all i_x and i_y for each harmonic. The FDSBE assumes that the solution can be represented by a finite number of harmonics, again denoted by M.

The nonlinear algorithm

The complete algorithm for nonlinear wave propagation can now be presented.

1. Choose the extent of the source plane D, the sampling rate F_s and the stepsize Δz, as described in the linear algorithm. Also choose the number of harmonics to be used during the calculations.

2. Sample the source function spatially, to obtain the samples v_1. Initially, all other harmonics v_n will be zero.

3. Sample the normal velocity point spread function for all harmonics, h_n, and perform the DFT to obtain the samples H_n. Alternatively, sample the analytical Fourier transform H_n directly. For either option, H_n will be the transfer function for a step of length $\Delta z/2$.

4. Perform the DFT of the source function v_n and window it. Multiply the result of each harmonic with its transfer function H_n and then take

the inverse DFT. This will propagate the field a distance $\Delta z/2$, and result in the intermediate v'_n.

5. Add nonlinear effects to v'_n by inserting it into Eq. (5.10).

6. Repeat step 4 for v'_n to propagate one more $\Delta z/2$ step. This is the resultant field v_n in the step Δz.

7. Repeat step 4 trough 6 until the desired propagation distance is obtained.

5.6 Implementation issues

There are still a few problems related to implementing a nonlinear propagation algorithm. These are discussed here before moving on to verification in the next chapter.

Memory usage

One large challenge in implementing nonlinear propagation is the memory usage. A matrix of double precision is needed to hold the velocity field of every harmonic at each step. The size of the matrix is $M \times N \times N$, where $N = D/\Delta d$ and M is the number of harmonics included in the calculations. So, dependent on the choice of sampling scheme, as discussed in Chapter 4, and the number of harmonics included, the size of the matrix needed varies.

Each harmonic has its own propagation function H_n, so a matrix of equal size is needed to hold H. As H is determined by the steplength, H can be calculated once and stored at the beginning of the simulation if all planes are equidistant from one another. It could also be stored on disk and H_n could be read into memory each time it is needed. This would be very time-consuming, but allows for larger matrices to be used.

The size of the matrices determine if they can be held in virtual memory at all. This limits our possible choices of parameters, especially in the 3-D case. It also determines the size of the DFT, which affects computation time to a great deal.

To limit the virtual memory needed in the simulation, in-place calculation is used. At each step Δz, the matrix v contains the velocity field for that step. This field may be stored on disk if needed at some later time.

Low attenuation

For water, the value of b in the attenuation term in Eq. (5.9) is equal to 2. This low value leads to a small attenuation of even the highest harmonics, and in literature, attenuation is often neglected for propagation problems in water. With a small or non-existing damping, more harmonics need to be modeled, and this might lead to problems with both memory and computation time.

Christopher and Parker mention in their article (1991a) that if no shocks are anticipated, five to ten harmonics are adequate to describe a continuous wave field. However, to compute propagation with shocks would require 30 to 50 harmonics. They estimate the size of the nonlinear effects by using the maximum amplitude of the linear field as input to the FDSBE.

To limit the number of harmonics necessary for the field calculation, they propose to artificially ramp up the attenuation. This is done by replacing the exponential coefficient b by $b(n) = b + [(n-1)q/N]$. This version of the attenuation function has been included in the program. It should still allow for accurate modeling because very little energy is contained in the highest harmonics. It is, however, not valid for sinusoidal sources of very high amplitude involving near-field shocks. Setting q equal to zero will lead to $b(n) = b$ for all harmonics.

Phase front curvature

The source has an initial normal velocity that is input to the algorithm. At some subsequent propagation plane, the velocity is then calculated by the proposed algorithm. However, these are actual, not normal, velocities, and have some wave or phase front curvature. To correct for this, Christopher and Parker (1991a) added correction terms to their nonlinear substep by dividing Δz and $v_n(z,i)$ by $\cos\theta[u_1(z,i)]$. Here,

$$\theta[u_1(z,i)] = \frac{\mathrm{d}}{\mathrm{d}r}\left[\arctan\left(\frac{\mathrm{Im}[u_1(z,i)]}{\mathrm{Re}[u_1(z,i)]}\right)\right]_{r=r_i}$$

is the angle the phase front of the fundamental makes with the z-axis at the point (z,i). Their algorithm assumes radial symmetry, so to implement this, r would have to be replaced by x and y. This would lead to a rather challenging derivative. Fjellestad (2000) tried to estimate the derivative by a bilinear interpolation, but found that artificial sources were introduced which needed to be accounted for. He also gained good results by neglecting this correction term, and so it has not been included in the model of this thesis either.

A note on Burgers' equation and the FDSBE

During the work on this thesis, the author came across many versions of the FDSBE in literature. As this was both confusing and time-consuming, the differences between them are discussed here.

The version given by Haran and Cook has already been mentioned. The results seem tolerable at first, but tend to infinity for high initial pressure or for larger propagation distances, as the result is multiplied by 2 for each Δz step.

Christopher and Parker (1991b) gave a version equal to Eq. (5.10) but divided by a factor 2. This version was initially implemented in the nonlinear simulations in Section 6.4, but resulted in too little energy leaking to the higher harmonics compared to measurements. Two theses have previously been concluded on the topic of nonlinear propagation at the University of Oslo by Synnevåg (1998) and Fjellestad (2000), which are frequently referred to in this work. Both implemented the FDSBE given by Christopher and Parker, and in the same simulation obtained the same erroneous results, with lower value of the higher harmonics. This is not due to the velocity not being phase corrected, as correct results were achieved in Chapter 6 by using Eq. (5.10) without phase correcting. As Christopher and Parker also achieved correct results in the same simulation, the extra 2 is assumed to be a typo.

In addition Zemp *et al.* (2003) gave a version of the FDSBE similar to Eq. (5.10), which had the same constant term. But in their version the second summation was equal to

$$\sum_{k=n}^{N} n v'_k v'^{*}_{n-k} \qquad \text{instead of} \qquad \sum_{k=n}^{N} n v'_k v'^{*}_{k-n},$$

with the subscript of the velocity field reversed. This was however not consistent with the FDSBE given in the thesis by Zemp (2000)

$$\begin{aligned} v_n(i_x, i_y, z+\Delta z) &= v'_n(i_x, i_y, z+\Delta z) \\ &+ \frac{jn\beta\pi f \Delta z}{2c_0^2}\left(\sum_{k=1}^{n-1} v'_k v'_{n-k} + 2\sum_{k=n+1}^{M} v'_k v'^{*}_{k+n}\right) \\ &- \alpha_0 (n f_0)^b v'_n \Delta z, \quad n = 1, 2, \ldots, N, \end{aligned}$$

where both summations as well as the constant term were different. However, as k ranges to M, the subscript $k+n$ of v' will range to $M+N$, which exceeds

the maximum dimensions of the matrix v'. This plus sign might just be a typo.

All the different versions were tested in the algorithm, but Eq. (5.10) undeniably gave the best results, and is regarded as the correct implementation of the FDSBE in this thesis.

Chapter 6

Verification

Before we may trust the implemented algorithm to produce correct results, it must be verified. This will be done in the following chapter by testing it on various examples from literature. The linear algorithm is tested in Sections 6.1 and 6.2, and on circular sources in Section 6.3. The nonlinear algorithm is tested in Section 6.4 and finally the choice of step length is discussed in Section 6.5.

6.1 Verification of the linear propagator

To verify the linear algorithm, it is tested on several examples used by Wu *et al.* As in one of their articles (1996a), we consider a linear transducer of width $2A = 32\lambda$ operating in water with density $\rho = 10^3$ kg/m^3. The sound speed is $c = 1500$ m/s. Throughout all of the referred article, the sampling frequency is chosen to be $Fs = 2/\lambda$ and $N = 8192$. This gives a discretization size $D = 4096\lambda$, which is chosen so large to minimize the spatial aliasing error. The main consideration in this chapter is to see if the simulator produces correct results, and the impact of different parameters will therefore not be discussed here.

The angular spectra achieved by means of the discrete Fourier transform (DFT) and the discrete sinc-Fourier transform (DSFT) are presented in Figs. 6.1(a) and 6.1(b), respectively. Note that the DFT version has been phase corrected, as $L = 64$ and thereby even. The difference between these two spectra will then be dominated by the frequency aliasing. It is displayed in Fig. 6.1(c). Here we can clearly see that the DFT's results deviates more as n_x grows, implying larger propagation angles. Fig. 6.1 is indistinguishable from Fig. 2 in the article by Wu *et al.*

Utilizing the DFT's and DSFT's spectra, the pressure field for z ranging

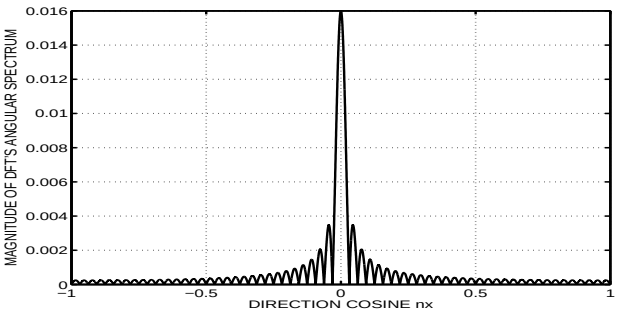

(a) Magnitude of DFT's angular spectrum.

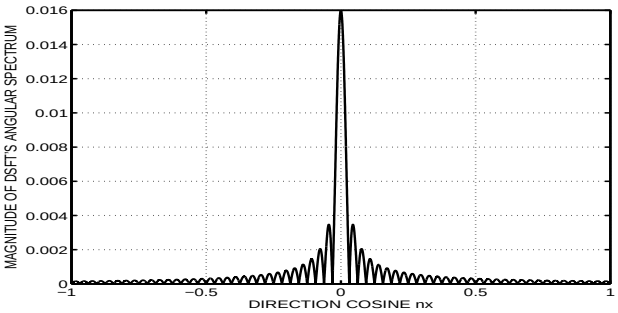

(b) Magnitude of the DSFT's exact spectrum.

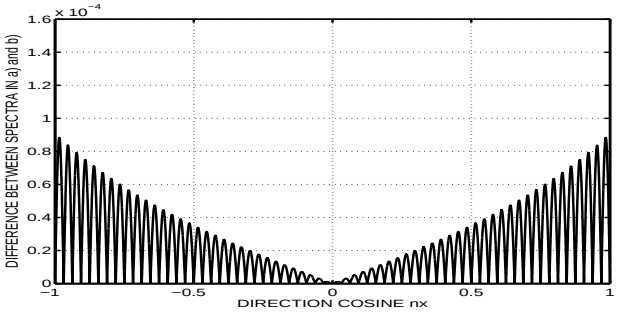

(c) Difference of the spectra given in (a) and (b).
Note that the vertical axis is blown up by 100.

Fig. 6.1: The DFT angular spectrum compared with the exact spectrum obtained by using the DSFT, for the transducer with $2A = 32\lambda$. $N = 8192$, $F_s = 2/\lambda$.

from 2λ to 400λ is calculated and presented in Figs. 6.2 and 6.3, respectively. The field is calculated both on the z-axis, giving $x = 0$, and off-axis, at $x = 2A$. Fig. 6.2 is practically identical to the dotted curves in Fig. 3 in the referred article, showing the DFT results. Wu *et al.* also implemented the analytical results (showed with solid lines in the same plots) and the DFT result deviates from this one in the near field. There is also a small ripple in the far field, reproduced with our algorithm in Fig. 6.2(a). This ripple is the remains of the spatial aliasing.

The DSFT-based spectrum gives a better result both on and off the z-axis, as is shown in Fig. 6.3. Again our algorithm completely reproduces the results presented by Wu *et al.*, wherein the agreement between the DSFT's results and the analytical one is excellent. All that remains is some minor ripple in the far field, but this is slightly diminished compared to the DFT's results.

Other parameters

In search for an optimal choice of parameters, Wu *et al.* (1996b) tested a variety of options for the 2-D case. An important test of our algorithm is to reproduce Fig. 3 in their article, which shows the calculated fields from the linear transducer for a selection of parameters. They also showed the analytical solution with solid lines in the same plots.

The predicted results from our model are shown in Fig. 6.4. All plots are in excellent agreement with the corresponding dotted curves in the article by Wu *et al.* These results demonstrate not only the credibility of our model, but also the importance of choosing parameters wisely. The influence of different parameters on the results were discussed in Chapter 4.

Note that in all of the figures above, the incremental step Δz between planes is 2λ, which gives 200 planes out to the maximum lateral distance of 400λ.

Linear plots in three dimensions

All plots given so far were produced by means of the two-dimensional linear algorithm. Wu *et al.* also implemented a three-dimensional version (1997b), and their results will now be used to verify the three-dimensional algorithm implemented in this thesis. The source is a rectangular one, of width $2A = 32\lambda$ and height $2B = 24\lambda$. In this simulation, $Fs = 2/\lambda$ and $N = 512$, which is an optimal selection of parameters for this simulation, in the region of interest.

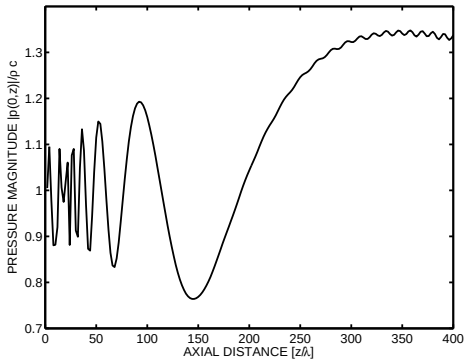

(a) On the z-axis; $x = 0$.

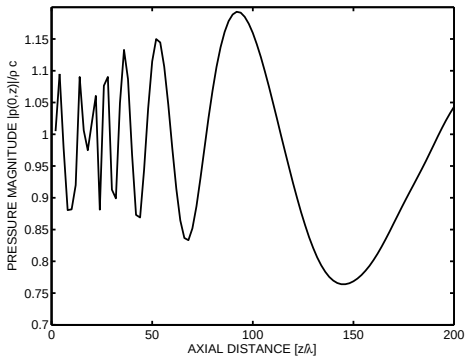

(b) The zooming in of (a).

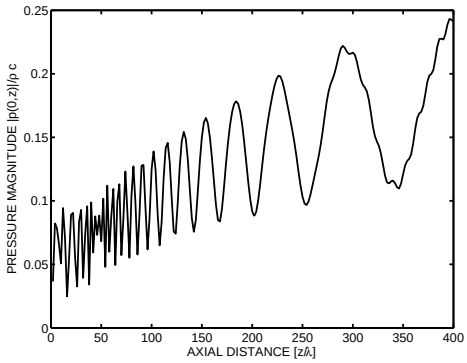

(c) Off the z-axis, at $x = 2A$.

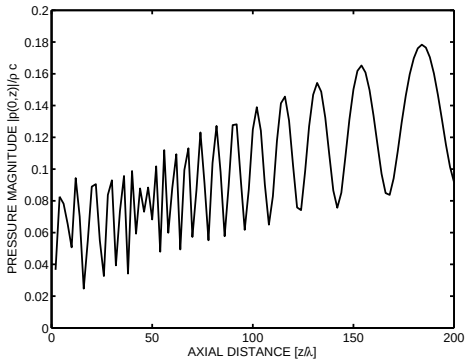

(d) The zooming in of (c).

Fig. 6.2: Results obtained by using the DFT-spectra for $N = 8192$, $Fs = 2/\lambda$. Normalized pressure field $|P(x, z)|/\rho c$ for the transducer of width $2A = 32\lambda$.

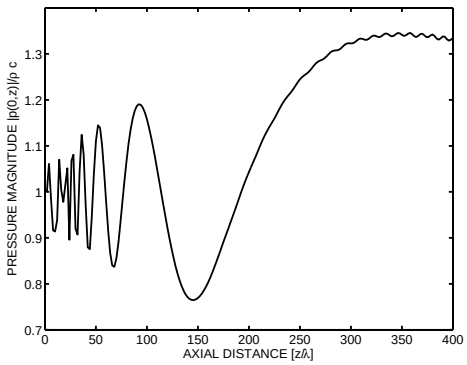

(a) On the z-axis; $x = 0$.

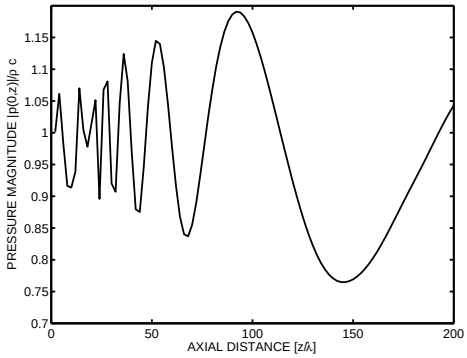

(b) The zooming in of (a).

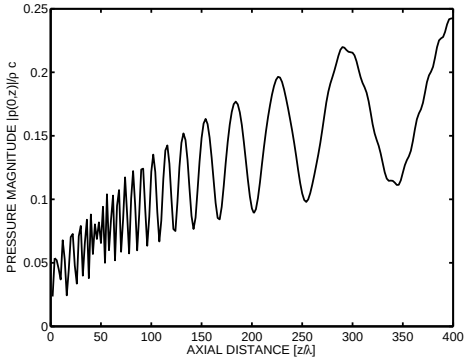

(c) Off the z-axis, at $x = 2A$.

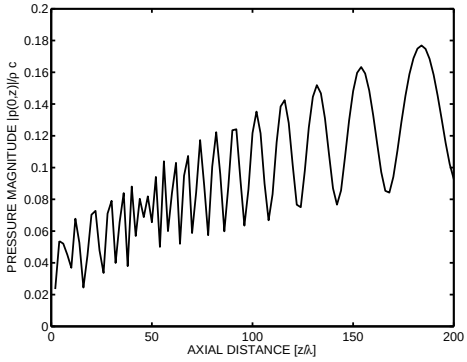

(d) The zooming in of (c).

Fig. 6.3: Results obtained by using the DSFT-spectra for $N = 8192$, $Fs = 2/\lambda$. Normalized pressure field $|P(x, z)|/\rho c$ for the transducer of width $2A = 32\lambda$. (Figs. (b) and (d) are not given by Wu *et al.*)

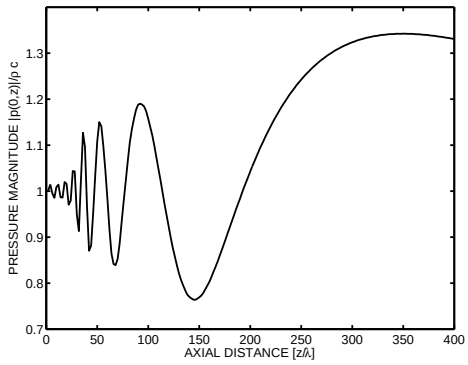

(a) $N = 512$, $Fs = 1/\lambda$.

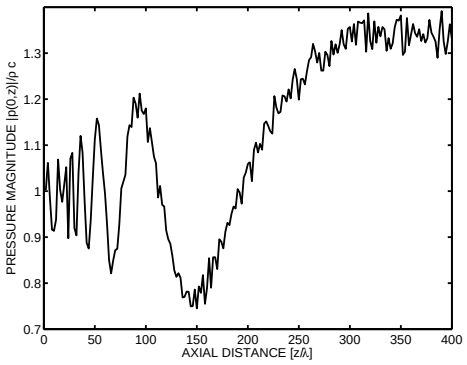

(b) $N = 1024$, $Fs = 2/\lambda$.

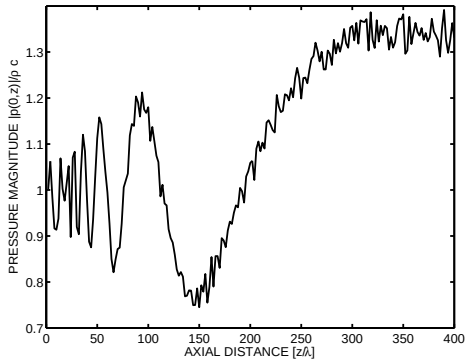

(c) $N = 512$, $Fs = 2/\lambda$.

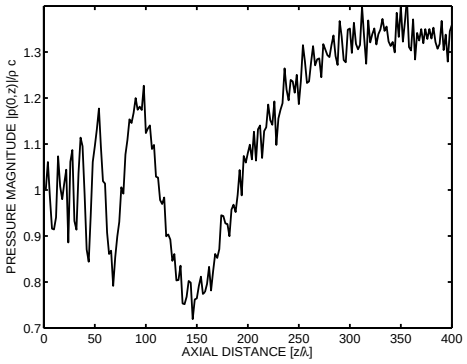

(d) $N = 1024$, $Fs = 3/\lambda$.

Fig. 6.4: The ASA's pressure magnitude, calculated on the z-axis for the transducer of width $2A = 32\lambda$ for various choices of N and sampling frequency F_s.

Fig. 6.5 shows the result from our implementation, which does not deviate from Wu *et al.*'s results in their Fig. 5. The ASA's solution is in this case in very good agreement with the analytical solution, also implemented by Wu *et al.* and shown in their figure.

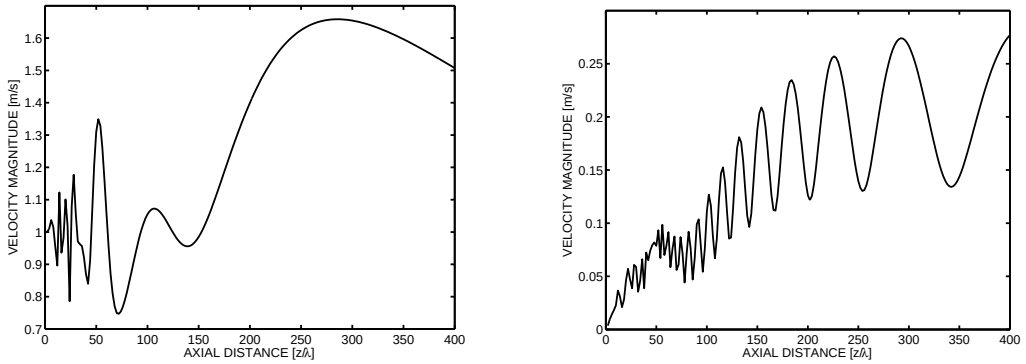

(a) $x/A = 0$ and $y/B = 0$ (b) $x/A = 2$ and $y/B = 0$

Fig. 6.5: Acoustic field from the transducer of width $2A = 32\lambda$ and height $2B = 24\lambda$, as calculated by the 3-D algorithm.

6.2 The multistep algorithm

In Chapter 4, the idea of the multistep algorithm was introduced as a replacement for the single-step version when nonlinearity is to be implemented. Some difference might be expected between the two methods, as the DSFT is only applicable in the first step of the multistep algorithm. In all other steps, the DFT must be used to calculate the angular spectrum of the result from the previous step. On the z-axis, however, the difference between the two spectra is close to zero, as previously demonstrated in Fig. 6.1(c). Hence, the field on or close to the z-axis should not be affected much by our switching to multistep propagation. This has been verified by running the multistep version with the same parameters as above, for the same transducer.

As a demonstration, the velocity field from the linear transducer for $N = 512$, $F_s = 1/\lambda$ is propagated out to the distance $z = 1024\lambda$, which is the near field/far field crossover for this particular source. In this case, Δz is set equal to λ to have more points of comparison.

Fig. 6.6(a) depicts an overlay of the onaxis velocity field results for both

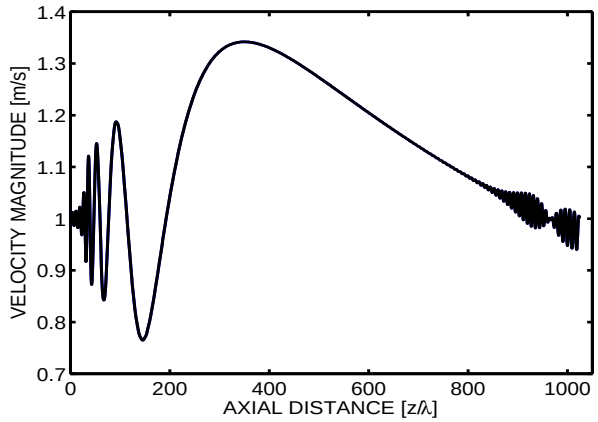

(a) Velocity field on the z-axis. Overlay of the multistep and the single-step algorithm's computed results. Note how the spatial aliasing comes into play at about 800λ.

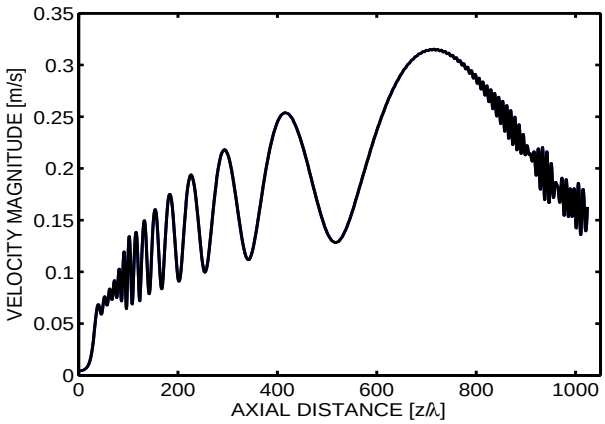

(b) Field off-axis, at $x = 2A$. Overlay of the multistep and the single-step algorithm's computed results. Spatial aliasing is more severe in off-axis positions.

Fig. 6.6: To investigate the error in the multistep algorithm, the velocity field for the linear transducer is propagated to the near field/far field limit, $z = 1024\lambda$. In this simulation, $N = 512$ and $Fs = 1/\lambda$. (These plots are not given by Wu *et al.*)

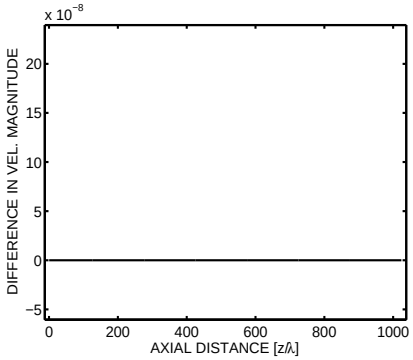

Fig. 6.7: Difference in velocity magnitude on the z-axis between the multistep and the single-step method. Maximum difference was $1.8 \cdot 10^{-13}$ m/s.

the multistep and the single-step version. Note how the spatial aliasing comes into play at about 800 λ, pushed towards the far field by choosing optimal parameters for this simulation. The curves are as good as indistinguishable. The difference between the two is practically zero, as shown in Fig. 6.7. The maximum error was found at 886 λ where it was equal to $1.8 \cdot 10^{-13}$ m/s.

The computed velocity field at $x = 2A$ is shown in Fig. 6.6(b). The error offaxis (not shown) has a maximum of $2.4 \cdot 10^{-13}$ m/s. For the multistep algorithm, the accuracy of the result is based on how correct the field was calculated in the previous step. This is not the case for the single-step algorithm, and so we might expect the error to accumulate as the propagation distance grows. The small values of Fig. 6.7 makes this hard to see.

If the pressure field is of interest, the impedance relation $p = \rho c v$ may be used. For this medium, this blows up the error by a factor 10^6, but its size relative to the field stays the same. This makes the error easier to analyze when expressed in pascals. The difference in pressure magnitude at $x = 0$ and $x = 2A$ is displayed in Figs. 6.8(a) and 6.8(b), respectively. The error is clearly accumulative, and larger offaxis than onaxis (maximum $3.6 \cdot 10^{-7}$ Pa and $2.7 \cdot 10^{-7}$ Pa, respectively).

As the error accumulates at each step, the field was recalculated with a steplength equal to 4λ to see if this made the error grow slower. The difference in pressure magnitude for this simulation is shown in Fig. 6.9. It does appear smaller than for $\Delta z = \lambda$, and the maximum error is now $1.9 \cdot 10^{-7}$ Pa onaxis and $2.6 \cdot 10^{-7}$ Pa offaxis. The number of steps should therefore be reduced if possible, when the propagation distances are large.

A common way to implement the ASA is to calculate diffraction of the pressure field, instead of the velocity field. As a test, the pressure field was also computed directly, but this gave the same results.

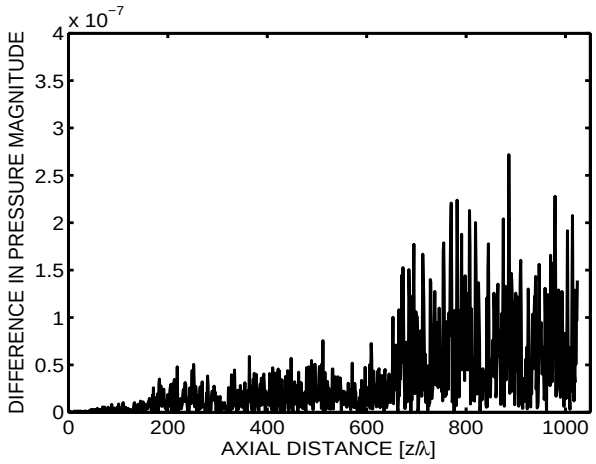

(a) Difference in pressure magnitude on the z-axis.

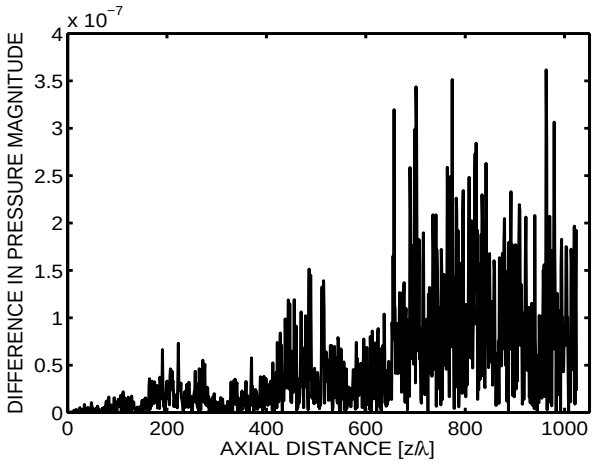

(b) Difference in pressure magnitude at $x = 2A$.

Fig. 6.8: Difference in pressure magnitude when using multistep as opposed to single-step (inserting z's directly). Stepsize $\Delta z = \lambda$.

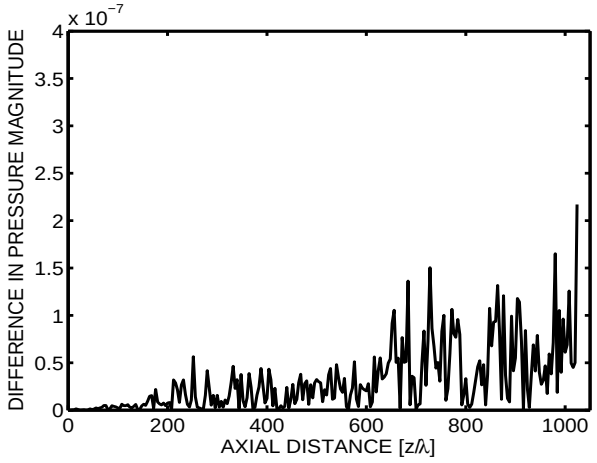

(a) Difference in pressure magnitude on the z-axis.

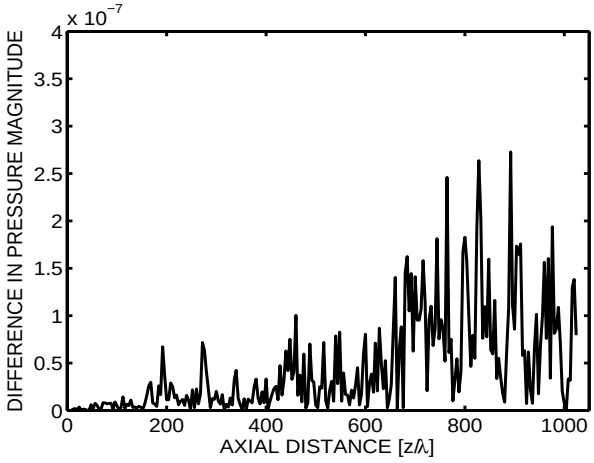

(b) Difference in pressure magnitude at $x = 2A$.

Fig. 6.9: Difference in pressure magnitude when using a steplength Δz equal to 4λ.

As the error is a factor 10^{-13} smaller than the field, the multistep algorithm is assumed to produce satisfying results. It is therefore used to calculate the field from here on out.

6.3 Application to circular sources

The algorithm is also applicable to circular sources, which will be demonstrated next. We consider an example given by Christopher and Parker (1991b) in which a 3-MHz unfocused piston of radius 1 cm is operating in water. Attenuation is in this case neglected.

The sampling rate is given to be 80 samples per centimeter. This implies that $\Delta d = 0.25\lambda$ or, equivalently, $F_s = 4/\lambda$. The transform extent, which is half our source plane, is given to be 4 cm. Hence we end up with the number of lateral samples N equal to 640.

The initial acoustic peak intensity is 0.1 W/cm^2. To convert to initial normal velocity as required by the algorithm, the following version of the impedance relation was used (Young and Freedman 2004)

$$v_0 = \sqrt{\frac{I}{\rho \cdot c}} = \sqrt{\frac{0.1 \frac{\mathrm{W}}{\mathrm{cm}^2} \cdot 10^4}{10^3 \frac{kg}{m^3} \cdot 1500 \frac{m}{s}}} \quad ,$$

which gives the initial uniform amplitude of approximately 0.026 m/s.

First, the field is propagated out to $z = 0.5$ mm. The result is depicted in Fig. 6.10(a). There is a slight disturbance at lateral distances greater than a centimeter, not present in Christopher and Parker's result. Their algorithm is valid for circular sources only, and takes advantage of circular symmetry in using the discrete Hankel transform (DHT). There are differences between the DHT and the DFT which Fjellestad discussed for this case in his thesis (Fjellestad 2000). He showed that the DFT's deviation from the DHT is especially evident for spatial frequencies of 10 cycles per centimeter or greater. This might explain the disturbance in our results. Furthermore, our source is discretized on a rectangular grid and will never be completely circular, although a denser sampling scheme will help.

The field calculated at $z = 200$ mm is shown in Fig. 6.10(b). The only difference from Christopher and Parker's result is the zero amplitude at lateral distances greater than about three centimeters. This is due to our window tapering.

As a second example of application to circular sources, we consider a case in the thesis by Zemp (2000). This transducer has a radius A of 1.9 cm and operates at 1 MHz. The initial pressure is 50 kPa, and the field is

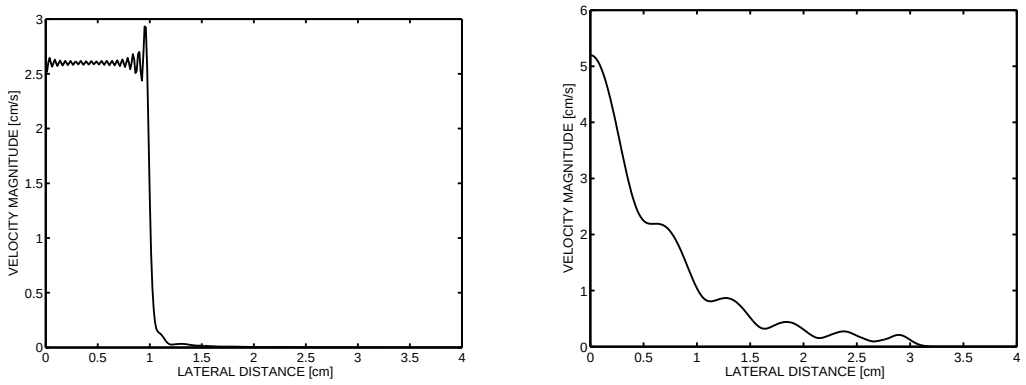

(a) $z = 0.5$ mm (b) $z = 200$ mm

Fig. 6.10: Velocity field from an unfocused circular piston transducer of radius 1 cm. The lateral field is circular symmetric, and shown along the positive x-axis.

propagated out to the near field/far field crossover, A^2/λ, or 0.25 m. The result is presented in Fig. 6.11, and is in excellent agreement with what Zemp obtained.

All the plots given so far have been in very good agreement with their correspondents in literature, and we may conclude that the linear algorithm produces satisfying results for both linear, rectangular and circular sources.

6.4 Verification of the nonlinear substep

To verify the nonlinear algorithm, it is tested on the case of a plane circular piston source with frequency 2.25 MHz and initial pressure amplitude 100 kPa. The source has a radius of 19 mm, and the field is propagated 750 mm in the axial direction. The example is from an article by Baker *et al.* (Baker, Anastasiadis, and Humphrey 1988), who performed measurements in a water tank as well as performing simulations. To produce the predicted results, the parabolic approximation model was used. As mentioned in the previous chapter, this is not valid in the near field, and we would expect some differences there, compared to our results.

Christopher and Parker implemented the same problem using the angular spectrum approach combined with the FDSBE (Eq. (5.9)). The same approach has been used in this thesis, with the exception that the second-order operator splitting technique is implemented. This was described in

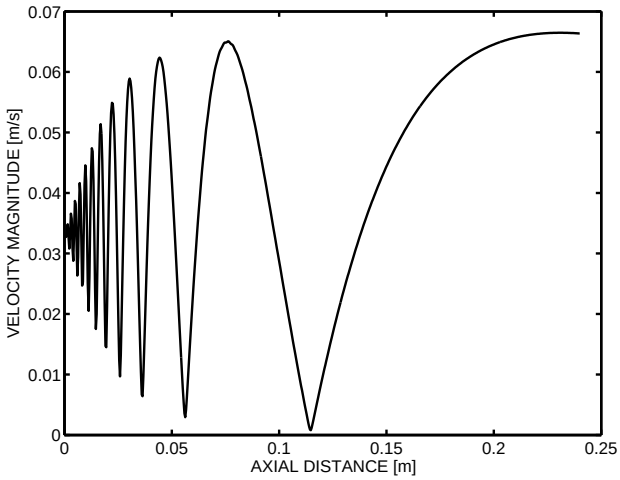

Fig. 6.11: Velocity profile of the plane piston transducer of radius 1.9 cm with initial pressure 50 kPa. $N = 512$, $F_s = 2/\lambda$.

Chapter 5.

The measured amplitudes of Baker *et al.* for the first three harmonics are shown in Fig. 6.12(a). The corresponding predictions using our model are presented in Fig. 6.12(b), where the velocity amplitudes have been converted to pressure amplitudes using the impedance relation $p = \rho c \mathbf{v}$. The results are in good agreement with the measurements Baker *et al.* obtained. There are some differences in the near field, before 100λ, where the measurements of Baker *et al.* show diffraction loss. They mention that this is a limitation of the hydrophone used to measure the field. Close to the transducer, the pressure as seen by the hydrophone tends towards the average. This is because the field contains rapid variations which are smaller than the hydrophone diameter. The predictions of our model do however correspond very well to what Christopher and Parker obtained.

We see that the last maximum of the fundamental is lower than the previous maximum at 200 mm. This clearly demonstrates the transfer of energy from the fundamental into higher harmonics, whose levels grow during the same period. At the maximum axial distance of 750 mm, the levels of the higher harmonics are relatively high compared to the fundamental. Recalling the discussion in Chapter 5, this would indicate that the waveform is seriously distorted compared to the transmitted wave.

Baker *et al.*'s log scaled measured and predicted amplitudes of the second and third harmonics are shown in Figs. 6.13(a) and 6.13(b), respectively. Note the deviations in the near field, which demonstrates the limitations of the parabolic approximation. Figs. 6.13(c) and 6.13(d) depict the

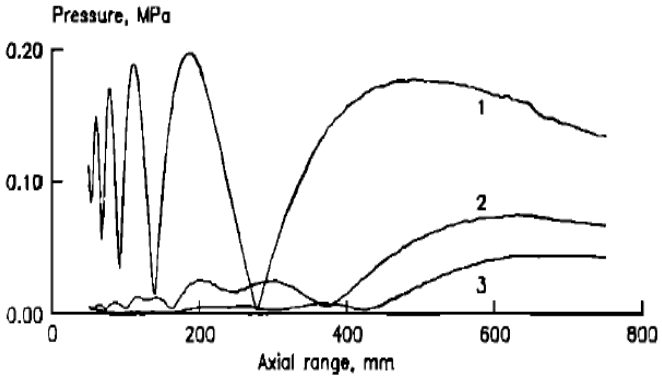

(a) The measured amplitudes of the first three harmonics. (Ill: Baker *et al.* (1988))

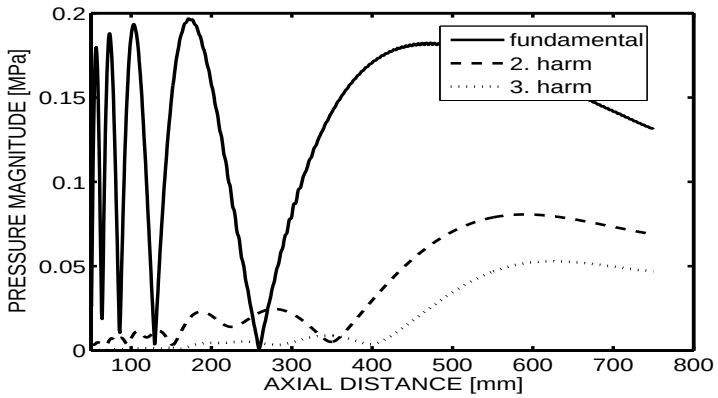

(b) Computed axial amplitudes for the first three harmonics, shown for $z > 50\lambda$.

Fig. 6.12: Comparison of the predicted results for an unfocused 2.25 MHz transducer with the measured values of Baker *et al.*.

corresponding results of our model. The ASA's solution is in much better agreement with the measured results in the near field. Some differences still remain in the nodal depths compared to the measured values of the second harmonic. This is believed to be because of the previously mentioned diffraction loss. Christopher and Parker also got this discrepancy.

Finally, the log scaled lateral field profile at $z = 275$ mm is displayed for the first three harmonics in Fig. 6.14. This propagation distance corresponds to the last axial minimum of the fundamental. This figure shows that the higher harmonics have narrower field profiles than the fundamental. The computed results of our model shown in Fig. 6.14(b) are identical to the computed results of Baker *et al.*, except for the values of the fundamental far off the z-axis. The parabolic approximation might not be valid in this region. Also, the fundamental center value is not exactly zero. Again our results are equal to those obtained by Christopher and Parker.

Parameter	**Symbol**	**Value**
Fundamental frequency	f0	2.25 MHz
Density	ρ	1000 kg/m^3
Sound speed	c	1500 m/s
Harmonics used in simulation	M	10
Lateral samples	N	512
Sampling frequency	Fs	$1/\lambda$
Radius	A	0.0345 m
Nonlinear coefficient	β	3.5

Table 6.1: Parameters used in the simulation of this section.

6.5 Test of different stepsizes Δz

Figs. 6.12 through 6.14 were produced with a step length Δz equal to λ. Though Christopher and Parker make no mention of the step length used in their simulation, they claim that a Δz small enough to display axial variations of the fundamental is acceptable. This is valid if the initial amplitude is not excessively high. Otherwise, the attenuation for the highest harmonic should be no smaller than 0.7 across Δz, and this would determine the appropriate stepsize in the far-field region.

In their companion linear article (1991b), they perform a simulation in a layered medium using 600 Δz's out to an axial distance of 12 cm. The frequency of the source was 3 MHz, giving a step size of about 0.4λ. The simulation was repeated with the nonlinear algorithm, presumably with the

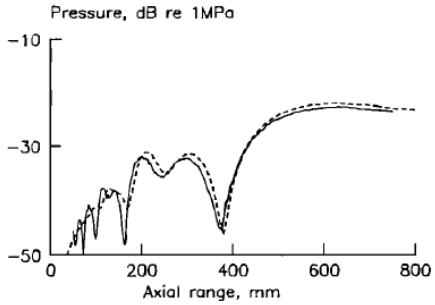

(a) The measured and computed (dotted lines) second harmonic, as obtained by Baker *et al.*(Ill: Baker *et al.* (1988))

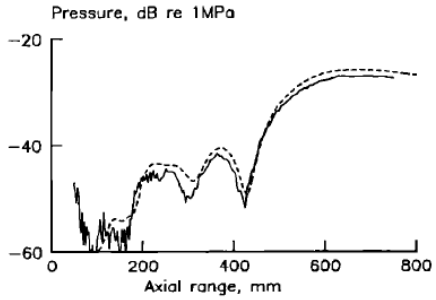

(b) The measured and computed (dotted lines) third harmonic, as obtained by Baker *et al.*(Ill: Baker *et al.* (1988))

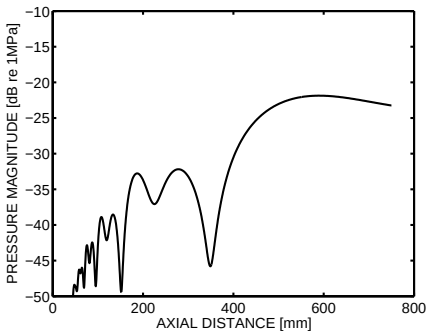

(c) Predicted results for the second harmonic.

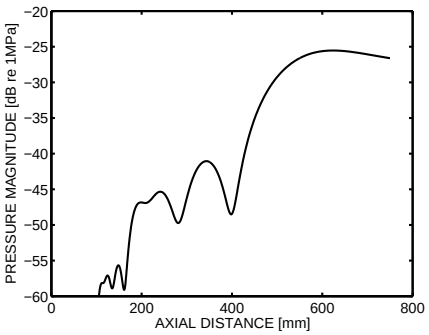

(d) Predicted results for the third harmonic.

Fig. 6.13: Log scaled axial amplitudes of the second and third harmonics. Comparison of the results obtained by Baker *et al.* and our model. Note the difference in the near field between the two computed results.

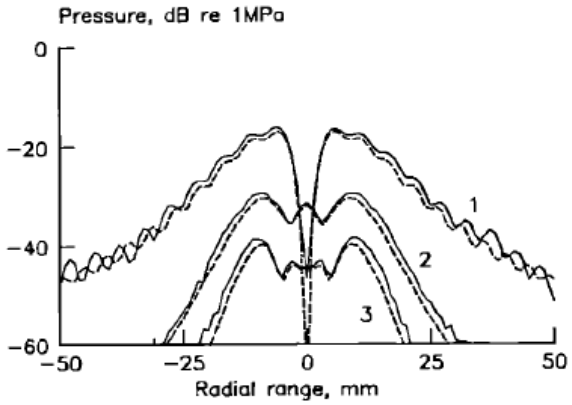

(a) Baker *et al.*'s computed (dotted lines) and measured results. (Ill: Baker *et al.* (1988))

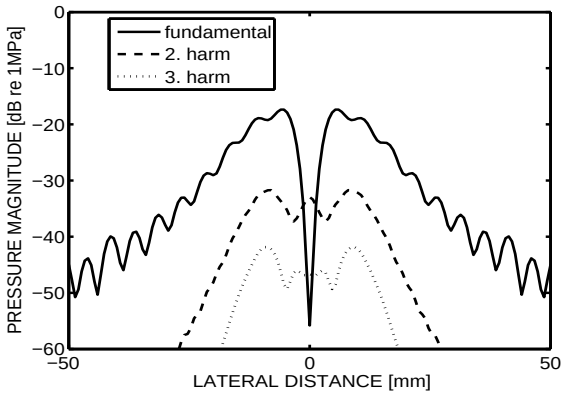

(b) Corresponding computed results of our model.

Fig. 6.14: Log scaled lateral amplitudes of the first three harmonics. Axial distance is 275 mm, corresponding to the last axial minimum.

same stepsize. In the same article, they investigated a 3 MHz circular source operating in water, using the single-step approach. They gained good results for the FSC algorithm when Δz was equal to λ, but convolution wraparound error was severe for $\Delta z = 20$ cm $= 400\lambda$.

To reduce computation time, we would like to enlarge the stepsize and still obtain good results. Implementing the second order operator-splitting approach as described in Section 5.5 might allow this. However, large stepsizes might make H undersampled in the frequency domain, as stated by Zemp *et al.* (2003) and discussed in Section 4.4. To see how the stepsize affects the results, the field for the lateral distance of 750 mm was recalculated with a consecutive doubling of the stepsize. As shown in Figs. 6.15 and 6.16, the results are still very good. Even with a stepsize of 32λ, correct results in the grid points are obtained, although the axial variations may not be displayed very well on such a coarse grid. Judging from the log scaled plots in Fig. 6.16, Δz equal to 8 λ gives very good results, and such a grid still displays the axial variations quite well.

The results obtained by the algorithm are generally in good agreement with measurements and simulated results reported in literature. The nonlinear algorithm based on the ASA may in some cases give better results than the parabolic approximation, and we may conclude that the simulator produces correct results for the propagation distances considered so far. In Chapter 7, the simulator's performance on larger distances will be examined. The simulator will also be utilized to investigate the nonlinear field of a 200KHz circular transducer.

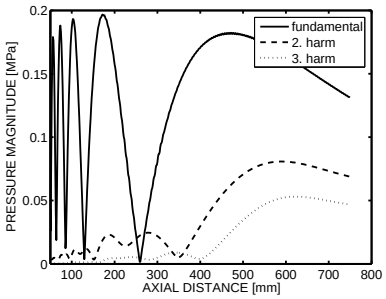

(a) Axial field, $\Delta z = 2\lambda$

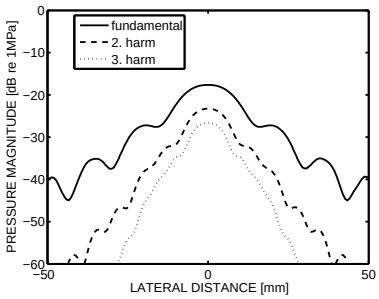

(b) Lateral field at 750 mm, $\Delta z = 2\lambda$

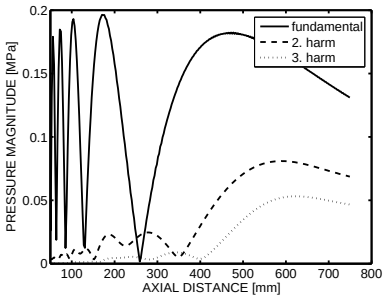

(c) Axial field, $\Delta z = 4\lambda$

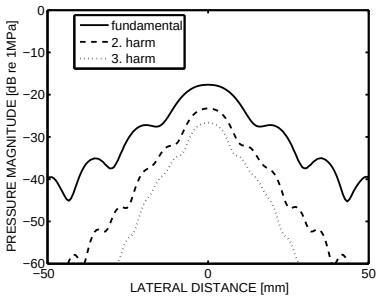

(d) Lateral field at 750 mm, $\Delta z = 4\lambda$

Fig. 6.15: The field of the transducer used by Baker *et al.* for the axial distance of 275 mm, calculated using different stepsizes Δz.

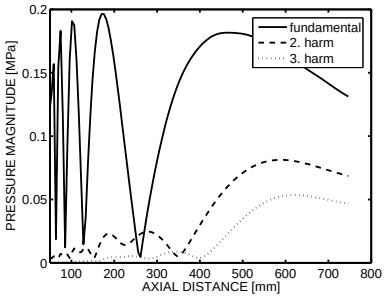

(e) Axial field, $\Delta z = 8\lambda$

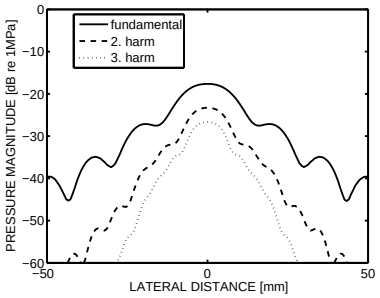

(f) Lateral field at 750 mm, $\Delta z = 8\lambda$

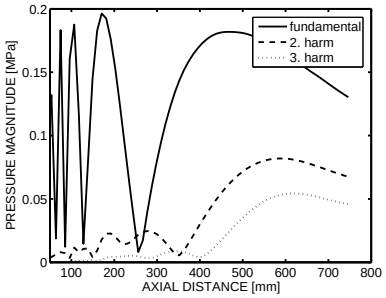

(g) Axial field, $\Delta z = 16\lambda$

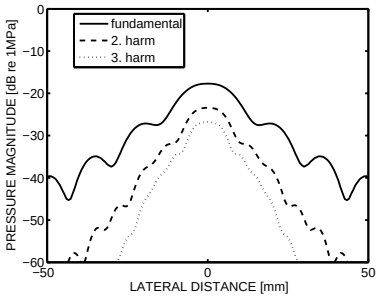

(h) Lateral field at 750 mm, $\Delta z = 16\lambda$

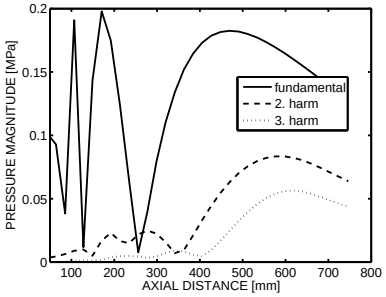

(i) Axial field, $\Delta z = 32\lambda$

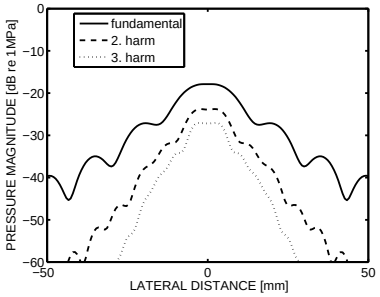

(j) Lateral field at 750 mm, $\Delta z = 32\lambda$

Fig. 6.15: The field of the transducer used by Baker *et al.* for the axial distance of 275 mm, calculated using different stepsizes Δz. (Cont.)

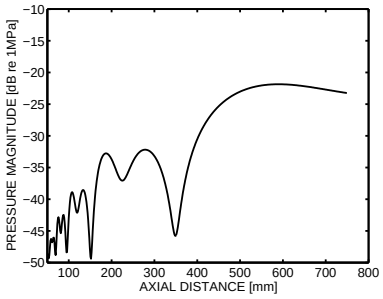

(a) $\Delta z = 2\lambda$

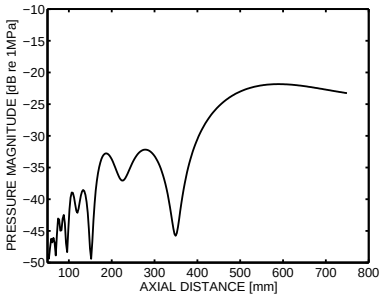

(b) $\Delta z = 4\lambda$

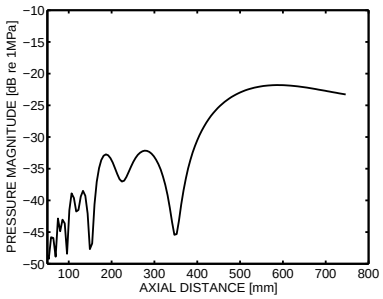

(c) $\Delta z = 8\lambda$

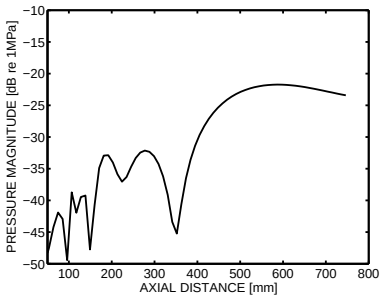

(d) $\Delta z = 16\lambda$

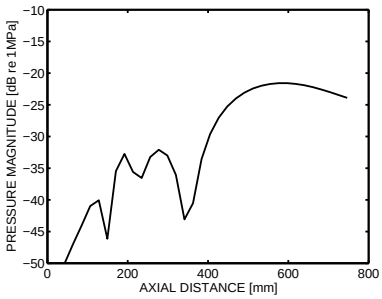

(e) $\Delta z = 32\lambda$

Fig. 6.16: The log scaled field of the second harmonic, calculated using different stepsizes Δz.

Chapter 7

Simulations and discussion

As new acoustic equipment is expensive to develop, a simulator which calculates the nonlinear field correctly for large distances would be of great value to fishery researchers and others dependent on wide-range sonars. The simulator must work for a wide variety of sources and initial states to be of much use.

An attempt on such a simulator has been developed in this thesis. In this chapter, it will be used to calculate the field of a transducer used in fisheries research.

Some issues regarding the simulation of large propagation distances is discussed first in Section 7.1. We will revisit a familiar source to determine what parameters to use in the main simulations. Section 7.2 resumes the topic of target strength, and explains how nonlinear effects may influence these measurements. This offers a motivation for the main simulations in Section 7.3, where the size of the nonlinear effects are investigated for an appropriate source. The field of the second harmonic is also investigated.

7.1 Calculating the far field

The field from a variety of transducers was calculated in Chapter 6. In the current section, we will reconsider the source used by Baker *et al.* (1988) in their calculations, the 2.25 MHz circular transducer. The computed field for this transducer was presented in Section 6.4. Attenuation was neglected, as was also done by Christopher and Parker in their simulation of the same problem (1991a), and the simulator gave excellent results out to the axial distance of 750 mm.

The main consideration in this thesis are transducers used in fisheries acoustics. Needless to say, the axial ranges of interest of such applications go

far beyond the distance of 750 mm. Fish swim at a wide range of depths, and finding them at several hundred meters is not uncommon. One might also want to use sonars to find fish at large horizontal distances. It is therefore of great interest to see how the simulator copes with larger propagation distances. The reports of such simulations in literature are few, because the emphasis of nonlinear simulations has been on problems involving medical ultrasound or sonar fields of short ranges.

To the author's knowledge, the field of the transducer described in Section 6.4 has not yet been simulated further than 750 mm. At this point, we would like to investigate this field to see how well it may be simulated by the program. The interest also lies on how different parameters influence the results. To this end, the field is simulated thrice as far, out to 2.25 meters.

There are several issues to consider in such calculations. What initially springs to mind are the number of harmonics included in the simulation, which was set to ten in all the simulations so far. Christopher and Parker state that five to ten harmonics are adequate if no shocks are likely to occur, otherwise 30 to 50 harmonics might be necessary to simulate the field. Recall from the discussion of Fig. 6.12(b) that a highly distorted waveform is expected at 750 mm. This indicates that ten harmonics might not be adequate for larger propagation distances. For this reason, the field was simulated with 30 harmonics included.

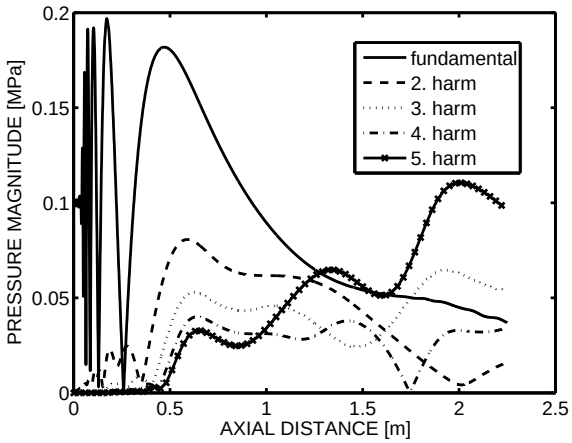

Fig. 7.1: Axial field of the 2.25 MHz circular transducer, simulated out to 2.25 meters without attenuation. $F_s = 1$, $N = 512$.

From Fig. 7.1, it is readily evident that the result does not make physical sense; The higher harmonics actually start growing after reaching their maximum at about 0.6 meters, and finally reach beyond the level of the

fundamental. As nothing but the source is feeding the system with energy, it is unreasonable that the higher harmonics should contain more energy than the fundamental. Obviously, attenuation cannot be neglected for these propagation distances. The simulation is repeated for several step-sizes with attenuation included, with the attenuation coefficient α_0 equal to $25 \cdot 10^{-15}$ Np/m/Hz^2.

The exponential attenuation constant b was initially set to 1.1. This is incorrect, as $b = 1.1$ is a typical value for tissue-like media. For water, b is actually equal to 2. What became clear after several erroneous simulations of this field, setting the correct value of b is very important. The low attenuation in water combined with this incorrect b led to a field that tended to infinity for large steps. The result from some of these simulations is given in Figs. D.3 through D.6 in Appendix D.

An interesting point is that attenuation is negligible up to the propagation distance of 750 mm. This was seen in Section 6.4, where corrects values were obtained even though attenuation was not included in the simulations. Therefore, the effect of an incorrect value of b is not visible at all unless larger propagation distances are considered.

The field was calculated again using the correct value $b = 2$ and a step-length of 8 λ. Christopher and Parker mention that if attenuation is small, an upramping of the attenuation might be necessary, in addition to involving many harmonics. This implies setting a nonzero upramping constant q. (The effect of a nonzero q on the attenuation was described in Section 5.6.) Christopher and Parker found it necessary to use $q = 0.35$ for a similar propagation problem in water in their article (1991a). Therefore, q was set equal to 0.35 in the following simulations.

Fig. 7.2 displays the result. In this simulation, F_s was set to 1, and N to 512. This result is much more reliable than that of Fig. 7.1, as the values of the harmonics decrease with increasing distance after reaching their maximum. This is consistent with the $1/r$-factor in the spherically symmetric solution of the wave equation (Eq. (2.9)). In the lateral field profile at 2.25 meters, displayed in Fig. 7.2(b), some minor ripple due to spatial aliasing is visible in lateral distances greater than 60 mm. With sonars, we are mainly interested in the on-axis field, so this may not be of great importance.

To see how the sampling frequency influenced the result, the simulation was repeated for $F_S = 2/\lambda$ and $F_S = 4/\lambda$ without changing N. As $D = N\Delta d = N/F_s$, this decreases the size D of the zero-padded source plane. From the discussion in Section 4.4, we know that this could lead to spatial aliasing of the field.

The axial and lateral fields computed with $F_s = 2$ and $N = 512$ are shown in Fig. 7.3(a) and (b), respectively. The spatial aliasing is evident in

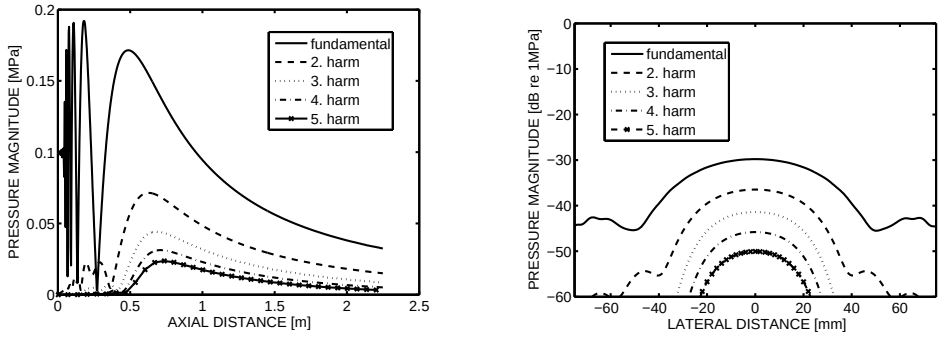

(a) Axial field

(b) Lateral field at 2.25 m

Fig. 7.2: Field from the 2.25 MHz circular transducer, computed with attenuation. $Fs = 1$, $N = 512$.

the first two harmonics for axial distances greater than about 1 meter. The lateral field is cut off at around 60 mm due to the decreased D. To view the whole lateral field, N would have to be enlarged. The aliasing is also visible in Fig. 7.4(a), which displays the field of the fundamental in the xz-plane.

Spatial aliasing occurs at smaller axial distances for $F_s = 4$, whose axial and lateral fields are displayed in Figs. 7.3(c) and (d), respectively. The aliasing seriously distorts the result in this case. To use this sampling frequency, N would have to be a lot larger. The size of D has now gotten so small that the lateral field is cut off at about 30 mm. Figs. 7.4(c) and (d) show the field of the first two harmonics in the xz-plane. The spatial aliasing and the diminished field are especially evident in these figures.

The best results were obtained when setting $F_s = 2/\lambda$ and $N = 1536$. The axial and lateral fields are shown in Fig. 7.3(e) and (f), respectively. With this value of F_S, the angular range spans the entire half-space, and hence includes all real wavenumbers. Apparently N is sufficiently large, because no spatial aliasing is noticeable in this case. The corresponding fields in the xz-plane are shown in Figs. 7.4(e) and (f). They display a clear and credible structure.

A potential cause of problems in nonlinear simulations is the undersampling of higher harmonics. As the spatial sampling interval Δd is fixed for a fixed F_s, the second harmonic will have twice as many oscillations in one interval as the fundamental. If the spatial sampling frequency F_s is set according to the rules that are valid for the fundamental frequency, it may be too low when the frequency is doubled, tripled and so on. So the higher

harmonics may be aliased even if the fundamental is not.

For some reason, no spatial aliasing is not visible in the higher harmonics in Fig. 7.2, even though the fundamental is not completely well-sampled for $F_s = 1/\lambda$. Christopher and Parker do however claim (1991a, pp. 492, second column) to obtain good results with a radial sampling rate of one to two times the Nyquist rate for unfocused fields.

In Section 7.3, the field from a 200 kHz circular transducer was simulated several times with $F_s = 1/\lambda$. In some of the results, (e.g. Fig. 7.16) the effect of the undersampling is visible for the fourth and fifth harmonic. A likely reason for why the aliasing is avoided in Fig. 7.2, is the 57 λ diameter of the 2.25 MHz circular transducer. This makes it a lot larger measured in wavelengths than the source used in Section 7.3, whose diameter is 9.2 λ. This might cause the beam of the higher harmonics to be too narrow for the aliasing to have an effect. Additional simulations could be run to determine if this is the case, but for the time being we may conclude that the fundamental should well-sampled to avoid aliasing in the higher harmonics. In some cases, oversampling the fundamental might be necessary, which makes a larger N a requisite.

From the above, we deduce that a large number of lateral samples combined with a high sampling frequency will give better results. For the propagation distance considered in this section, $F_s = 2/\lambda$ and $N = 1536$ gave very good results. The spatial aliasing might still turn out to be a problem for very large propagation distances, but these are the parameters of choice in the main simulation in Section 7.3. For the field considered in the current section, including 30 harmonics in the simulations seems to be adequate when setting $q = 0.35$. This will also be used in Section 7.3.

Simulations involving many harmonics and/or many lateral and axial samples are fairly time consuming. A simulation involving 50 harmonics with $N = 512$, $F_s = 1/\lambda$ and $\Delta z = \lambda$ took approximately 28 hours to run on a computer with 16GB ram and a 2.2 GHz Dual Core AMD Opteron Processor 275. Tripling N would nine-double the size of the DFT, which is responsible for a large part of the computation time. Setting $N = 1536$ thus leads to a substantial increase in computation time.

At the finishing stage of this thesis, the days were too limited to run all of the desired simulations in Section 7.3 with these selected parameters. Faced with a need to prioritize, the decision has been to run one simulation with these parameters out to 26 meters, and several shorter ones with $N = 768$ and $F_s = 1/\lambda$. As stated previously, this lead to undersampling of some of the higher harmonics. Only the first two harmonics are considered in this thesis, so as long as they are well-sampled, the results are still acceptable.

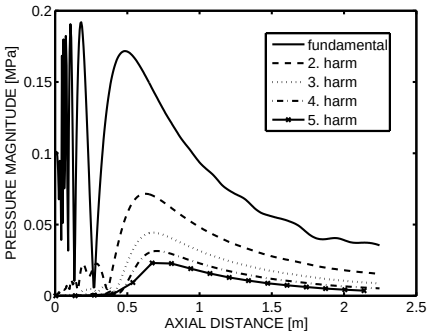

(a) Axial field, $Fs = 2$, $N = 512$.

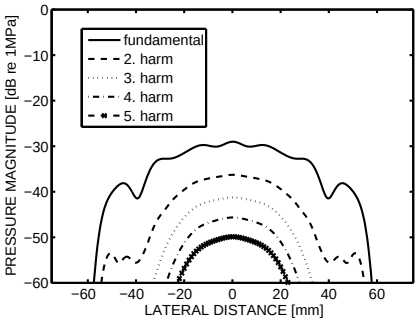

(b) Lateral field at 2.25 m, $Fs = 2$, $N = 512$.

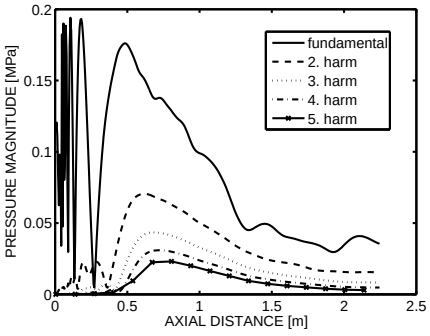

(c) Axial field, $Fs = 4$, $N = 512$.

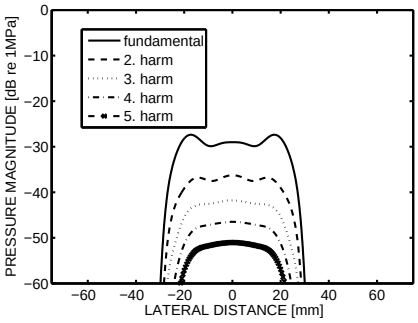

(d) Lateral field at 2.25 mm, $Fs = 4$, $N = 512$.

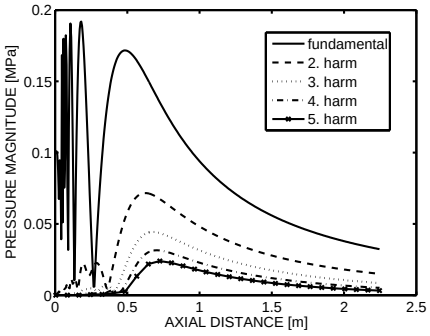

(e) Axial field, $Fs = 2$, $N = 1536$.

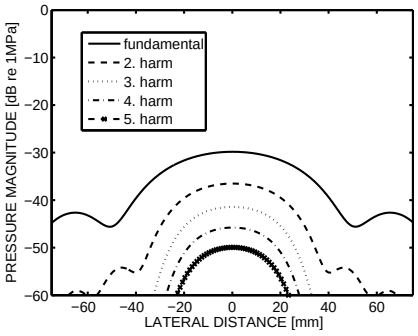

(f) Lateral field at 2.25 mm, $Fs = 2$, $N = 1536$.

Fig. 7.3: Field from the 2.25 MHz circular transducer, computed with attenuation.

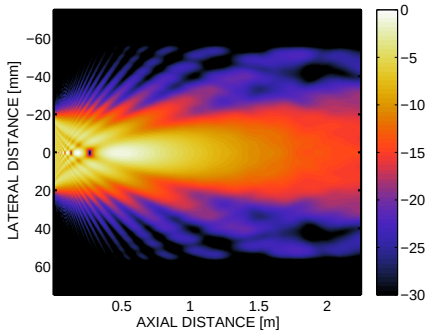

(a) First harmonic, $F_s = 2$, $N = 512$.

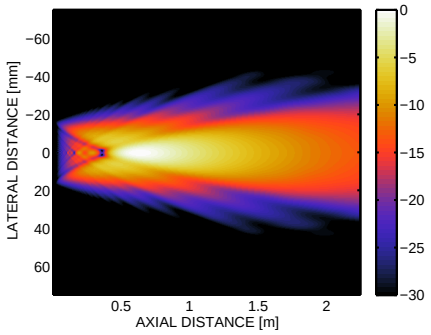

(b) Second harmonic, $F_s = 2$, $N = 512$.

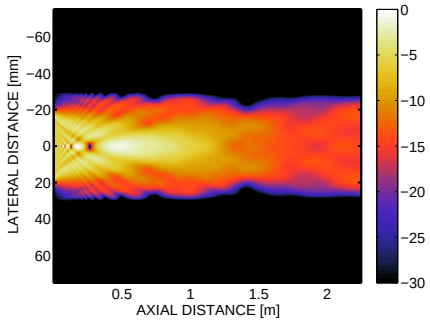

(c) First harmonic, $F_s = 4$, $N = 512$.

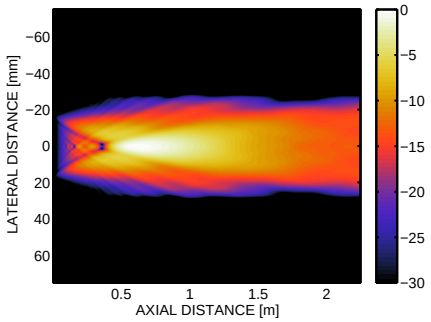

(d) Second harmonic, $F_s = 4$, $N = 512$.

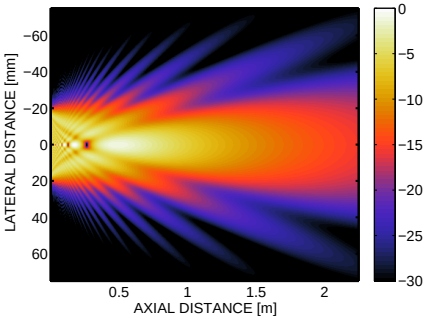

(e) First harmonic, $F_s = 2$, $N = 1536$.

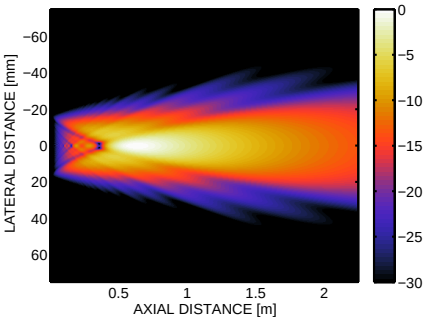

(f) Second harmonic, $F_s = 2$, $N = 1536$.

Fig. 7.4: Log scaled field in the xz-plane of the transducer used by Baker *et al.*.

7.2 Nonlinear effects on target strength measurements

We now return to the topic of target strength (TS), defined in Chapter 3 as

$$\mathrm{TS} = 10 \log_{10}(\sigma_{\mathrm{bs}}), \tag{7.1}$$

where

$$\sigma_{\mathrm{bs}} = R^2 \, \frac{I_{\mathrm{bs}}}{I_{\mathrm{i}}}, \tag{7.2}$$

is the backscattering cross-section.

To be able use a returned signal to deduce anything about insonified targets, the target strength of different targets needs to be known. Measuring target strength accurately is important, because the TS of a single scatterer is often used to calibrate echosounders. Calculating TS of fish based on acoustical theory and knowledge of the fish's composition is only accurate to a certain extent, because of all the factors contributing to target strength, discussed in Section 3.3.

Measuring the backscattered intensity of a single target is described by the active sonar equation (Urick 1983)

$$\mathrm{EL} = \mathrm{SL} + \mathrm{TS} - 2\mathrm{TL}, \tag{7.3}$$

where the echo level EL is the sound pressure level of the backscattered sound at the location of the transducer. The source level SL is defined as the on-axis sound pressure level at some distance r_0, usually unity. When assuming linearity, the only energy loss included is the transmission loss TL due to diffraction and attenuation. In Eq. (7.3), TL is counted twice to account for both directions of propagation.

As previously seen in Chapter 5, nonlinear effects may lead to excess attenuation of the wave. Neglecting these effects would cause TS to be measured as lower than it really is. If the nonlinear loss is large, the acquired information about the target might be misleading.

Nonlinear effects are not accounted for in the echosounders used today, but it is likely that they influence the measurements, especially those done with high-frequency sources.

Tichy *et al.* (2003) measured and simulated target strength along the beam axis for a 200 kHz echosounder operating in fresh water. They found the nonlinear losses in this case to be of such dimensions that they need to be accounted for in the TS measurements. How to perform this adjustment might not be well known in all cases, as their results indicate that the

nonlinear attenuation is dependant on both target range and the power level of the transducer. Tichy *et al.* propose that the lowest practical power level should be used to minimize nonlinear losses. In view of an ongoing discussion in this thesis - whether harmonic imaging is applicable in sonars - one might propose the opposite. This would increase the nonlinear losses, and thus the level of the second harmonic would be higher. However, this is not always practical. High power levels heat up the transducer, and very high voltages applied over time may also cause mechanical fatigue to the piezoelectric material the transducer consists of.

Large power levels may in some cases also induce cavitations (Simmonds and MacLennan 2005). Close to the surface, the ambient density is 1 atm. It grows with depth, as the temperature drops. If the transducer is not that deeply immersed, and operates with a high initial pressure, it is possible that the minimum resultant pressure approaches zero. This means that a vacuum has been generated. As the transducer vibrates, the vacuum collapses, and this results in explosive sounds known as cavitations. The chance of this happening is smaller for greater depths of the source, and for smaller initial pressures. As the resultant pressure cannot be negative, this limits the maximum waves that may exist in the water medium. Cavitations form more quickly in bubbly water.

The presence of bubbles in the water produces excess nonlinear effects, much like the contrast agents acquainted in Section 5.3. Small air bubbles are quite common right below the surface of the ocean, caused for instance by breaking waves or the wakes of ships. Larger bubbles rise quickly to the surface, while small bubbles may persist for hours or even days. Microbubbles of air may also be trapped as acoustical equipment is lowered into water. To reduce this possibility, the equipment is often covered with soap before immersed in water.

7.3 The field from the ES200-7C transducer

Echosounders are used in fisheries research in rivers, lakes and seas, and therefore encounter waters of very different temperatures, salinities and densities. Fresh water at room temperature is a special case, rarely found in nature, yet measurements are often performed here. The measurements made by Tichy *et al.* (2003) were performed in a freshwater tank, and the water temperature was approximately 18°C. The source used in the measurements was a ES200-7C transducer, shown in Fig. 7.5. The transducer has a radius A of 34.5 mm, a center frequency of 200 kHz and a bandwidth of almost 100 kHz.

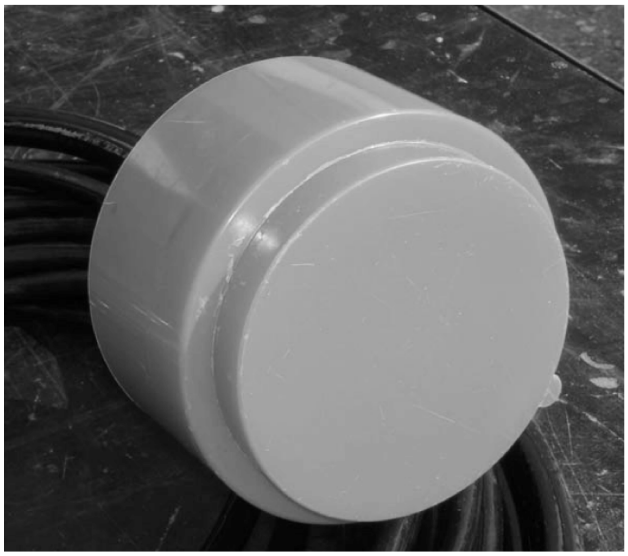

Fig. 7.5: The 200 kHz ES200-7C echo sounder transducer.

The simulated results of Tichy *et al.* were calculated by means of the KZK-equation. As noted in Chapter 4 and shown in Section 6.4, this may fail in the near field. The near field/far field crossover of this source is located at approximately 63.5 cm.

Tichy *et al.* performed measurements at different ranges for different power settings, and both were found to influence the amount of nonlinear loss. The nonlinear loss can be calculated by finding the difference between the linear and the nonlinear results for the fundamental for that power setting.

In the main simulations in this thesis, presented in the current section, we will consider the same source as the one used by Tichy *et al.*, the ES200-7C transducer. We would like to investigate the field of this source, to assess the size of the nonlinear effects. Another objective of this section is to investigate the possibility for utilizing the field of the second harmonic. It could perhaps be used in imaging situations or for TS measurements, if the quality and range of the beam is appropriate for such purposes.

Several power settings, given in Table 7.1, will be considered. They coincide with some of those considered by Tichy *et al.*, and we would like to see if the same results are output by our model. The normal maximum power setting for this particular transducer is 1000 W when used in fisheries research (Pedersen 2006).

As power equals intensity times area (Young and Freedman 2004), the

Power setting	**RMS velocity** v_{RMS}	**Peak velocity** $v_0 = \sqrt{2} \cdot v_{\text{RMS}}$
56 W	0.0986 m/s	0.1349 m/s
330 W	0.2393 m/s	0.3384 m/s
560 W	0.3118 m/s	0.4410 m/s
1000 W	0.4167 m/s	0.5893 m/s
1100 W	0.4370 m/s	0.6180 m/s

Table 7.1: Conversion from power to peak velocity.

initial velocity may be calculated using the following formula

$$v_{\text{RMS}} = \sqrt{\frac{P}{\rho c \pi A^2}} \,, \tag{7.4}$$

which gives the initial velocities displayed in Table 7.1. The transmitted-power levels used by Tichy *et al.* were calculated by measurements of electric potential over the transducers terminals. They are averaged values, and so the velocity values given by Eq. (7.4) are root mean square values of velocity. To obtain initial peak velocity, they must be multiplied by $\sqrt{2}$. These final values are also given in Table 7.1.

The beampattern of the ES200-7C transducer is displayed in Fig. 7.6(a). This particular transducer has a beamwidth of 7°. Tichy *et al.* mention that the transducer signals are weighted to reduce the sidelobe levels. This changes the beampattern, and will cause the field to be different from that achieved with uniform weighting.

The details of the weighting applied is not elaborated in the article (2003), but a common weighting in such cases is one correspondent to a Hamming window. Assuming this is done by Tichy *et al.* we may try to apply the same weighting by multiplying the discretized source with such a window. The Hamming window is similar to the Tukey window previously mentioned, but does not have a large uniform plateau of value 1, or value zero at the edges. The difference between the two windows is illustrated in Fig. 7.7.

The choice has been to apply an $L_x \times L_y$ hamming window which is multiplied by 2. This will lead to a peak velocity that is greater than v_0 in the middle of the transducer, and smaller at the edges. The sum of the weighting remains the same as if uniform weighting is applied.

The beampattern of the transducer after applying the Hamming window is shown in Fig. 7.6(b). Compared to Fig. 7.6(a), the level of the sidelobes has been reduced by approximately 18 dB. Lower sidelobe levels generally lead to a better clutter suppression, but come at the cost of a wider mainlobe, which reduces resolution.

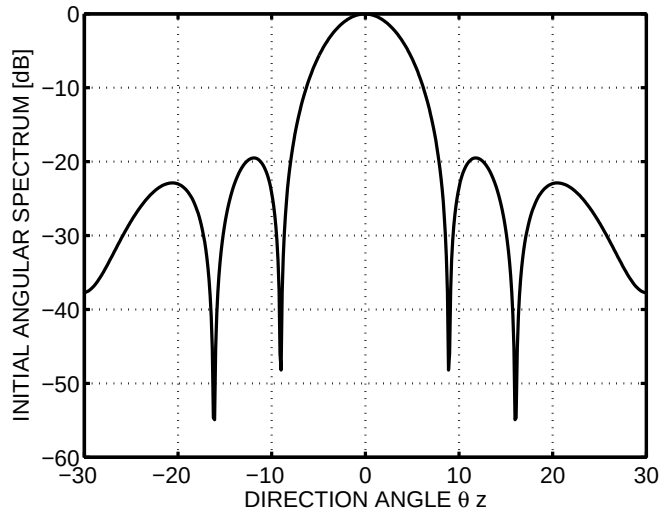

(a) Beampattern with uniform weighting of the transducer.

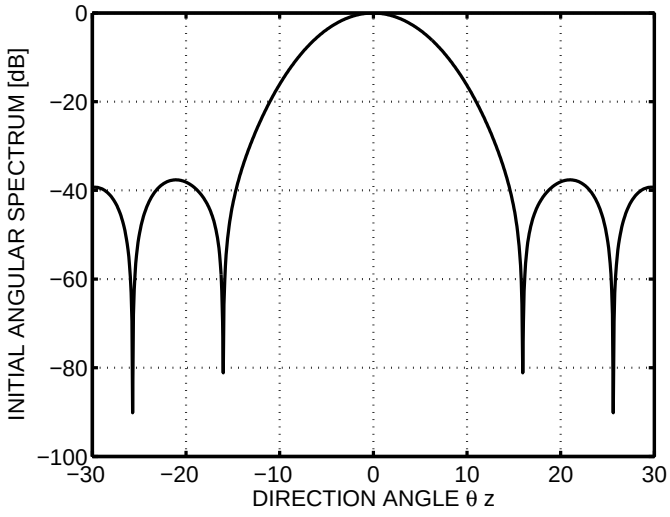

(b) Beampattern after applying the Hamming window. Weighting the transducer lowers the sidelobe levels at the cost of a wider mainlobe.

Fig. 7.6: Beampattern of the 200 kHz ES200-7C transducer. The transducer has a beamwidth of 7°.

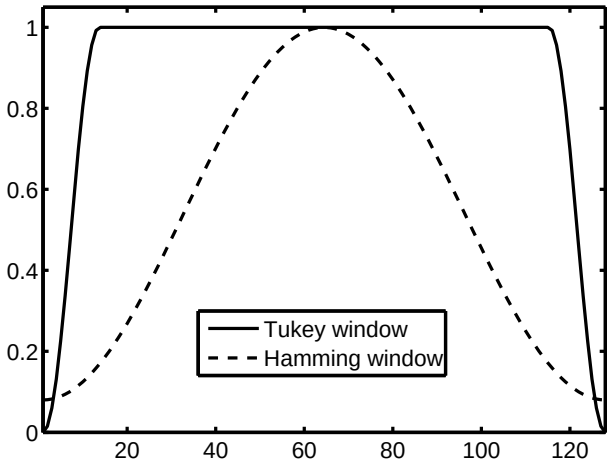

Fig. 7.7: Comparison of the 128 point Hamming window and the Tukey window.

Main simulation: The field for the power setting 1000 W

In the main simulation we will consider the power setting of 1000 W. The field will be propagated out to 3500 $\lambda = 26.25$ meters using $F_s = 2$ and $N = 1536$, consistent with the discussion in Section 7.1. All other parameters for the simulations presented throughout this section are summarized in Table 7.2.

The axial field from the transducer as calculated by the simulator is shown in Fig. 7.8. The fundamental reaches its maximum almost instantly. The maxima of the higher harmonics follow shortly thereafter, whereupon the values drop rather quickly. The fundamental drops to one tenth of its maximum value in less than two meters.

The log scaled field in the xz-plane is displayed for the first two harmonics in Fig. 7.9. The sidelobes are not visible because their values have been lowered trough applying the Hamming window.

Tichy *et al.* display the waveform of the pulse at 0.25 m, 1m and 7 m together with the corresponding FFTs in their Figure 3. The FFT values were provided by the Agilent 54621A oscilloscope used to sample the hydrophone signal. The FFT values show how the energy of the higher harmonics relative to the fundamental increases with propagation distance. From Chapter 5, we know that this indicates a highly distorted waveform. This is supported by the waveforms in Tichy *et al.*'s Figure 3.

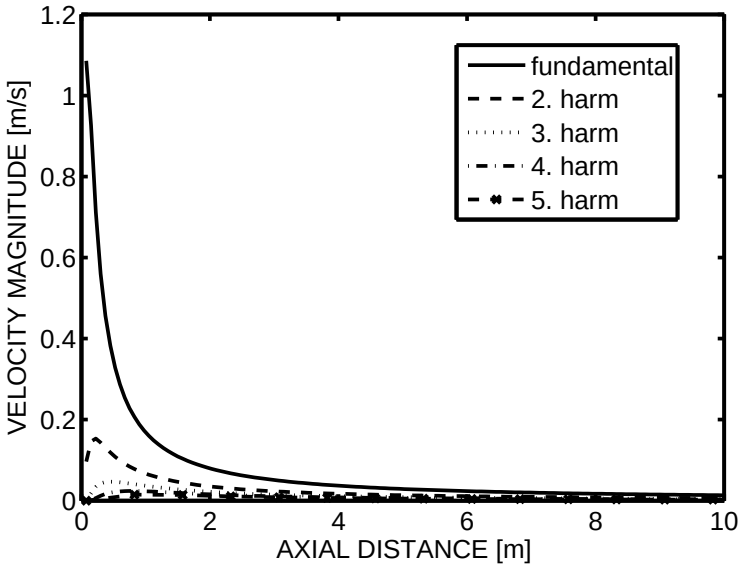

(a) Nonlinear field computed with 30 harmonics.

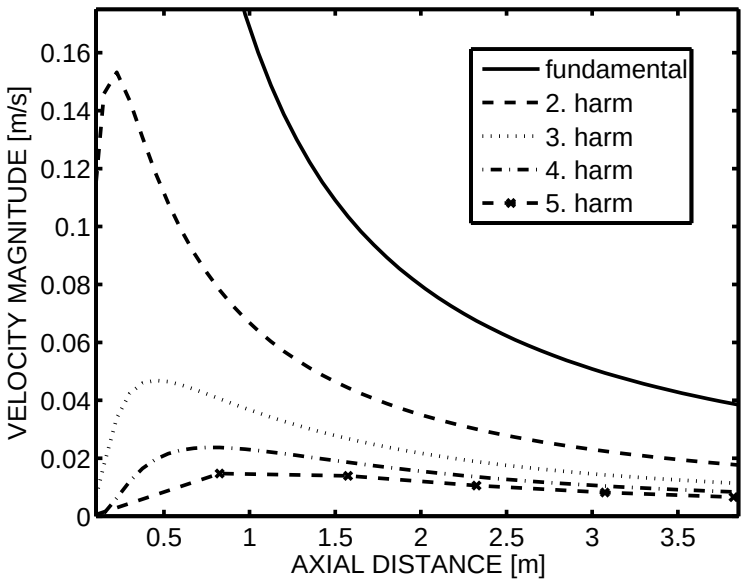

(b) The zooming in of (a).

Fig. 7.8: Axial field of the weighted transducer, for the power setting 1000 W.

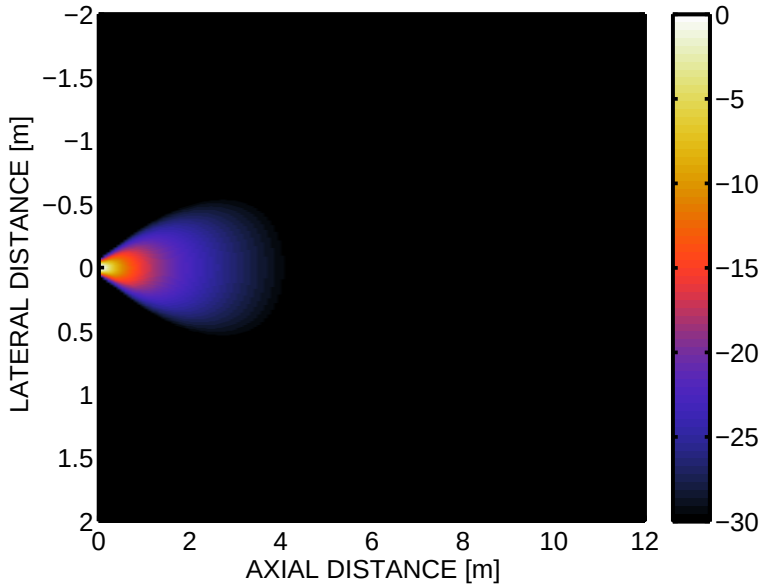

(a) Fundamental.

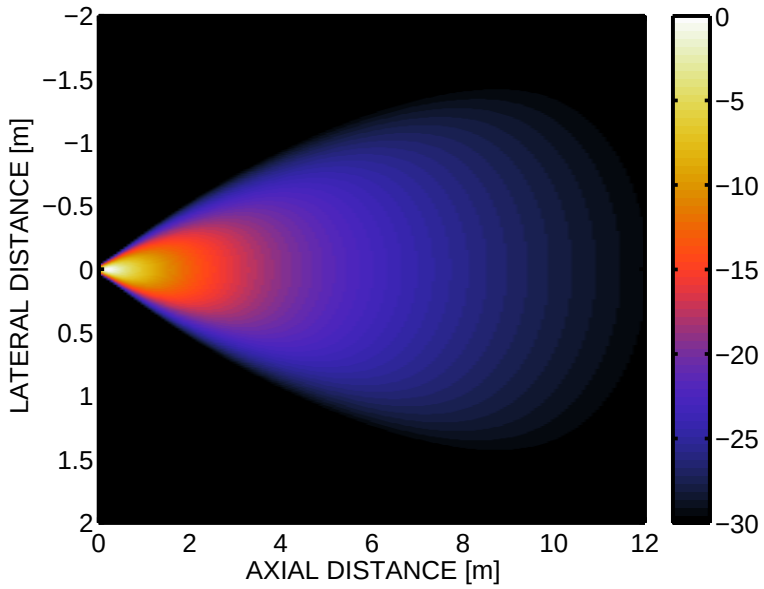

(b) Second harmonic.

Fig. 7.9: Log scaled field from the weighted transducer in the xz-plane.

The FFT values output by our model are shown in Fig. 7.10 for several ranges. They differ somewhat from those obtained by Tichy *et al.*. The simulator generally finds less energy in the second and third harmonic, and more energy in fourth and fifth harmonic than what is apparent from Tichy *et al.*'s Figure 3. For the ranges 1 m and 7 m, the levels of the second and third harmonic are about 5 dB lower than the measured values, while the fourth harmonic is about 2 dB higher. Altogether, the energy in the higher harmonics is calculated to be lower than the corresponding measurements for all ranges.

The values in Fig. 7.10 are computed directly in the axial points of interest. Remembering from Section 6.4 that the hydrophone has a certain spatial extent, this implies that it will average its measurements to some degree. This motivates us to try to average the FFT values with the values in the eight neighboring grid points. Hopefully, the averaged results will more closely resemble Tichy *et al.*'s Figure 3.

The averaged FFT values are displayed in Fig. 7.11. The relative levels of the higher harmonics are a lot larger now. However, they still do not agree with the values given by Tichy *et al.*. The level of the second harmonic is in much better agreement with the measured value, but the third and higher harmonics are much too high.

The averaging had a huge effect on the level of the FFTs, and it is possible that it should be performed differently. As the lateral grid points are $\Delta d = 1/F_s = \lambda/2$ apart, and the axial grid points are $\Delta z = 8\lambda$ apart, the averaging points may not have been spread out evenly enough. The averaged values were recalculated by considering surrounding points equidistant (Δz) from the points of interest. However, the result (displayed in Fig. D.7) was not much of an improvement. Several other averaging points were tested without much luck in attaining the desired values.

There are many possible reasons for why the simulator does not completely reproduce the values given by Tichy *et al.*.

As $\Delta z = 8\lambda = 6$ cm, the grid points do not completely coincide with the announced axial distances. Still, being within 2 cm of them, it is unlikely that this is responsible for the differences.

The neighboring points used in the averaging may be too far apart, and possibly the result for the FFTs would have been better if the field had been calculated using a smaller Δz.

Due to an error discovered too late in the process to correct, the Hamming window applied is not completely circular symmetric. Better results could perhaps be attained if this had been the case. The difference on the beam axis should not be large, but as we average with off-axis points, it could cause some deviation from a source applied a circular symmetric window. It is also

possible that the weighting applied by Tichy *et al.* is not consistent with a Hamming window, and that a different window altogether should be applied.

The difference in FFT values may arise simply because the applied power level is not completely equal to what is applied by Tichy *et al.* The article (2003) states that the acoustic power was around 1000 W. This was interpreted to be the averaged value, but this should possibly have been confirmed with Tichy *et al.*.

Simmonds and MacLennan comment on the article by Tichy *et al.* in their book (2005, page 38). They refer to the article by Shooter *et al.* (1974) which deals with the theoretical shock distance and acoustic saturation. The work of Shooter *et al.* was previously mentioned in Section 5.2.

More attenuation is apparently present in Tichy *et al.*'s short range results than what is predicted by Shooter *et al.*'s calculations and measurements. Simmonds and MacLennan also point out that the waveforms shown by Tichy *et al.* are asymmetrical, and that this is an indication of their results being influenced by other unknown factors. For ranges greater than 5 m, the two results agree with each other.

This implies that the FFT values displayed in Tichy *et al.*'s Figure 3 for 0.25 m and 1 m might not be completely accurate. Our only basis for comparison will then be the FFT values at 7 m.

As time was too limited to repeat the simulation with the suggested improvements, we have little choice but to accept the presented results. The averaged value for 7 m is not that far off for the second and third harmonic, but is too high for the fourth harmonic.

Having discussed the differences, there are also some obvious similarities between Fig. 7.11 and Tichy *et al.*'s Figure 3.

Energy has been transferred to higher harmonics due to nonlinear effects, which will lead to a nonlinear loss of the field. The energy contained in the higher harmonics relative to the fundamental is larger at 1 m than it was at 0.25 m, and larger still at 7 m.

At 12 m, the levels appear to be unchanged from those at 7 m. This means that the values of the higher harmonics relative to the fundamental have been constant for 5 meters of propagation, implying that the fields have been attenuated equally. FFT values at 12 m are not displayed by Tichy *et al.*, so whether they obtained a similar result or not is unknown.

Parameter	**Symbol**	**Value**
Fundamental frequency	f0	200 kHz
Density	ρ	1027 kg/m^3
Sound speed	c	1500 m/s
Harmonics used in simulation	M	30
Lateral samples	N	768 (1536)
Steplength	Δz	8λ
Sampling frequency	F_s	$1/\lambda$ $(2/\lambda)$
Radius	A	0.0345 m
Nonlinear coefficient	β	3.5
Attenuation coefficient	α_0	$25 \cdot 10^{-15}$ Np/m/Hz^2
Frequency dependency	b	2
Upramping constant	q	0.35

Table 7.2: Parameters used in main simulations.

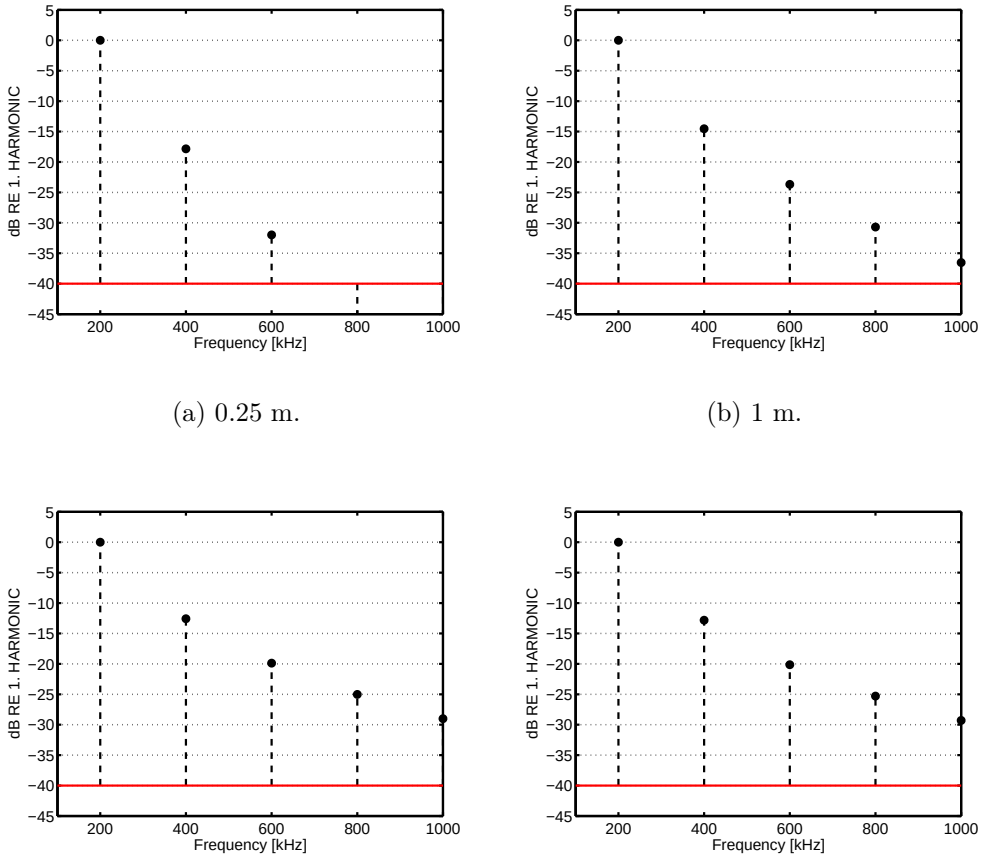

(a) 0.25 m.

(b) 1 m.

(c) 7 m.

(d) 12 m.

Fig. 7.10: FFT of field at different ranges, for the power setting 1000 W.

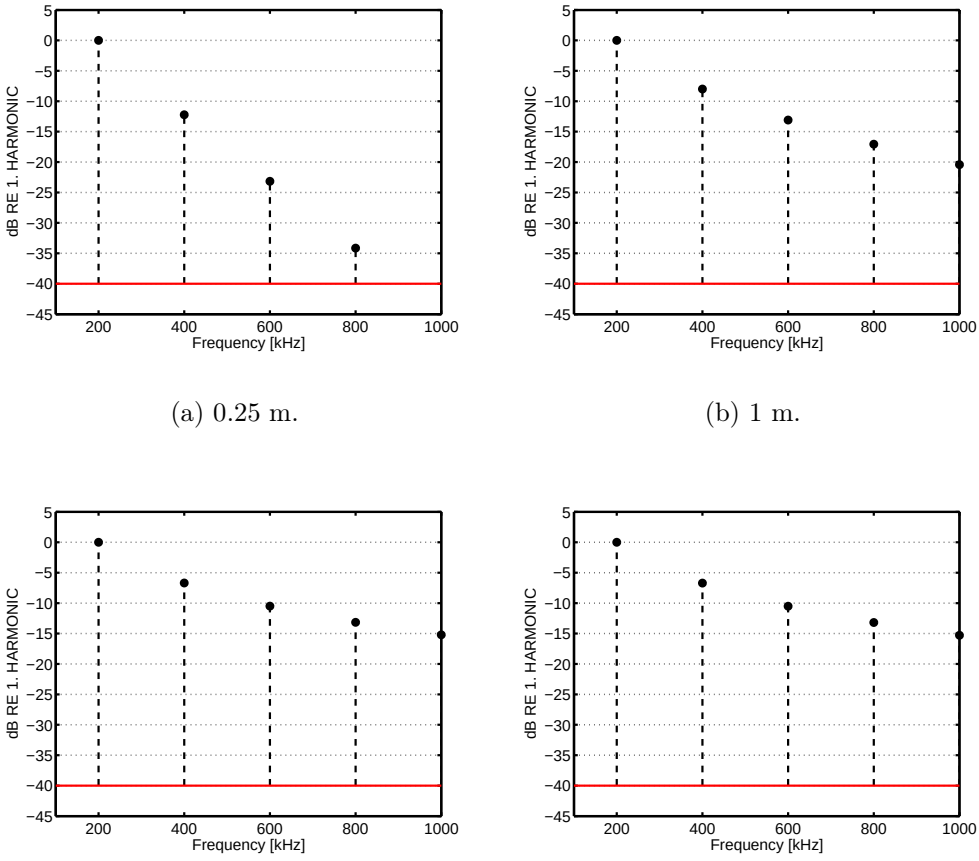

(a) 0.25 m.

(b) 1 m.

(c) 7 m.

(d) 12 m.

Fig. 7.11: Averaged FFT of field at different ranges, for the power setting 1000 W. Value in point of interest is averaged with the 8 neighboring points.

Investigating the field of the second harmonic

We would like to see how the second harmonic develops with increasing propagation distance. From the conclusions just made from the FFT values in Figs. 7.10 and 7.11, we expect its level relative to the fundamental to grow initially, and then stabilize after 7 meters.

The log scaled axial field, displayed in Fig. 7.12(a) supports this prediction. The levels of both the fundamental and the higher harmonics seem to behave as linearly decaying functions after some propagation distance has been reached. This means that the relative levels stay approximately constant, which is also understood from Fig. 7.12(b). Apparently the levels stabilize before 7 m is reached, possibly as early as 3 meters, and the second harmonic seems to stabilize at a level 7 dB below the fundamental.

To investigate the development of the second harmonic, we consider the lateral field profile for different ranges. In the following, we only consider the second harmonic, but the third harmonic is shown for illustrative purposes. The lateral velocity field at several ranges is shown in Fig. 7.13, and Fig. 7.14 shows the normalized log scaled lateral fields. What is evident from these plots, is that the second harmonic generally has a narrower field profile than the fundamental. Also, the sidelobes of the fundamental are visible for the ranges of 1 m and 7 m, but this is not the case for the second harmonic. This indicates that the second harmonic has a lower sidelobe structure. The lateral field is cut off at 4 meters, which is visible in Figs. 7.14(e) and (f).

These results are promising, as this would lead to images of both higher resolution and less noise, compared to images produced by the fundamental. This means that the second harmonic can be utilized to a great advantage in imaging situations, if it contains so much energy that it can be detected. However, as the beam is narrower than the fundamental's, beams must be sent in a few more directions to cover the same area.

In target strength measurements, the second harmonic might contain additional information which could be combined with what is output from the fundamental. As a result, more accurate measurements can be obtained.

From Fig. 7.12(a), we can see that the fundamental has dropped to -42 dB of its initial value at 15 m. Assuming the transducer is able to detect this signal, it will also be able to detect the signal of the second harmonic at approximately 7.5 m, because the second harmonic contains the same energy here. The lateral field profile at 7 m, displayed in Fig. 7.14(d), demonstrates that imaging using the second harmonic is a better choice at this range, even though the fundamental's signal is 7 dB stronger.

Today's sonars are not generally able to receive at the second harmonic because the bandwidth is too small. These results indicate that it could

be a good idea to develope a sonar of a wider bandwidth. Developing new transducers with various desired qualities is a costly process. It might not be easily accomplished, but transducers who receive at the second harmonic are operative in medical ultrasound.

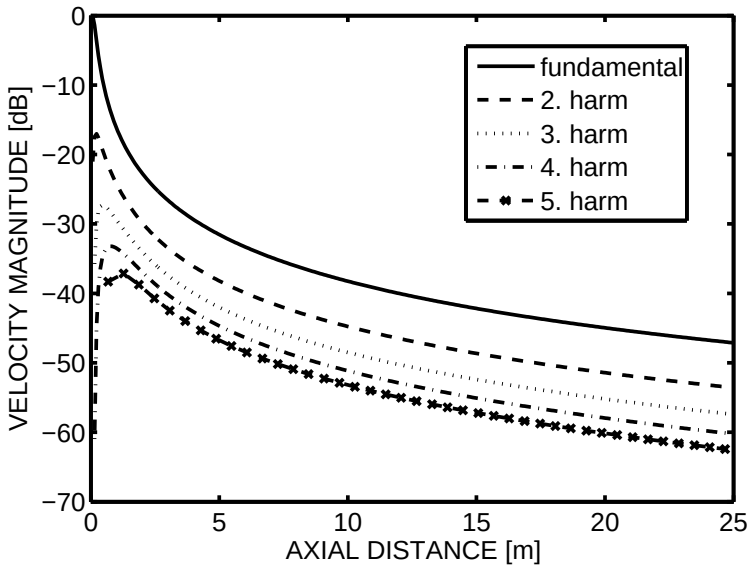

(a) Field of harmonics relative to the fundamental's maximum.

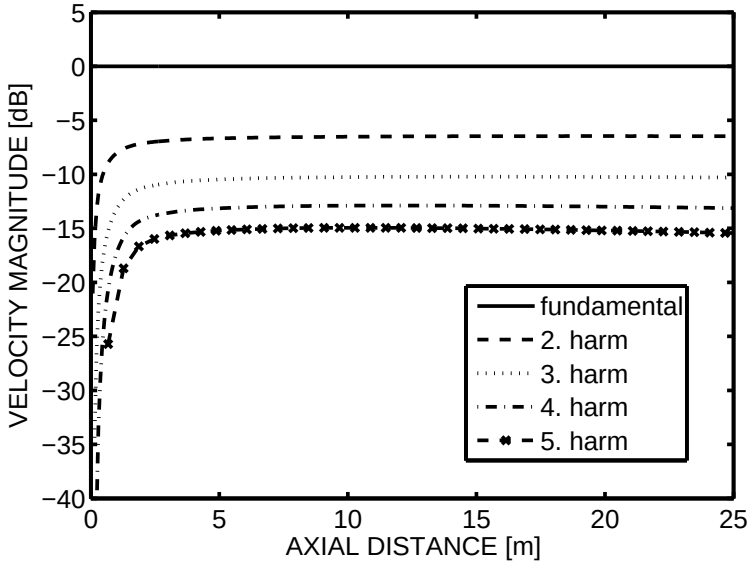

(b) Field of harmonics relative to the fundamental.

Fig. 7.12: Log scaled axial field of the weighted transducer, for the power setting 1000 W.

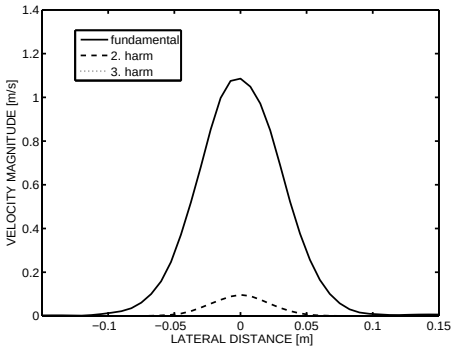

(a) 0.075 m, field in m/s

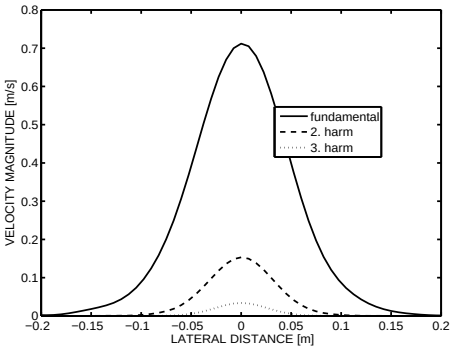

(b) 0.25 m, field in m/s

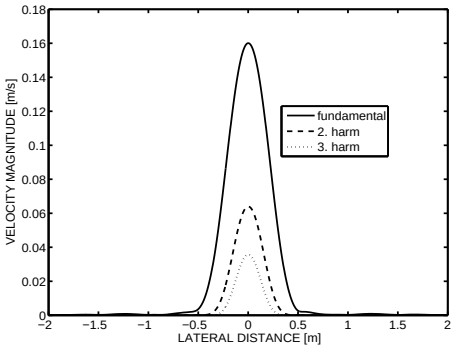

(c) 1 m, field in m/s

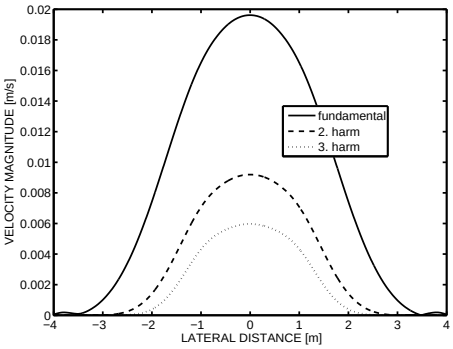

(d) 7 m, field in m/s

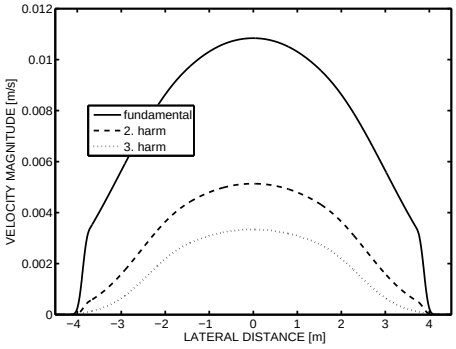

(e) 12 m, field in m/s

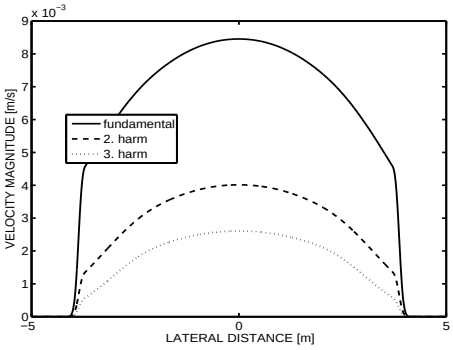

(f) 15 m, field in m/s

Fig. 7.13: Lateral velocity field from the weighted transducer.

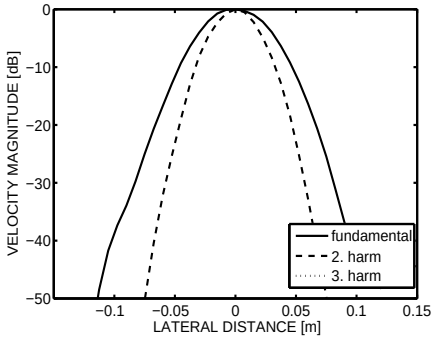

(a) 0.075 m.

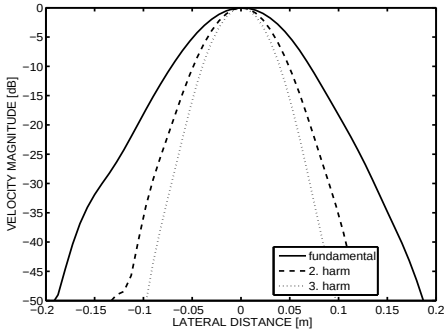

(b) 0.25 m.

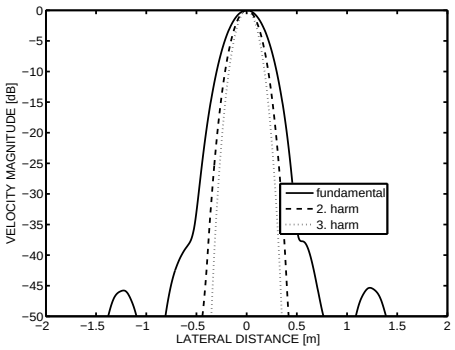

(c) 1 m.

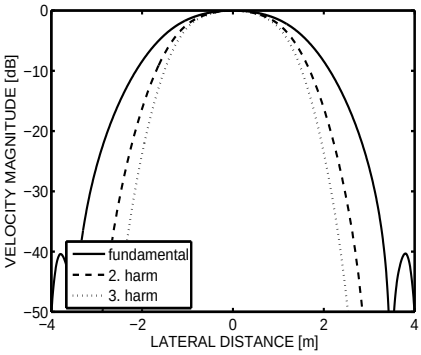

(d) 7 m.

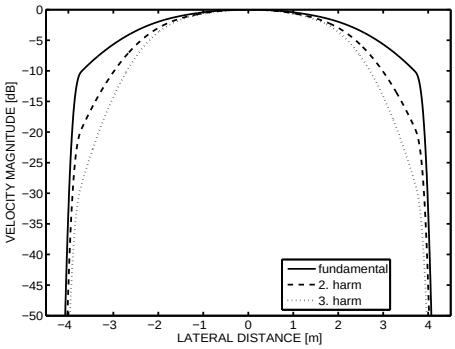

(e) 12 m.

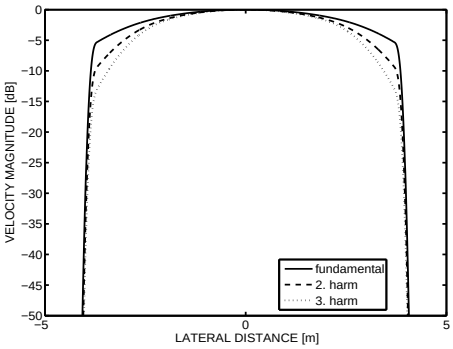

(f) 15 m.

Fig. 7.14: Log scaled lateral velocity field from the weighted transducer.

Nonlinear loss as a function of range and power setting

The nonlinear loss is a measure of the excess attenuation due to nonlinear effects on the field. This can be found by simulating the field both linearly and linearly, and taking the difference between the two calculated fundamentals. For the power setting 1000 W, the simulated nonlinear loss is displayed in Fig. 7.15. The nonlinear loss reaches several decibels in this case. According to this result, the sound pressure level at 12 meters is halved compared to what it would have been, had the propagation been a linear process. This means that it is very likely that target strength measurements performed with this source will be erroneous at this power setting.

Tichy *et al.* display the nonlinear loss as a function of range for several power settings in their Figure 4. Their simulated result for the power setting 927 W agrees with Fig. 7.15 up to the axial distance of 2 meters. After that, it shows a loss between half a dB and one dB greater than what is output from our model. This is consistent with our FFT values showing less energy in the higher harmonics. At 7 meters, Tichy *et al.* simulated a nonlinear loss of 3.25 dB, while Fig. 7.15 shows a loss of 2.5 dB at this location. The shapes of the curves are however similar, and show a great nonlinear loss in the beginning of the field. The loss continues to grow, but at a gradually decreasing rate. This is also consistent with what the FFT values showed, and the log scaled axial field displayed in Fig. 7.12.

The time was unfortunately too limited to run a simulation of this power setting out to larger axial distances. Tichy *et al.* performed such a simulation for the power setting of 330 W out to 260 meters. The result displayed an additional 2 dB nonlinear loss beyond the 2 dB loss present at 10 m. The loss displayed in Fig. 7.15 also seems to continue to grow after the propagation distance of 26 meters.

To investigate the nonlinear loss further, the field from the ES200-7C echosounder transducer was recalculated for the different power settings shown in Table 7.1. As previously mentioned, these simulations were performed with $F_s = 1/\lambda$ and N equal to 768 to save computation time. We anticipate that the higher harmonics may be undersampled as a result. Additionally, they have only been simulated out to the propagation distance of 12 m. This range was chosen to have time to run the simulation for all the power settings. As the levels seem to start stabilizing before this range, we should very well be able to discuss the properties of the different curves. The results reported by Tichy *et al.* also cut off at 12 m.

The log scaled axial velocity fields are displayed in Fig. 7.16. The spatial aliasing is readily visible for the fourth and fifth harmonic, especially in Fig. 7.16(d). The second and third harmonic do however seem well-sampled.

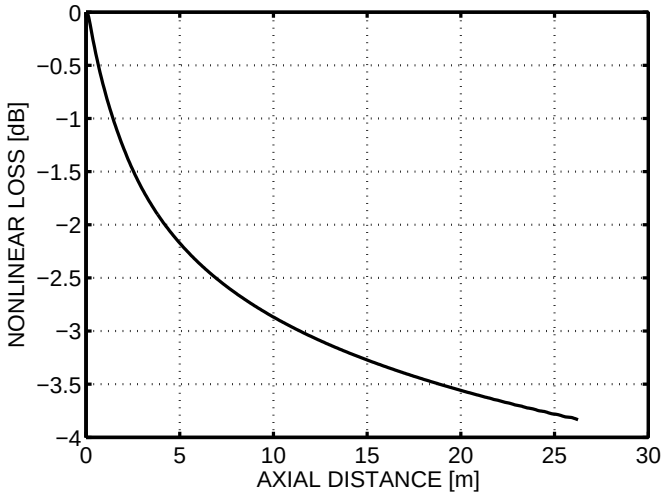

Fig. 7.15: Nonlinear loss as a function of range for the power setting 1000 W.

As was the case for the power setting 1000 W, the rate with which the fundamental loses energy to the higher harmonics decays with increasing range. After propagating some distance, the levels stay almost constant relative to each other.

The nonlinear loss for all the power settings in Table 7.1 is shown in Fig. 7.17. The result does show some similarities to Tichy *et al.*'s Figure 4. The nonlinear loss clearly is larger for larger initial power settings, and increases with range. None of the curves seem to have stopped decaying at the range of 12 m, so additional losses are expected with larger propagation distance.

These results allow us to agree with Tichy *et al.* in that transmitted power is an important factor for the amount of nonlinear effects. For the largest considered power levels, the nonlinear loss reaches up to more than 3 dB, and still shows sign of increasing further. This could have a drastic impact on target strength measurements and other measurements performed at these power levels, for the source considered.

One interesting result is that the simulated loss for 1100 W is actually slightly lower than the loss displayed for 1000 W. Figure 4 in the article agrees with this fact for the most part, but this has not been commented on by Tichy *et al.*. It could be interesting to run simulations for more power settings around and above this level, to see where those curves lie.

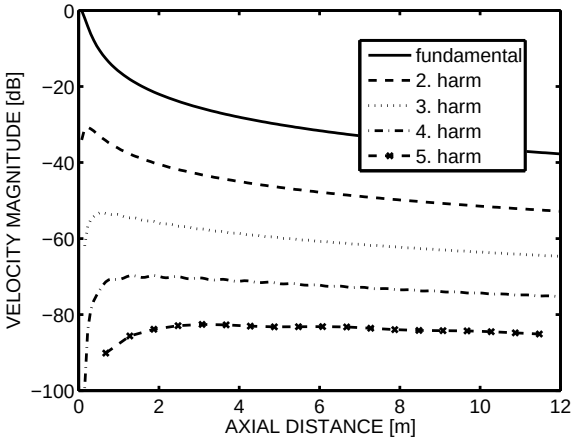

(a) 56 W.

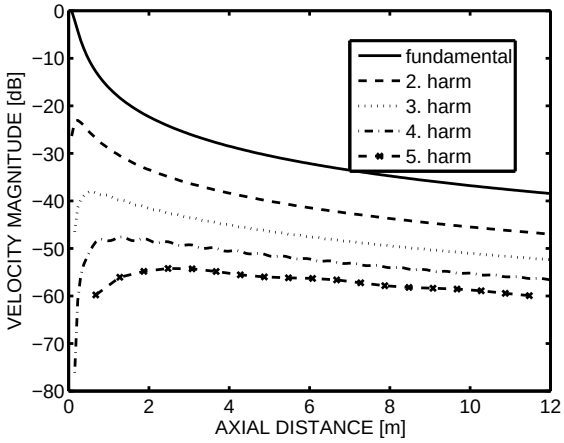

(b) 330 W.

Fig. 7.16: Log scaled axial field of the weighted transducer, for different power settings.

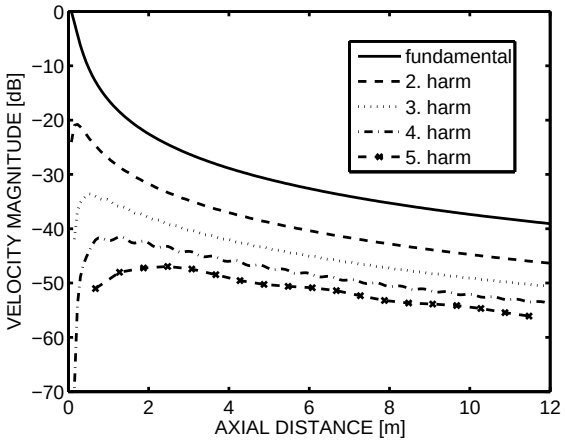

(c) 560 W.

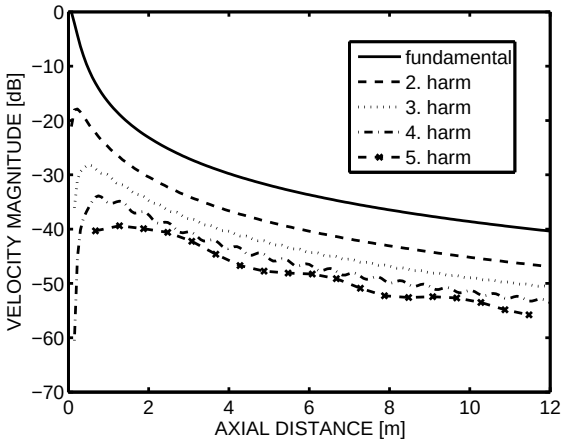

(d) 1100 W.

Fig. 7.16: Log scaled axial field of the weighted transducer, for different power settings (Cont.).

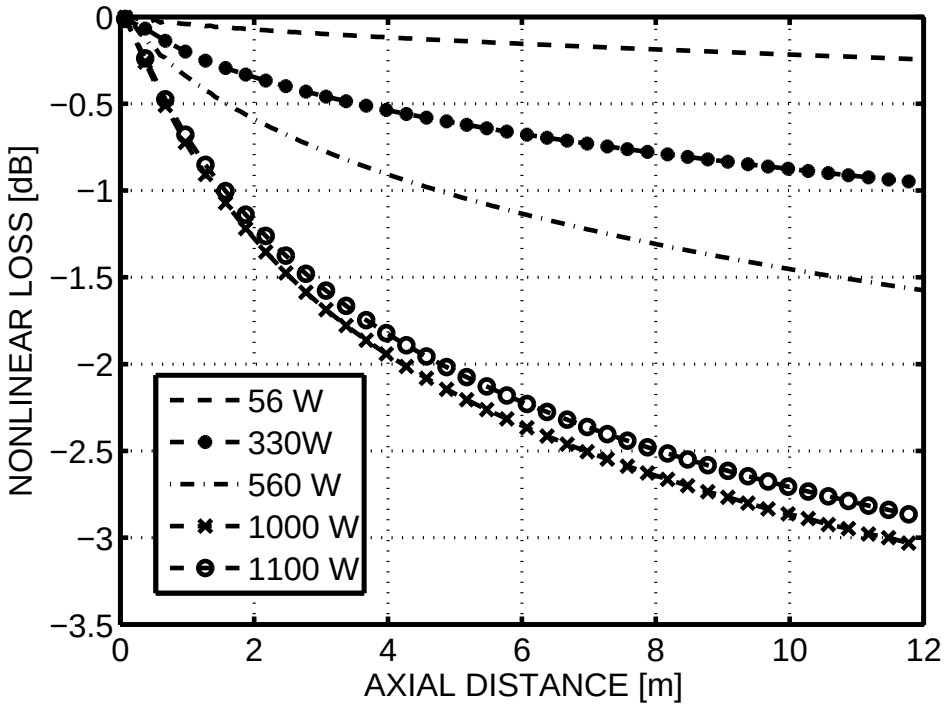

Fig. 7.17: Nonlinear loss as a function of range for several power settings.

Chapter 8

Conclusion

The present chapter concludes this thesis. A summary of the work and results presented is given in Section 8.1, and section 8.2 suggests some further investigations that may be done.

8.1 Summary

A simulator has been developed which calculates the linear and nonlinear propagation of acoustic fields. The effects of diffraction, attenuation and nonlinearity are calculated in a step-by-step fashion, based on the known field at some source plane.

The calculation of diffraction was based on the angular spectrum method (ASA). Potential aliasing errors in the ASA and their remedies have been presented. Attenuation and nonlinear effects are added in a separate substep through a frequency domain solution of Burger's equation (FDSBE).

The simulator is applicable to transducers of arbitrary shapes. Its implementation was made with fields from sonars and echosounders in mind, but it could just as well be used to calculate general ultrasonic fields.

A few obstacles were met during the development of the simulator. Many versions of the FDSBE were encountered in literature, which made the implementation of the nonlinear substep a surprisingly time-consuming task. All encountered versions were tested in the simulation of a field for which measured results were available. Several simulations and error-seeking dismissed some of the candidates to likely be typographical errors. Eq. (5.10) stood out by giving results which were in excellent agreement with measured results reported in literature.

An initially erroneous value of the frequency dependence parameter b caused a lot of trouble. The field from a 2.25 MHz transducer was calculated

several times with highly unreasonable results. The fact that correct results were obtained out to a certain axial extent with attenuation neglected, led it to be ruled out prematurely as the cause of the problem. Several simulations were performed with different combinations of step-sizes, up-ramping coefficients q, the number of harmonics included, N and F_S to locate the problem. Attenuation is sometimes neglected altogether in literature when simulating ultrasonic fields in water. Apparently, this is not always recommendable when considering such fields at larger propagation distances.

Much effort was put into verifying the simulator. Simulations were performed for a variety of transducers operating in water, and the field on and off the beam axis was found to be in good agreement with reported results.

Certain parameters in the simulations affect the results a great deal. An investigation was performed to decide on the best choice of sampling scheme for the main simulation.

The thesis has considered the effects of nonlinear sound propagation on target strength (TS) measurements. The field for a transducer applicable to fishery research was simulated for several power levels to investigate the nonlinear losses. The results show slightly less nonlinear loss than what was reported by Tichy *et al.* for this source. Otherwise, the results are quite reasonable, and possibly the differences are simply due to incorrect parameters.

Judging from the obtained results, the amount of nonlinear loss is clearly dependent on both range and power level. For some power levels, the losses reach several decibels. In these cases, target strength measurements may be incorrect, and some form of compensation must be made.

TS measurements may benefit from considering the back-scattered second harmonic in addition to the fundamental. The field of the second harmonic on short ranges shows much promise of being used in imaging situations. Its lateral field profile is generally narrower than the fundamental's, which leads to a higher resolution. Information obtained from the second harmonic may successfully be combined with the fundamental's information, when both fields are detectable.

8.2 Suggestions for further work

The calculated field for the source used by Tichy *et al.* did not completely correspond with reported measurements. To find the cause of the differences, one could check if the parameters used in the simulations were correct. The weighting should be confirmed to see if it corresponds to a Hamming window,

and it should in any case be made circular symmetric before it is applied to the transducer.

The propagation distances considered in this thesis have been limited to 26 m or shorter. The main reason for this has been the time limitation, and the fact that the simulations were very time-consuming. It would be of interest to study the nonlinear losses and the field of the second harmonic for greater propagation distances. The simulator is ready to perform such large scale simulations.

To validate the simulator for larger propagation distances, measurements must be made for these propagation distances as well. As the size of pools and tanks is generally limited, such measurements probably must be made at sea. Making measurements in bubbly water may also be of interest, as microbubbles generally add to nonlinear effects. Modeling bubbly water would be a bit more challenging.

With increasing depth, the temperature of the sea generally decreases, and the ambient density increases. As the small-signal limit sound speed depends on these factors, it will vary as a function of depth. Such functions are called sound-speed profiles. If such a profile is determined through measurements, it would be straightforward to include it in the program.

An adaptive sampling scheme as described by Zemp *et al.* in their article (2003) may be used to modify the simulator. According to Zemp *et al.*, this could lead to the possibility of enlarging Δz significantly, which saves computation time.

In this thesis, only unfocused single-beam transducers have been considered. Focusing or steering could easily be applied to the transducer, but the resulting field should not come out that different.

In the study of nonlinear loss, a single frequency was considered in this thesis. A further study could be done to chart the nonlinear losses for several transducers, power levels and frequencies. To be able to correct for nonlinear losses, their approximate sizes must be known in each case. Perhaps such a study could unveil some sort of general rule or guideline on how the nonlinear losses depend on different factors. Such a study would be a major undertaking, but knowing how to correct for nonlinear effects when using sonars would be valuable information.

Bibliography

Averkiou, M. A., D. N. Roundhill, and J. E. Powers (1997). A new imaging technique based on the nonlinear properties of tissues. *Proceedings IEEE Ultrasonics Symposium 2*, 1561–1566.

Baker, A. C., K. Anastasiadis, and V. F. Humphrey (1988). The nonlinear pressure field of a plane circular piston: Theory and experiment. *The Journal of the Acoustical Society of America 84*(4), 1483–1487.

Christopher, P. T. and K. J. Parker (1991a). New approaches to nonlinear diffractive field propagation. *The Journal of the Acoustical Society of America 90*(1), 488–499.

Christopher, P. T. and K. J. Parker (1991b). New approaches to the linear propagation of acoustic fields. *The Journal of the Acoustical Society of America 90*(1), 507–521.

Enflo, B. O. and C. M. Hedberg (2002). *Theory of Nonlinear Acoustics in Fluids*. Kluwer Academic Publishers.

Fjellestad, H. (2000). Simulation of nonlinear ultrasound fields. mathematical modeling. Master's thesis, University of Oslo.

Hamilton, M. F. and D. T. Blackstock (Eds.) (1998). *Nonlinear Acoustics*. Academic press.

Haran, M. E. and B. D. Cook (1983). Distortion of finite amplitude ultrasound in lossy media. *The Journal of the Acoustical Society of America 73*(3), 774–779.

Heathershaw, A. D., P. D. Ward, and A. M. David (2001). The environmental impact of underwater sound. *Proc. Inst. Acoust 23*(4), 1–12.

Horne, J. K. (2000). Acoustic approaches to remote species identification: a review. *Fisheries Oceanography 9*(4), 356–371.

Johnson, D. H. and D. E. Dudgeon (1993). *Array Signal Processing, concepts and techniques*. Prentice Hall.

Korneliussen, R. J. (2002). *Analysis and presentation of multi-frequency echograms*. Ph. D. thesis, University of Bergen.

Marakov, S. and M. Ochmann (1997). Nonlinear and thermoviscous phenomena in acoustics, part ii. *ACUSTICA 83*, 197–222.

Misund, O. A. (1997). Underwater acoustics in marine fisheries and fisheries research. *Reviews in Fish Biology and Fisheries 7*(1), 1–34.

Morse, P. M. and K. U. Ingard (1968). *Theoretical Acoustics*. McGraw-Hill, Inc.

Oppenheim, A. V. and R. W. Schafer (1999). *Discrete-time Signal Processing*. Prentice Hall.

Orofino, D. and P. Pedersen (1993a, May). Efficient angular spectrum decomposition of acoustic sources. i. theory. *Ultrasonics, Ferroelectrics and Frequency Control, IEEE Transactions on 40*(3), 238–249.

Orofino, D. and P. Pedersen (1993b, May). Efficient angular spectrum decomposition of acoustic sources. ii. results. *Ultrasonics, Ferroelectrics and Frequency Control, IEEE Transactions on 40*(3), 250–257.

Pedersen, A. (2006). *Effects of nonlinear sound propagation in fisheries research*. Ph. D. thesis, University of Bergen.

Shooter, J. A., T. G. Muir, and D. T. Blackstock (1974). Acoustic saturation of spherical waves in water. *The Journal of the Acoustical Society of America 55*(1), 54–62.

Simmonds, J. and D. MacLennan (2005). *Fisheries Acoustics*. Blackwell Publishing.

Synnevåg, J.-F. (1998). Linear and nonlinear propagation of limited diffraction beams. Master's thesis, University of Oslo.

Tichy, F. E., H. Solli, and H. Klavenes (2003). Non-linear effects in a 200-khz sound beam and the consequences for target-strength measurement. *ICES Journal of Marine Science 60*(3), 571–574.

Trivett, D. H. and A. L. V. Buren (1981). Propagation of plane, cylindrical, and spherical finite amplitude waves. *The Journal of the Acoustical Society of America 69*(4), 943–949.

Trivett, D. H. and A. L. V. Buren (1984). Comments on "distortion of finite amplitude ultrasound in lossy media," by m. e. haran and b. d. cook [j. acoust. soc. am. 73(3), 774–779 (1983)]. *The Journal of the Acoustical Society of America 76*(4), 1257–1258.

Urick, R. J. (1983). *Principles of Underwater Sound*. McGraw-Hill Book Company.

Williams, E. G. (1983). Numerical evaluation of the radiation from unbaffled, finite plates using the fft. *The Journal of the Acoustical Society of America 74*(1), 343–347.

Williams, E. G. and J. D. Maynard (1982). Numerical evaluation of the rayleigh integral for planar radiators using the fft. *The Journal of the Acoustical Society of America 72*(6), 2020–2030.

Wu, P., R. Kazys, and T. Stepinski (1996a). Analysis of the numerically implemented angular spectrum approach based on the evaluation of two-dimensional acoustic fields. part i. errors due to the discrete fourier transform and discretization. *The Journal of the Acoustical Society of America 99*(3), 1339–1348.

Wu, P., R. Kazys, and T. Stepinski (1996b). Analysis of the numerically implemented angular spectrum approach based on the evaluation of two-dimensional acoustic fields. part ii. characteristics as a function of angular range. *The Journal of the Acoustical Society of America 99*(3), 1349–1359.

Wu, P., R. Kazys, and T. Stepinski (1997a). Erratum: Analysis of the numerically implemented angular spectrum approach based on the evaluation of two-dimensional acoustic fields. part ii. characteristics as a function of angular range [j. acoust. soc. am. 99(3), 1349–1359 (1996)]. *The Journal of the Acoustical Society of America 101*(4), 2395–2396.

Wu, P., R. Kazys, and T. Stepinski (1997b). Optimal selection of parameters for the angular spectrum approach to numerically evaluate acoustic fields. *The Journal of the Acoustical Society of America 101*(1), 125–134.

Wu, P. and T. Stepinski (1999). Extension of the angular spectrum approach to curved radiators. *The Journal of the Acoustical Society of America 105*(5), 2618–2627.

Young, H. D. and R. A. Freedman (2004). *Sears and Zemansky's University physics*. San Fransisco, Calif. : Pearson/Addison-Wesley.

Zemp, R. J. (2000). Modeling nonlinear ultrasound propagation in tissue. Master's thesis, University of Toronto.

Zemp, R. J., J. Tavakkoli, and R. S. C. Cobbold (2003). Modeling of nonlinear ultrasound propagation in tissue from array transducers. *The Journal of the Acoustical Society of America 113*(1), 139–152.

Appendix A

Nomenclature

j	imaginary unit, $\sqrt{-1}$
A	half the width of linear/planar source or source radius
B	half the height of planar source
c_0	small signal sound speed
λ	wavelength
f	frequency
T	period of wave
$\mathbf{k}$	wavenumber vector
k	wave number/radius of radiation circle $k = 2\pi f/c_0$
ω	angular frequency
M	number of harmonics in nonlinear propagation
N	number of lateral samples of source plane
$L_x,\ L_y$	number of lateral samples of source
F_s	spatial sampling frequency
Δd	spatial sampling interval
D	size of source plane
Δf	sampling frequency in spatial frequency domain
Δz	steplength in multistep algorithm
$\mathbf{v} = (v_x, v_y, v_z)$	velocity vector
v	velocity magnitude
v_0	initial peak particle velocity, piston source
p	sound pressure amplitude (complex)
p_0	ambient pressure
ρ	density
ρ_0	ambient density

$r,\ R$	distance from source
σ_{bs}	backscattering cross-section
$\sigma_{\mathrm{bs,eff}}$	effective backscattering cross-section
s_v	volume backscattering coefficient
TS	target strength
P	power
I	intensity
I_{inst}	instantaneous intensity
I_{bs}	intensity of backscattered sound
I_{i}	incident intensity
$V,\ V_D$	angular spectrum, $\mathcal{F}\{v\}$
$i_x,\ m_x$	indices
$i'_x,\ m'_x$	shifted indices
n	index – harmonic number
$\theta_x,\ \theta_y,\ \theta_z$	direction cosines of plane waves
$\mathbf{n} = (n_x, n_y, n_z)$	normal vector of plane wavefronts
h	point spread function
H	transfer function, $\mathcal{F}\{h\}$
β	nonlinear coefficient
B/A	nonlinear parameter
α	attenuation coefficient
α_0	attenuation coefficient $\alpha_0 = \alpha(nf_0)^b$
b	frequency dependency in attenuation
q	attenuation upramping parameter
∇^2	Laplacian operator
$\mathcal{F}\{\cdot\}$	Fourier transform

Appendix B

Derivations

This chapter includes some useful definitions and derivations used in this thesis.

B.1 The Fourier transform

Throughout this thesis, $\mathcal{F}\{\cdot\}$ denotes the Fourier transform, given by

$$F(\varepsilon) = \mathcal{F}\{f(x)\} = \int_{-\infty}^{\infty} f(x)\mathrm{e}^{-j2\pi x\varepsilon}\, dx, \tag{B.1}$$

and its inverse

$$f(x) = \mathcal{F}^{-1}\{F(\varepsilon)\} = \frac{1}{2\pi}\int_{-\infty}^{\infty} F(\varepsilon)\mathrm{e}^{j2\pi x\varepsilon}\, d\varepsilon. \tag{B.2}$$

Capitalized letters here denote a Fourier transformed variable. The discrete Fourier transform (DFT) is given by

$$X_k = \sum_{n=0}^{N-1} x_n\, \mathrm{e}^{-j\frac{2\pi}{N}kn}, \quad k = 0, 1, \ldots N-1, \tag{B.3}$$

where $\mathrm{e}^{-j\frac{2\pi}{N}}$ is the N-th root of unity. Also, we have the inverse DFT

$$x_n = \frac{1}{N}\sum_{k=0}^{N-1} X_k\, \mathrm{e}^{j\frac{2\pi}{N}kn}, \quad n = 0, 1, \ldots N-1. \tag{B.4}$$

B.2 Discrete velocity field

From Eq. (4.8), we may derive the expressions used in the angular spectrum algorithm, Eqs. (4.9) and (4.10). First, we need to obtain the discrete version of Eq. (4.8), which calculates the velocity field in the point (x, z). We consider the two-dimensional case

$$v(x,z) = \frac{k}{2\pi} \int_{-\infty}^{\infty} V(n_x)\, \mathrm{e}^{jk(xn_x + \Delta z n_z)} dn_x.$$

Now, $n_x = \lambda m_x \Delta f$, so $dn_x = \lambda \Delta f dm_x$, and since $n_z = [1 - (\lambda m_x \Delta f)^2]^{1/2}$

$$v(x,z) = \Delta f \frac{\lambda k}{2\pi} \int_{-\infty}^{\infty} v(\lambda m_x \Delta f)\, \mathrm{e}^{jk[x\lambda m_x \Delta f + \Delta z \sqrt{1-(\lambda m_x \Delta f)^2}\,]} dm_x$$

$$v(x,z) = \Delta f \int_{-\infty}^{\infty} v(\lambda m_x \Delta f)\, \mathrm{e}^{j2\pi[x m_x \Delta f + \Delta z \sqrt{1/\lambda^2 - (m_x \Delta f)^2}\,]} dm_x$$

We obtain the discrete form by letting the integral go to a Riemann sum over m_x, which ranges from $-N/2+1$ to $N/2$. The discrete spatial indices are i_x so that $x = i_x \Delta d$, which gives

$$v_D(i_x \Delta d, z) = \Delta f \sum_{m_x=-N/2+1}^{N/2} V_D(m_x \Delta f)\, \mathrm{e}^{j2\pi[\frac{i_x m_x}{N} + \Delta z \sqrt{1/\lambda^2 - (m_x \Delta f)^2}\,]}, \quad \text{(B.5)}$$

for $i_x = -N/2+1, \ldots, N/2$. Here, we have applied the fact that $\Delta d \Delta f = 1/N$. V_D is simply the discrete Fourier transform of $v(i_x \Delta d, 0)$

$$V_D(m_x \Delta f) = \Delta d \sum_{i_x=-N/2+1}^{N/2} v(i_x \Delta d, 0)\, \mathrm{e}^{-j\frac{2\pi}{N} m_x i_x}. \quad \text{(B.6)}$$

Shifted angular spectrum

In this section the derivation of Eqs. (4.9) and (4.10) is given. As mentioned in Section 4.3, we need to shift the spatial and spatial frequency indices, so they range from 0 to $N-1$. This is because of the definition of the DFT.

We begin with Eq. (B.6) and introduce the shifted variable $i'_x = i_x + \frac{N}{2} - 1$

$$V_D(m_x \Delta f) = \Delta d \sum_{i'_x=0}^{N-1} v((i'_x - \tfrac{N}{2}+1)\Delta d, 0)\ \mathrm{e}^{-j\frac{2\pi}{N} m_x (i'_x - \frac{N}{2}+1)},$$

for $m_x = -\frac{N}{2}+1, \ldots, \frac{N}{2}$. Similarly we shift m_x to $m'_x = m_x + \frac{N}{2} - 1$ and obtain

$$V_D((m'_x - \tfrac{N}{2}+1)\Delta f) = \Delta d \sum_{i'_x=0}^{N-1} v((ix' - \tfrac{N}{2}+1)\Delta d, 0)\ \mathrm{e}^{-j\frac{2\pi}{N}(m'_x - \frac{N}{2}+1)(i'_x - \frac{N}{2}+1)},$$

where $m'_x = 0 \ldots N-1$. Now, since $(m'_x - \frac{N}{2}+1)(i'_x - \frac{N}{2}+1) = m'_x i'_x + i'_x(-\frac{N}{2}+1) + (m'_x - \frac{N}{2}+1)(-\frac{N}{2}+1)$

$$\begin{aligned} V_D((m'_x - \tfrac{N}{2}+1)\Delta f) &= \Delta d\, \mathrm{e}^{-j\frac{2\pi}{N}(m'_x - \frac{N}{2}+1)(-\frac{N}{2}+1)} \\ &\quad \times \sum_{i'_x=0}^{N-1} v((i'_x - \tfrac{N}{2}+1)\Delta d, 0)\ \mathrm{e}^{-j\frac{2\pi}{N}(i'_x(-\frac{N}{2}+1))} \mathrm{e}^{-j\frac{2\pi}{N} m'_x i'_x}, \\ &= \Delta d\, \mathrm{e}^{-j\frac{2\pi}{N}(m'_x - \frac{N}{2}+1)(-\frac{N}{2}+1)} \\ &\quad \times \mathrm{DFT}\left\{ v((i'_x - \tfrac{N}{2}+1)\Delta d, 0)\ \mathrm{e}^{-j\frac{2\pi}{N}(i'_x(-\frac{N}{2}+1))} \right\}. \end{aligned} \tag{B.7}$$

This is precisely Eq. (4.9), multiplied with $\mathrm{e}^{-j\frac{2\pi}{N}(m'_x - \frac{N}{2}+1)(-\frac{N}{2}+1)}$. This term will be abbreviatet later when inserted into v_D.

Formula for updated velocity field

Using the shifted variables m'_x and i'_x, we obtain from Eq. (B.5)

$$\begin{aligned} v_D((i'_x - \tfrac{N}{2}+1)\Delta d, z) &= \Delta f \sum_{m'_x=0}^{N-1} V_D((m'_x - \tfrac{N}{2}+1)\Delta f) \\ &\quad \times \mathrm{e}^{j\frac{2\pi}{N}(i'_x - \frac{N}{2}+1)(m'_x - \frac{N}{2}+1)} \\ &\quad \times \mathrm{e}^{j2\pi\Delta z\sqrt{1/\lambda^2 - ((m'_x - \frac{N}{2}+1)\Delta f)^2}} \\ &= \Delta f \sum_{m'_x=0}^{N-1} V_D((m'_x - \tfrac{N}{2}+1)\Delta f) \\ &\quad \times \mathrm{e}^{j\frac{2\pi}{N}(i'_x - \frac{N}{2}+1)(m'_x - \frac{N}{2}+1)} \mathrm{e}^{j\Delta z k_z}, \end{aligned}$$

where $k_z = 2\pi[1/\lambda^2 - ((m'_x - \frac{N}{2}+1)\Delta f)^2]^{1/2}$. Now, since $(i'_x - \frac{N}{2}+1)(m'_x - \frac{N}{2}+1)$ may be written as $m'_x i'_x + m'_x(-\frac{N}{2}+1) + (i'_x - \frac{N}{2}+1)(-\frac{N}{2}+1)$

$$\begin{aligned} v_D((i'_x - \tfrac{N}{2}+1)\Delta d, z) = {} & \Delta f \; \mathrm{e}^{j\frac{2\pi}{N}(i'_x - \frac{N}{2}+1)(-\frac{N}{2}+1)} \\ & \times \sum_{m'_x=0}^{N-1} V_D((m'_x - \tfrac{N}{2}+1)\Delta f) \; \mathrm{e}^{j\frac{2\pi}{N}(m'_x(-\frac{N}{2}+1))} \\ & \times \mathrm{e}^{j\Delta z k_z} \mathrm{e}^{j\frac{2\pi}{N} i'_x m'_x} \end{aligned} \tag{B.8}$$

To complete the derivation, we insert the expression for V_D, Eq. (B.7), and obtain

$$\begin{aligned} v_D((i'_x - \tfrac{N}{2}+1)\Delta d, z) = {} & \Delta f \Delta d \; \mathrm{e}^{j\frac{2\pi}{N}(i'_x - \frac{N}{2}+1)(-\frac{N}{2}+1)} \mathrm{e}^{j\frac{2\pi}{N}(m'_x - \frac{N}{2}+1)(-\frac{N}{2}+1)} \\ & \times \sum_{m'_x=0}^{N-1} \mathrm{DFT}\left\{ v((i'_x - \tfrac{N}{2}+1)\Delta d, 0) \; \mathrm{e}^{-j\frac{2\pi}{N}(i'_x(-\frac{N}{2}+1))} \right\} \\ & \times \mathrm{e}^{j\frac{2\pi}{N}(m'_x(-\frac{N}{2}+1))} \mathrm{e}^{j\Delta z k_z} \mathrm{e}^{j\frac{2\pi}{N} i'_x m'_x} \\ \\ = {} & \Delta f \Delta d \; \mathrm{e}^{j\frac{2\pi}{N}(i'_x(-\frac{N}{2}+1))} \\ & \times \sum_{m'_x=0}^{N-1} \mathrm{DFT}\left\{ v((i'_x - \tfrac{N}{2}+1)\Delta d, 0) \; \mathrm{e}^{-j\frac{2\pi}{N}(i'_x(-\frac{N}{2}+1))} \right\} \\ & \times \mathrm{e}^{j\Delta z k_z} \mathrm{e}^{j\frac{2\pi}{N} i'_x m'_x} \\ \\ = {} & \Delta f \; \mathrm{e}^{j\frac{2\pi}{N}(i'_x(-\frac{N}{2}+1))} \\ & \times \Delta d \sum_{m'_x=0}^{N-1} \mathrm{DFT}\left\{ v((i'_x - \tfrac{N}{2}+1)\Delta d, 0) \; \mathrm{e}^{-j\frac{2\pi}{N}(i'_x(-\frac{N}{2}+1))} \right\} \\ & \times \mathrm{e}^{j\Delta z k_z} \mathrm{e}^{j\frac{2\pi}{N} i'_x m'_x} \\ \\ = {} & \Delta f N \; \mathrm{IDFT}\Big[\Delta d \, \mathrm{DFT}\Big\{ \\ & v((i'_x - \tfrac{N}{2}+1)\Delta d, 0) \; \mathrm{e}^{-j\frac{2\pi}{N}(i'_x(-\frac{N}{2}+1))} \Big\} \mathrm{e}^{j\Delta z k_z} \Big] \end{aligned}$$

which is Eq. (4.10).

Appendix C

The Matlab code

The simulator that produces the results in this thesis has been written in Matlab version 7.5.0. Parts of the code is included in the following.

C.1 Initializing

```
function P = ASAParam3D(f0, c, maxHarm, varargin)
% Create struct containing parameters for ASAlinear or ASAnonlinear,
% to calculate linear or nonlinear field propagation.
%
% Usage P = ASAParam3D(f0, c, maxHarm, A, B, u, N, Zmax, Zincr, FsFact)
%
% All arguments can be omitted, or replaced by []
% Optional input arguments:
%
%  f0       : Frequency of fundamental.
%  c        : Sound speed.
%  maxHarm  : Number of harmonics in calculation.
%  A, B     : Size of source in x and y-direction.
%  u        : Velocity distribution at source. Integer or Lx*Ly matrix.
%  N        : Number of samples along source plane.
%  Zmax     : Maximum lateral distance, in units of lambda.
%  Zincr    : Distance between adjacent planes, given in units of lambda.
%  FsFact   : Factor for determining sampling frequency.
%             Fs = FsFact/lambda.
%

P.date = date;

%% Parameters concerning the system and medium

if nargin<1 | isempty(f0), P.freq = 3e6; else P.freq = f0; end
if nargin<2 | isempty(c), P.c = 1500; else P.c = c; end
```

```
P.lambda = P.c/P.freq;
P.lambdaSQ = (P.c-1e-4)/P.freq; % Speed of propagation subtracted a tiny
                                % number to avoid pole in Eq. (8).
P.rho = 10^3;                   % Density in medium in kg/m^3

%%    Parameters controlling the ASA.
if nargin<3 | isempty(maxHarm),
    P.maxHarm = 10;
else
    P.maxHarm = maxHarm;
end

if nargin<4 | isempty(varargin{1}) , % Either not given or given as '[]'
    P.A = 16*P.lambda;              % Extent of source in x-direction
else
    P.A = varargin{1};
end

              etc...........


P.Fs = P.FsFact/P.lambda;   % Spatial sampling frequency.
P.deltaD = 1/P.Fs;          % Sampling interval in the spatial domain
P.D = P.deltaD*P.N;         % Size of source plane
P.deltaF = 1/P.D;           % Samp. interval in spatial frequency domain

%% Parameters concerning the source
P.Lx = round((2*P.A)/P.deltaD);  % # of samples along source
P.Ly = round((2*P.B)/P.deltaD);
P.v = zeros(P.N, P.N);           % Normal velocity at source plane (z=0)

% Source is to be located in the middle of the source plane.
elemx = round(P.N/2 - P.Lx/2);   % First matrix element that contains
                                 % source, in the x-direction.
elemy = round(P.N/2 - P.Ly/2);   % likewise in the y-direction
% Insert initial velocity distribution:
P.v(elemx:elemx + P.Lx-1, elemy:elemy + P.Ly-1) = u;


if (mod(P.Lx, 2) == 0)
    P.phiX = 1/2;           % Lx is even, correct phase shift error
else
    P.phiX = 0;
end

if (mod(P.Ly, 2) == 0)
    P.phiY = 1/2;
else
```

```
    P.phiY = 0;
end

%% Parameters controlling what to calculate
P.noOfSteps = fix(P.Zmax/P.Zincr);
P.z = (1:P.noOfSteps) * P.Zincr;

% Ix, Iy, Mx and My are identical matrices, and so
% Ix is used because of memory issues.
P.Ix = linspace(-P.N/2.0+1, P.N/2.0, P.N);  % Lateral samples
P.IxPrime = 0:P.N-1;                        % Shifted version

P.textinfo = '';
```

C.2 Linear wave propagation

```
function ASAlinear3D(P, saveFigs, saveField)
% Calculate linear propagation of acoustical 3-D field.
% Usage: ASAlinear3D([P], [saveField])
% P is a struct containing parameters for the angular spectrum approach.
% To define it use P = ASAParam(args), otherwise default values are used.
% saveFields = 1 saves three harmonics for later plotting.

changeColorMap;

if nargin<1 | isempty(P)
    % Struct P is not given. Call ASAParam with default values:
    % P = ASAParam(f0, c, maxHarms, N, Zmax, Zincr, FsFact)
    disp(strcat(10,10,'NOTE: Struct P not given! ', 10,...
                'DEFAULT VALUES WILL BE USED.', 10,...
                'For help on defining your own parameters, type',...
                10, '"help ASAParam"'))
    P = ASAParam(3e6, 1500, 10, 256, 400, 2, 2);
end

if nargin<2 || isempty(saveFigs), saveFigs = 0; end
if nargin <3, saveField = 0; end

P.maxHarm = 1;  % linear field

%% Directories
mydir = pwd;
fieldsdir = '/ifi/midgard/p17/highres/krispe/FELT';
newdir = sprintf('F%0.5g_c%d_N%d_Fs%d_Harm%d', ...
                              P.freq, P.c, P.N, P.FsFact, P.maxHarm);
fieldsdir = strcat(fieldsdir,'/',newdir)
% Where to put the figures:
figdir = ...;
```

```
if saveField
    [s,mess,messid] = mkdir(fieldsdir);
    name = strcat(fieldsdir,'/P.mat');
    save(name, 'P')
end


%% Window
N = P.N;
Padding = floor(N/5);
Win1D = [zeros(1,floor(Padding/2)), tukeywin(N-Padding,.2).', ...
         zeros(1,ceil(Padding/2))];
Win = Win1D.' * Win1D;
clear Win1D


% These are used often and defined here for easy reading..
expInDft = exp( -j*2*pi/N * (-N/2+1)*P.IxPrime ).'*...
           exp( -j*2*pi/N * (-N/2+1)*P.IxPrime );

expTerm = exp(j*2*pi/N * (-N/2+1)*P.IxPrime ).' * ...
          exp(j*2*pi/N * (-N/2+1)*P.IxPrime );


%% Calculating transfer function
H = exp(j*P.Zincr * 2 * pi * sqrt(1.0/P.lambdaSQ^2 - ...
                  (repmat(P.Ix.', 1, P.N)*P.deltaF).^2 - ...
                  (repmat(P.Ix, P.N, 1)*P.deltaF).^2)).* Win;


%% Initial angular spectrum (first step) -------------------------------

sizeIx = numel(P.Ix);

% Save these values for plotting:
xzPlaneLin = zeros(sizeIx, P.noOfSteps);
onaxis = zeros(numel(P.z),1);
offaxis = zeros(numel(P.z),1);


phaseshift =   exp( (-j*2*pi/N)*(P.Ix*P.phiX) ).'  * ...
               exp( (-j*2*pi/N)*(P.Ix*P.phiY) );

V = sinc(P.Ix/N).' * sinc(P.Ix/N) .* ...
        (phaseshift .* (P.deltaD^2 * fft2( P.v .*  expInDft)));
clear phaseshift P.v

v = zeros(sizeIx, sizeIx);  % To contain linear field at each step
```

```
v(:,:)= P.deltaF^2 * P.N^2 * expTerm .* ifft2(V.* H);

if saveField
    v1 = v;
    fname = '/v1_z1.mat';
    name = strcat(fieldsdir, fname);
    save(name, 'v1')
end

xzPlaneLin(:,1) = v(:, P.N/2);
onaxis(1) = v(P.N/2, P.N/2);
offaxis(1) = v(P.N/2 + P.Lx, P.N/2);

%% Loop over z-values to calculate field ------------------------
for step = 2:P.noOfSteps

    disp(strcat(num2str(P.noOfSteps-step),' steps to go...'))

    % Angular spectrum in the current source plane
    V = P.deltaD^2 * fft2(squeeze(v(:,:)).* Win .* expInDft);

    % Calc new v at Zincr:
    v(:,:) = P.deltaF^2 * P.N^2 * (expTerm .* ifft2(V.* H));

    onaxis(step) = v(P.N/2, P.N/2);
    offaxis(step) = v(P.N/2 + P.Lx, P.N/2);
    xzPlaneLin(:,step) = v(:, P.N/2);

    if saveField
        v1 = v;
        fname = sprintf('/v1_z%d.mat', step);
        name = strcat(fieldsdir, fname);
        save(name, 'v1')
    end

end

name = strcat(fieldsdir,'/xzPlaneLin.mat');
save(name, 'xzPlaneLin')
......
```

C.3 Nonlinear wave propagation

```
function ASAnonlinear3D(P, saveFigs, saveFields)
% Calculate nonlinear propagation of acoustical 3-D field.
% Usage: ASAnonlinear3D([P], [saveFigs], [saveFields])
% P is a struct containing parameters for the angular spectrum approach.
% To define it use P = ASAParam(args), otherwise default values are used.


changeColorMap;

if nargin<1 | isempty(P)
   % ..... As before
end

if nargin<2 || isempty(saveFigs), saveFigs = 0; end
if nargin <3, saveFields = 0; end

beta = 3.5; % nonlin param, = 1+B/2A
alpha0 = 25e-15;
b = 2;
q = 0.35;
harms2save = 3;

N = P.N;
maxHarm = P.maxHarm;


%% Directories
mydir = pwd;
etc .....

%% Window
Padding = floor(N/5);
Win1D = [zeros(1,floor(Padding/2)), tukeywin(N-Padding,.2).', ...
         zeros(1,ceil(Padding/2))];
Win = Win1D.' * Win1D;
clear Win1D

%(...)

%% Calculating transfer functions ---------------------------------------
sizeIx = numel(P.Ix);
H = zeros(maxHarm, sizeIx, sizeIx);   % Matrix containing transferfuncs
for harm = 1:maxHarm
    % H(n, :, :) is transferfunc for n-th harmonic:
    H(harm,:,:) =  exp(j*(P.Zincr/2) * ...
                   2*pi*sqrt(1.0/(P.lambdaSQ/harm)^2 - ...
                   (repmat(P.Ix.', 1, P.N)*P.deltaF).^2 - ...
```

```
                    (repmat(P.Ix, P.N, 1)*P.deltaF).^2)).* Win;
end

% Save these values for plotting:
xzPlane = zeros(sizeIx, P.noOfSteps);
%etc...

disp('Calculating pressure field...')

%v(n,:) is v_n, velocity field for the n-th harm.
v = zeros(maxHarm, sizeIx, sizeIx);
v_ = zeros(maxHarm, sizeIx, sizeIx); % Temporary mid-step fields

%% First step ------------------------------------------------------------

V = sinc(P.Ix/N).' * sinc(P.Ix/N) .* ...
                    (phaseshift .* (P.deltaD^2 * fft2( P.v .*  expInDft)));

v_(1,:,:)= P.deltaF^2 * P.N^2 * expTerm .* ifft2(V.* squeeze(H(1,:,:)));

v_ = nonlinstep3D(v_, P.Zincr, beta, alpha0, b,q,N, maxHarm,P.freq,P.c);

for harm = 1:maxHarm
    V = P.deltaD^2 * fft2( squeeze(v_(harm,:,:)).* Win .* expInDft);
    onaxisAll(harm,1) = V(P.N/2, P.N/2);
    v(harm,:,:) = P.deltaF^2 * P.N^2 * ...
                               expTerm .* ifft2(V.* squeeze(H(harm,:,:)));
end

if saveFields
    for harm = 1:harms2save
        varname = strcat('v',num2str(harm));
        evalc(sprintf('v%d = v(%d,:, :)', harm, harm));
        fname = sprintf('/v%d_z1.mat', harm);
        name = strcat(fieldsdir, fname);

        save(name, varname)
    end
end

xzPlane(:,1) = v(1, :, P.N/2); % Fundamental
%etc

%% Loop over z-values to calculate field --------------------------

for step = 2:P.noOfSteps
    disp(strcat(num2str(P.noOfSteps-step),' steps to go...'))

    % Diffraction substep Zincr/2
```

```
    for harm = 1:maxHarm
        % Angular spectrum in the current source plane
        V = P.deltaD^2 * fft2(squeeze(v(harm,:,:)).* Win .* expInDft);

        % Calc new v at Zincr/2:
        v_(harm,:,:) = P.deltaF^2 * P.N^2 * ...
                        (expTerm .* ifft2(V.* squeeze(H(harm,:,:))));
    end

    v_ = nonlinstep3D(v_,P.Zincr,beta,alpha0,b,q,N,maxHarm,P.freq, P.c);

    for harm = 1:maxHarm
        V = P.deltaD^2 * fft2( squeeze(v_(harm,:,:)).* Win .* expInDft);
        onaxisAll(harm,step) = V(P.N/2, P.N/2);
        % Final field at Zincr:
        v(harm,:,:) = P.deltaF^2 * P.N^2 * ...
                       (expTerm .* ifft2(V.*  squeeze(H(harm,:,:))));
    end

    if saveFields
        .....
    end
    %  Save for plotting
    xzPlane(:,step) = v(1, :, P.N/2);
    % etc.....
end % of main loop

clear v v_ H

name = strcat(fieldsdir,'/xzPlane.mat');  save(name, 'xzPlane')
% etc
```

C.4 The nonlinear substep

```
function u = nonlinstep3D(v, Zincr, beta, ...
                          alpha0, b, q, N, maxHarm, f0, c)
% Nonlinear step of the ASA propagation.
% Adds nonlinear effects to the calculated field after diffraction.
% Is called during every step Zincr, and is based on the FDSBE.
% Also includes attenuation.
%
% v         - field calculated at Zincr/2.
%             v(n,:, :) is the n-th harmonic.
% Zincr     - length of the nonlinear substep
% beta      - nonlinear coefficient
% b         - frequency dependency in attenuation
```

```
% q         - for upramping of attenuation
% N         - number of spatial samples
% maxHarm   - maximum number of harmonics
% f0        - fundamental frequency
% c         - sound speed


u = zeros(maxHarm, N,N); % To contain the new fields

for n = 1:maxHarm
    bn = b + ((n-1)/maxHarm)*q;

    accr = zeros(1,N, N); % Accretion of n-th harmonic
    depl = zeros(1,N, N); % Depletion of n-th harm to other harms.

    for k = 1:n-1
        accr = accr + ( k*v(k,:, :) .* v(n-k,:, :) );
    end
    for k = n+1:maxHarm
        depl = depl + ( n*v(k,:, :) .* conj(v(k-n,:, :)) );
    end


    u(n,:, :) = v(n,:, :) + ...
        ( (j*beta*pi*f0/(c^2) * (accr+depl)) - ...
           alpha0 * (n*f0)^bn * v(n,:, :) ) * Zincr;

end
```

C.5 Other files

figReadable.m

```
function figReadable(saveFigs)
% For nicer output of Matlab figures

set(findall(gcf,'Type','text'),'FontSize',14);
set(findall(gcf,'Type','axes'),'FontSize',14);
set(findall(gcf,'Type','axes'),'LineWidth',2);
set(findall(gcf,'Type','line'),'LineWidth',2);
set(get(gca,'Title'),'FontSize',18,'FontWeight','demi');
if saveFigs, title(''); end
```

circularSource.m

```
function v = circularSource(deltaD, radius, N, L, weighting)
% Create circular source for the ASA
% N - Number of lateral points of source plane
```

```
% L - Number of lateral points of source
% Weighting - Initial peak velocity

Mvec = linspace(-N/2.0+1, N/2.0, N);
u = (sqrt( (repmat(Mvec', 1, N)*deltaD).^2 + ...
           (repmat(Mvec, N, 1) *deltaD).^2 ) <= radius) * weighting;

elemx = round(N/2 - L/2);
v = u(elemx:elemx + L-1, elemx:elemx + L-1);
```

changeColormap.m

```
% Define new colormap that prints
% correctly in gray-scale
CMRmap = [0.00 0.00 0.00;
          0.15 0.15 0.50;
          0.30 0.15 0.75;
          0.60 0.20 0.50;
          1.00 0.25 0.15;
          0.90 0.50 0.00;
          0.90 0.75 0.10;
          0.90 0.90 0.50;
          1.00 1.00 1.00];

x = 1:8/63:9; % 64 color levels
xl = 1:9;
for i=1:3
    sCMRmap(:,i) = spline(xl,CMRmap(:,i),x)';
end
sCMRmap = abs(sCMRmap/max(sCMRmap(:)));
colormap(sCMRmap);
```

C.6 Calls to the simulator

```
function exampleRuns(Ex)
% Calls to the simulator for examples in the thesis.

cp = strcmp(Ex, 'cp');
%etc...

% Wu 3-D plots
if wu
    f0 = 3e6;  c = 1500;   lambda = c/f0;
    A = 16*lambda;   B = 12*lambda;

    P = ASAParam3D(f0, c, 1, A, B, 1.0, 512, 400, 2, 2);
    P.textinfo = 'Wu 3D-example';
    ASAlinear3D(P,1)
```

```
end

% Parker linear example: circular unfocused piston operating in water
if cp
    ...
end

% Zemp linear example
if zemp
    ...
end

% Parker nonlinear example: circular unfocused piston operating in water
if cpNL
    f0 = 2.25e6; c = 1500;
    maxHarm = 30;

    A = 0.019; B=A;
    N = 512;
    Zmax = 1125;
    Zincr = 10;
    FsFact = 4;
    lambda = c/f0;
    deltaD = lambda/FsFact;
    weighting = 0.0667;         % Initial velocity

    L = round((2*A)/deltaD);
    u = circularSource(deltaD, A, N, L, weighting);

    P = ASAParam3D(f0, c, maxHarm, A, B, u, N, Zmax, Zincr, FsFact);
    P.textinfo = 'Parker nonlinear example';
    ASAlinear3D(P,1,1)
    ASAnonlinear3D(P,1)
    plotCP(0)
end


if tichy
    f0 = 2e5;   c = 1500;   lambda = c/f0;  % 0.0075 m
    A = 0.0345; B=A;

    FsFact = 4;
    deltaD = lambda/FsFact;

    % Initial velocity:
    weighting = 0.5893;       %        1000 W

    Zincr = 5;
    maxHarm = 30;
```

```
    N = 512;

    L = round((2*A)/deltaD);
    u = circularSource(deltaD, A, N, L, weighting);
    Win = window(@hamming,L);
    u = u .* (Win*Win.'); % Apply weighting to transducer
    Zmax = 2000;   % 15 m

    P = ASAParam3D(f0, c, maxHarm, A, B, u, N, Zmax, Zincr, FsFact);
    P.rho = 1027;            % This simulation is in freshwater
    P.textinfo = 'Tichy';
    P.weighting = weighting;
    ASAlinear3D(P,1,1)
    ASAnonlinear3D(P,1)
    plotTichy(weighting, 1)

end
```

Appendix D

Additional figures

This chapter contains some additional figures included for illustratory purposes. It may be skipped without loss of comprehension of the text. A detailed discription of the figures will not be given, but the various figures are commented in their respective captions.

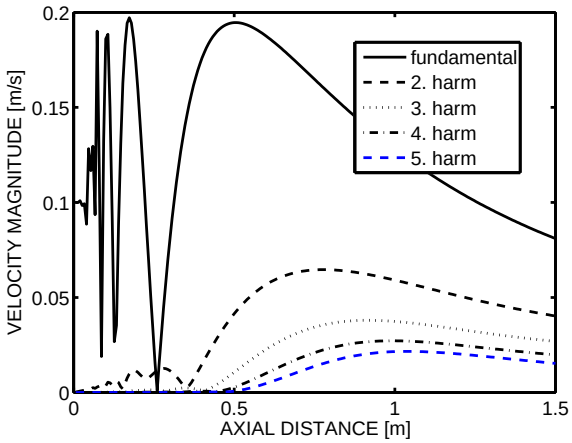

Fig. D.1: Axial field of the 2.25 MHz circular transducer, computed with the FDSBE given by Christopher and Parker. This version of the FDSBE resulted in too little energy being transferred to the higher harmonics.

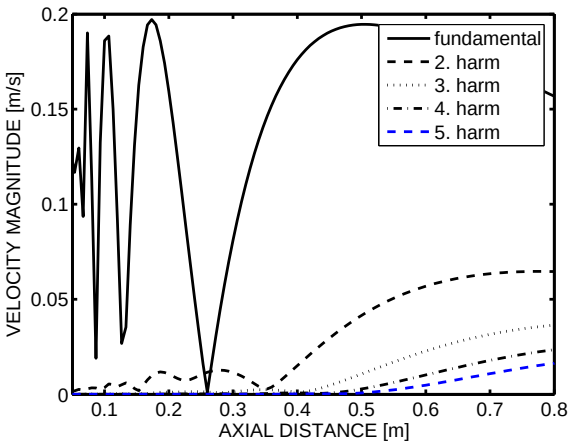

(a) The zooming in of Fig. D.1, to give the same view as in (b). This is equal to the results given by Fjellestad (2000) and Synnevåg (1998).

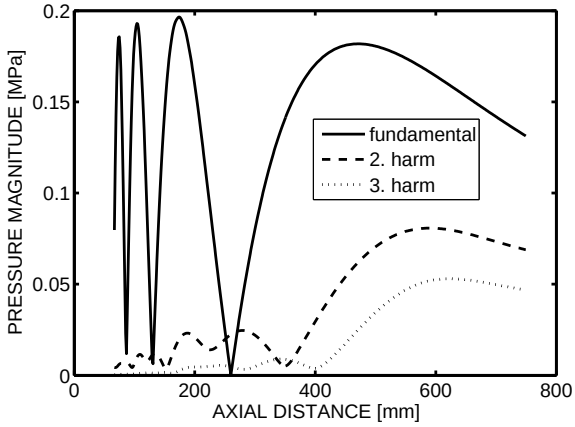

(b) Fig. 6.12(b) repeated for comparison, computed with the FDSBE as given by Eq. (5.9). Note that the level of the higher harmonics is higher compared to (b). This is consistent with the measurements of Baker *et al.*

Fig. D.2: Axial field of the 2.25 MHz circular transducer.

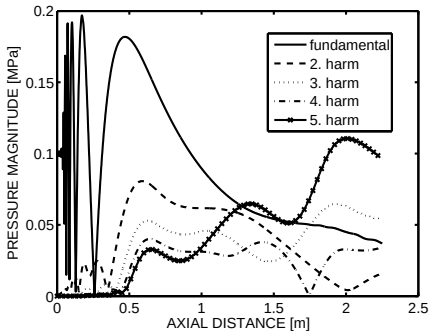

(a) $\Delta z = \lambda$

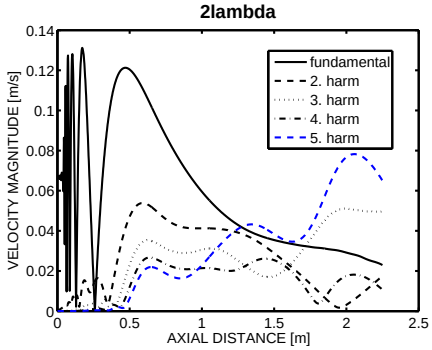

(b) $\Delta z = 2\lambda$

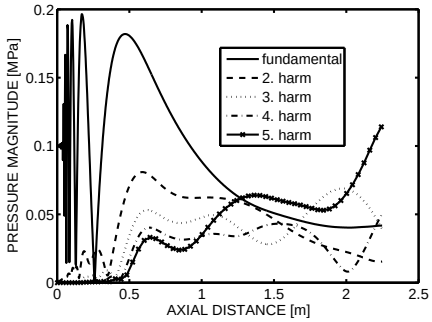

(c) $\Delta z = 4\lambda$

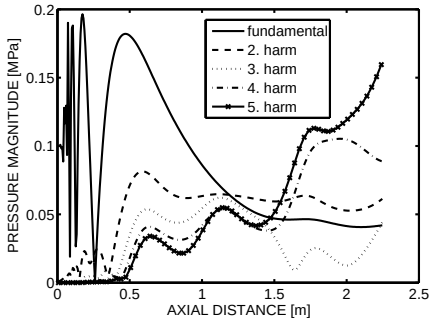

(d) $\Delta z = 10\lambda$

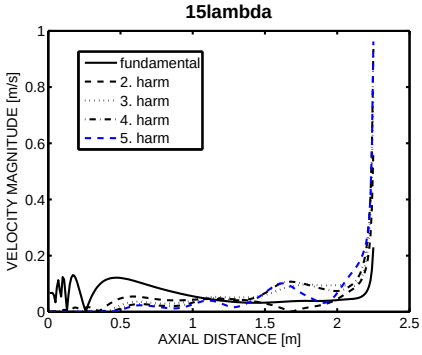

(e) $\Delta z = 15\lambda$

Fig. D.3: Axial field of the transducer used by Baker *et al.*, simulated with the incorrect value $b = 1.1$, for different stepsizes. The higher harmonics tend to infinity for large step-sizes.

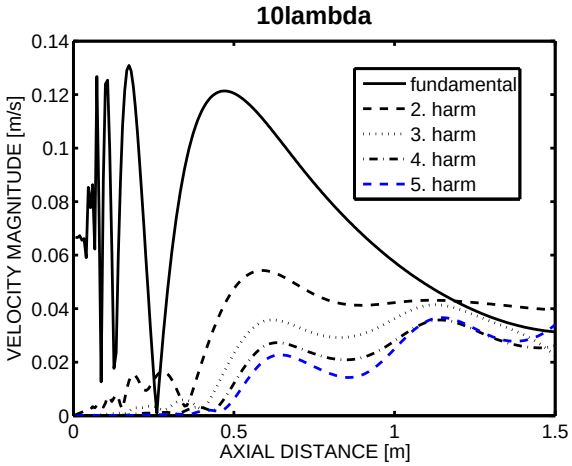

(a) q=1

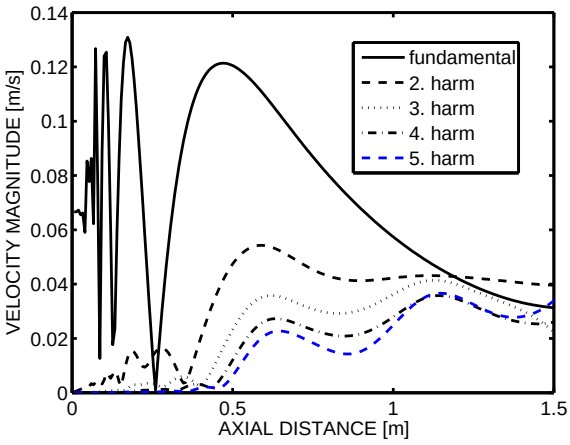

(b) q=2

Fig. D.4: Axial field of the transducer used by Baker *et al.*, simulated with the incorrect value $b = 1.1$, 30 harmonics included, $\Delta z = 10$. $F_s = 1$, $N = 512$. The value of q seemed to make no difference.

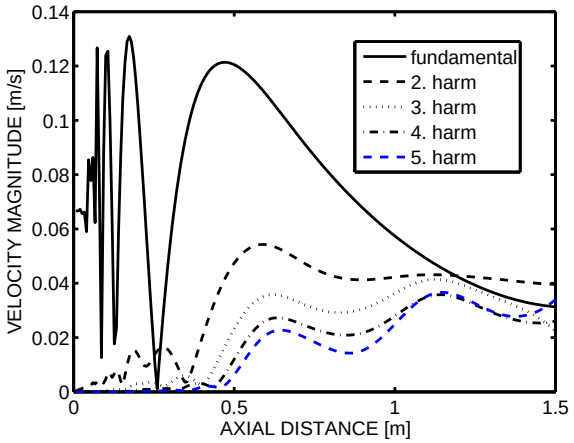

(a) Axial field

Fig. D.5: Axial field of the transducer used by Baker *et al.*, simulated with the incorrect value $b = 1.1$. Ten harmonics included, q=0.5, $\Delta z = 10$. $F_s = 1$, $N = 1024$. Apparently spatial aliasing was not the cause of the error.

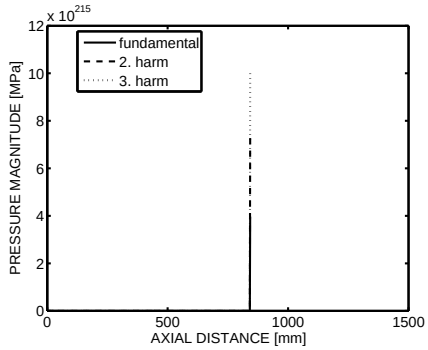

Fig. D.6: Axial field of the 2.25 MHz transducer calculated with 50 harmonics. Field tends to infinity due to the incorrect value $b = 1.1$. No upramping of the attenuation used here, $\Delta z = 2$, with $F_s = 1$, $N = 512$.

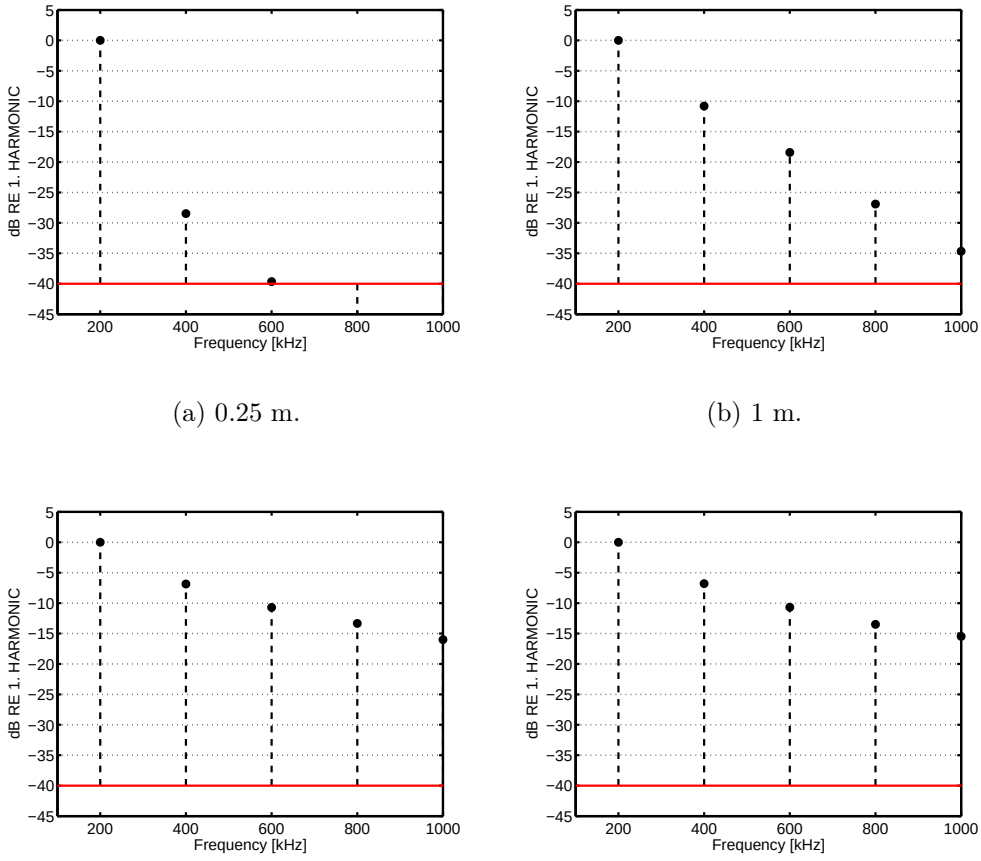

(a) 0.25 m.

(b) 1 m.

(c) 7 m.

(d) 12 m.

Fig. D.7: Averaged FFT of field at different ranges, for the power setting 1000 W. Value in point of interest averaged with points approximately 6 cm away.